FABRICATION AND CHARACTERIZATION OF MAGNETORESPONSIVE CARBON NANOTUBE-INFUSED POLYSULFONE (CNT-IPSF) NANOCOMPOSITES FOR WATER PURIFICATION

BY

Shisia Kuboka Silvanus (MSc Chemistry, KU)

Registration Number: I84/11265/06

A Thesis Submitted in Fulfillment of the Requirements for the Award of the Degree of Doctor of Philosophy (Chemistry) in the School of Pure and Applied Sciences of Kenyatta University

September, 2017

DECLARATION

This thesis is my original work and has not been presented elsewhere for the award of a Degree or any other award.

Shisia Kuboka Silvanus

Signature…… Date 21/9/2017

We confirm that the work reported in this thesis has been submitted with our approval as University Supervisors

Prof. Hudson Nyambaka

Department of Chemistry, Kenyatta University

Signature……Date 21/09/17

Dr. Naumih Noah

School of Pharmacy and Health Sciences,

United States International University-Africa

Signature……Date 21.09.2017

Dr. Dickson Andala

Department of Chemistry, MultiMedia University of Kenya

Signature……Date 21/09/2017

DEDICATION

This thesis is dedicated to my lovely wife Margaret Mboga Kagali and children Osteen Shisia and Audrey Angela and my dear parents Charles Shisia Olando and Ruth Anjelina Omukubi.

ACKNOWLEDGEMENTS

I wish to thank the University for providing a conducive learning environment during my entire study period. I would want to acknowledge the following people for their support towards the successful completion of my research work. My special thanks go to my supervisors: Prof. Hudson Nyambaka, Kenyatta University, Dr. Naumih Noah, United States International University-Africa; and Dr. Dickson Andala, Multimedia University of Kenya, for their scholarly guidance and encouragement during the whole period of my study at Kenyatta University. In addition, their facilitation for analysis of my samples using special equipment not available locally is highly appreciated. They were also steadfast in reading my thesis drafts, progress reports and in providing fast responses of their comments. Special thanks also go to NACOSTI, Kenya for funding this research work.

In addition, the teaching staff in the Department of Chemistry was also of great help in ensuring that postgraduate students were accorded the necessary support. Special thanks go to the technical staff from Department of Chemistry for their technical advice in some experiments. They include Ms Catherine Wanja, Ms Rachel Mwale, Ms Jane Mburu, Mr. Antony Njagi, Mr. Stanley Kariuki and Mr. John Kamau. The technologists from the Department of Physics headed by Mr. Fred Mudimba and Mr. Abraham Chesaina are highly appreciated for their technical expertise on Lindberg Blue furnace in the department necessary for synthesis of carbon nanotubes.

Finally and most important, I would like to most sincerely thank my God for giving me strength, wisdom, humility and understanding that enabled me finish this course. Praise be unto His Name, Amen.

TABLE OF CONTENTS

LIST OF TABLES

LIST OF FIGURES

LIST OF PUBLICATIONS

Shisia K. Silvanus, Naumih N., Nyambaka H and Andala M. Dickson (2017). Fabrication and Characterization of Magnetoresponsive Carbon Nanotube Infused Polysulfone Nanocomposites for water purification. Sustainable Use of Water Resources; Expert Workshop proceedings, ISBN 978-3-7369-9453-9, PP 71-80.

Shisia K. Silvanus, Naumih N., Nyambaka H and Andala D.M (2016). Efficiency of Fabricated CNT-IPSF/Fe_3O_4 Nanocomposites in Removal of Phenanthrenes from Contaminated Water. International Journal of scientific and Technology Research IJSTR ISSN 2277-8616 Volume 5, Issue 9, September 2016, PP 83-92

Shisia K. Silvanus and Andala M. Dickson (2016). Sorption of Lead(II) ions from Aqueous Solution by Fabricated Magneto responsive CNT-IPSF/Fe_3O_4 Nanocomposites. IOSR Journal of Applied Chemistry ISSN 2278-5736.Volume 9, Issue 9 Ver. I (Sept. 2016), PP 17-27

Shisia K. Silvanus and Andala M. Dickson (2016). Fabrication and Characterization of Magnetoresponsive Carbon Nanotube Infused Polysulfone Nanocomposites. International Journal of Innovative Research and Advanced Studies (IJIRAS): ISSN: 2394-4404. Volume 3 Issue 9, August 2016, PP 128-134

ABBREVIATIONS AND ACRONYMS

a.m.u	Atomic Mass Units
CNTs	Carbon Nanotubes
CVD	Chemical Vapour Deposition
EDS	Energy Dispersive Spectrometry
IPSF	Infused Polysulfone
MNPs	Magnetic Nanoparticles
MPMS	Magnetic Property Measurement System
MWCNTs	Multiwalled Carbon Nanotubes
NPs	Nanoparticles
PEG	Polyethylene Glycol
SDS	Sodium Dodecyl Sulfate
SEM	Scanning Electron Microscopy
SQUID	Superconducting Quantum Interference Device
SWNTs	Single Walled Carbon Nanotubes
TEM	Transmission Electron Microscopy
TFC	Thin Film Composites
TFN	Thin Film Nanocomposites
XRD	X-ray Diffractometry
UF	Ultrafiltration

ABSTRACT

The search for materials for purification of polluted water is growing daily with the advent of nanoparticles. This is particularly important because many populations of people in the developing countries lack clean water due to water pollution. Water pollutants such as heavy metals and polycyclic aromatic hydrocarbons (PAHs) are known to have adverse effects on humans and environment. This work investigated the potential of synthesized magnetoresponsive CNT-polysulfone infused polymeric nanocomposites (CNT-IPSF) in water purification against heavy metals and polycyclic aromatic hydrocarbons (PAHs) pollution. Adsorption mechanism was studied at constant initial Pb(II) ion concentrations, nanocomposite dosage, contact time, and pH. Carbon nanotubes (CNTs) with internal diameters in the range of 20-30 nm were prepared via chemical vapour deposition (CVD) process. Magnetite and silica coated magnetite nanoparticles (NPs) prepared by solvothermal and sol gel methods respectively exhibited UV-Visible spectrometric spectra at about 395 nm and 396 nm respectively. Successfully synthesized Fe_3O_4 nanoparticles exhibited FT-IR absorption bands at 460 and 521 cm^{-1} which ascribed for the vibrations of Fe-O bond. X-ray diffraction analysis of core shell NPs showed strongest peak at D(311) plane, characteristic of a cubic spinel structure. The core shell nanoparticles obtained displayed a thin hysteresis loop having saturation magnetization of 2.2 emu g^{-1} with ferrimagnetic property. Removal efficiency of the synthesized CNT-PSF/Fe_3O_4 nanocomposite for Pb(II) ions and phenanthrenes was 69 % and 63 % respectively compared to that for a commercially available activated carbon which recorded 54 % and 53 % respectively. Adsorption of Pb(II) ions and phenanthrenes followed pseudo-second-order while Freundlich adsorption isotherm gave the best-fit for the two pollutants. Regeneration for Pb(II) ions of above 60 % and a gradual decrease in desorption efficiency for phenanthrenes of up to 50 % after three desorption cycles confirmed the reusability of the fabricated magnetoresponsive CNT-IPSF/Fe_3O_4 nanocomposites. This study has developed a novel CNT-IPSF/Fe_3O_4 nanocomposite material with higher removal efficiency for water pollutants than commercially available activated carbon for use in water treatment.

CHAPTER ONE

INTRODUCTION

1.1 Background Information

Providing access to safe sustainable drinking water has been identified as one of the most important grand challenges facing scientists in the 21st century. Currently, human society is facing a major hurdle in meeting rising demands of potable water as the available supplies of freshwater are on the decline (Bhattacharya *et al.*, 2013). Many Kenyans especially in the rural areas have limited access to clean water. Due to continued population growth, it has been estimated that by the year 2025, Kenya's per capita water availability will be about two-thirds less than the current 650 cubic meters (Marshall, 2011).

Water pollution is a threat to natural water resources especially in developing countries. Heavy metals and organic compounds represent a large class of pollutants responsible for the pollution of many potential drinking water sources around the world (Shannon *et al.*, 2008). Acute and long-term toxicity of heavy metal ions to man and environment continues to raise major environmental concerns. Major heavy metals that are hazardous to human health include lead (Pb), mercury (Hg), cadmium (Cd), arsenic (As), copper (Cu), zinc (Zn) and chromium (Cr). Metals As and Cd are known to cause cancer, Hg causes mutations and genetic damage, while Cu, Pb and Hg cause brain and bone damage. Heavy metals can also accumulate in living tissues since they are non-biodegradable (Witek-Krowiak *et al.*, 2011).

The outflow of oil spills into water bodies is a chronic problem arising from continuous port activities (Tavakoly *et al.*, 2014). Polycyclic aromatic hydrocarbons (PAHs) are one of the major groups of these organic contaminants (Haritash and

Kaushik, 2009) whose presence in drinking and surface water has generated much public health concern (Okoli *et al.*, 2015). PAHs are semi-volatile contaminants that remain in the environment for long periods due to their high degree of conjugation and aromaticity (Mateen *et al.*, 2015). As a result of their persistence in the environment, they have been classified as priority pollutants with well-established restrictive limits by most environmental regulatory agencies (Muir and Howard, 2006).

Presence of various organic and inorganic pollutants in the effluent calls for specific and effective treatment technique (Gupta *et al.*, 2012). Several processes have been developed and used over the years to remove metal ions, such as chemical precipitation, reverse osmosis, electrolytic recovery, ion exchange or adsorption (Stafiej and Pyrzynska, 2007; Fu and Wang, 2011). Other approaches that utilize biological treatments such as membrane filtration, and adsorption processes have been applied in removal of organic compounds (Shannon *et al.*, 2008). Current water purification techniques involve several technical challenges due to cost implications and are less effective in removal of trace pollutants from water.

Nanotechnology has the potential to increase the effectiveness of the existing water treatment techniques at a more affordable price (Pendergast and Hoek, 2011). Nanotechnology is the design, characterization, production and applications of structures, devices and systems by controlling shape and size at nanometer scale (10^{-9} m). It involves manipulation of materials at atomic, molecular and macromolecular scales, where properties differ significantly from those at a larger scale (Barth *et al.*, 2005). As a result, nanoparticles can be anchored onto a solid matrix such as activated carbon and/or zeolite for enhanced water treatment (Kim and Van der Bruggen,

2010). The adsorption capacity of adsorbent materials is enhanced by the availability of a high number of atoms or molecules on their surfaces (Dhingra *et al.*, 2010).

Magnetoresponsive (MR) materials are a class of smart materials that can form chain-like structures when dispersed in a non-magnetic medium under an applied magnetic field (Felicia and Philip, 2012). When suspended in a non-magnetic liquid such as oil-based fluids, the freely movable particles become polarized when an external magnetic field is applied and connect to the neighbouring particles aligning along them in the direction of the applied magnetic field. The pollutants become trapped in the voids between the particles; the resulting mass is readily removed from the water by magnetic means, after which the pollutant is separated from the particles simply by centrifugation.

In recent years, much attention has been focused on the synthesis of uniformly sized magnetic nanoparticles. Among the magnetic nanoparticles, magnetite has attracted particular interest for several important medical applications such as drug delivery, cancer hyperthermia and magnetic resonance imaging (MRI) enhancement (Wu *et al.*, 2009). Incorporation of such magnetic nanoparticles into suitable polymeric materials can result into functionalized nanocomposites with suitable adsorptive properties for target pollutants during wastewater remediation.

Carbon nanotubes, a member in carbon nanomaterials family, are molecular-scale tubes of graphitic carbon with outstanding properties. The bonding in carbon nanotubes is sp^2, with each atom bonded to three neighbouring atoms with the fourth electron being delocalized over the entire nanotube as the case for benzene giving the nanotube composites amazing mechanical properties (Moghaddam and Pakizeh,

2015). Their highly porous and hollow structure, relatively large specific surface areas and easily modified surfaces has stimulated a lot of research in the area of environmental remediation (Stein *et al.*, 2009). CNTs have been exploited as sorbent materials due to their ability to form molecular complexes through non-covalent bonding (Gojny *et al.*, 2005). Their high loading capacity due to larger surface area makes them perfect templates for self-assembly (Ünal and Niazi, 2013). CNTs can be incorporated into polymeric matrices by the layer-by-layer assembly method (Deshmukh *et al.*, 2013). However, the use of polymers like polysulfone (PSF) has not been studied extensively yet. Therefore, this study focused on the fabrication and characterization of a novel magnetoresponsive CNT-IPSF/Fe_3O_4 nanocomposites consisting of multiwalled carbon nanotubes-polysulfone (CNT-PSF) polymer and silica-coated magnetite ($SiO_2 \cdot Fe_3O_4$) nanoparticles for water purification.

1.2 Statement of the Problem

Water pollution is mainly caused by discharge of industrial effluent with significant amounts of heavy metals and oil spills into water bodies (Verstraete *et al.*, 2009). Heavy metals have several effects on man such as nausea and vomiting (Cd), lung damage (Pb) and blood pressure (Hg). Polycyclic aromatic hydrocarbons (PAHs) are a major component of oil spills with serious effects on man such as cataracts (anthracene), liver and kidney damage (phenanthrenes), and destruction of red blood cells (nanphthalene).

Cattle grazing along highway road and nearby rivers/streams have their milk contaminated with heavy metals and PAHs from oil spill (Trombulak and Frissell, 2000). The recent lead poisoning by emission of toxic fumes from nearby metal refineries EPZ Ltd was reported on the Owino-Uhuru community in Mombasa.

Untreated waste water from the plant spilled into streams which residents used for washing and cooking. Children living nearby developed fevers and stomach problems and pregnant women had miscarriages and stillbirths (Kamonji, 2012).

Major conventional methods employed in removal of these pollutants include membrane filtration and separation, reverse osmosis, ion exchange, and physical/chemical treatment. However, these are faced with several technical challenges such as cost, expertise and reuse that reduce their usability in removing low concentration contaminants from water (Shannon *et al.*, 2008). A search for materials with specific properties that can significantly remove nanoscale pollutants is therefore a priority. The focus of this work was to develop nanomaterials and use them in fabricating nanocomposites with suitable properties to be used in water purification.

1.3 Justification

This study aimed at fabricating CNT-IPSF/Fe_3O_4 nanocomposites from CNTs and silica coated magnetite nanoparticles for removal of heavy metals and PAHs from polluted water. This is because the commercially available materials such as activated carbon are less efficient in removing trace levels of water pollutants. Nanomaterials such as carbon nanotubes have delocalized electrons that can remove PAHs through π-π interactions while the metal ions can be removed by ion exchange interaction on positively charged magnetite nanoparticles. The fabricated CNT-IPSF/Fe_3O_4 nanocomposites have nanosized particles of CNTs and core shell nanoparticles incorporated into a matrix of standard material with drastic improvement in properties such as mechanical strength, toughness, electrical or thermal conductivity. These materials are fabricatable and readily available for use on individual level.

1.4 Hypothesis

CNT-IPSF/Fe_3O_4 nanocomposites are efficient adsorbents in the removal of both heavy metals and polycyclic aromatic hydrocarbon (PAHs) pollutants from contaminated water

1.5 Objectives

1.5.1 General Objective

To fabricate and characterize novel magnetoresponsive CNT-IPSF/Fe_3O_4 nanocomposites consisting of carbon nanotube infused polysulfone (CNT-IPSF) polymer and silica-coated magnetite ($SiO_2 \cdot Fe_3O_4$) nanoparticles and investigate their application in water purification.

1.5.2 Specific Objectives

i) To fabricate and characterize CNT-IPSF/Fe_3O_4 nanocomposite from CNT-IPSF polymer and $SiO_2 \cdot Fe_3O_4$ nanoparticles

ii) To investigate the efficiency of the CNT-IPSF/Fe_3O_4 nanocomposites in the removal of Pb^{2+} ions and Phenanthrene

iii) To investigate the feasibility for regeneration of the nanocomposite for reusability.

1.6 Significance of the Study

Kenya is a developing country with its development agenda outlined in the Vision 2030 blue-print. The government of Kenya's strategy for water resources is to reduce wastewater pollution by improving technology on wastewater management. However, it still incurs costs combating waterborne diseases in many parts of the country (Corcoran, 2010). Development of new technologies towards new adsorbents for

water purification still attracts a lot of interests from industrial partners to fill the gap. This study aimed at developing a new nanocomposite material that has ability to remove both organic and inorganic water pollutants from wastewater during water purification. Therefore:

i) The findings of this study adds to the existing body of scientific knowledge on the fabrication of polymeric composites using non-toxic magnetite coated with silica as a surface functionality for attachment by polymer. These materials have proven effective in removal of organic pollutants (such as polycyclic aromatic hydrocarbons) and heavy metal ions (such as lead (II) ions).

ii) The fabrication, characterization and optimization of CNT-IPSF/Fe_3O_4 nanocomposites is important since these smart materials will find potential application in both large and small scale water purification through the use of nanotechnology.

iii) This research leads to preparation of a novel nanostructured adsorbent membrane system with higher efficiencies than locally available materials for the treatment of wastewater at the point of use (POU) for safe drinking

iv) This study also advances scientific knowledge on fabricating fibrous materials for use in other manufacturing and industrial processes.

1.7 Scope and Limitations of the Study

This study fabricated CNT-IPSF/Fe_3O_4 nanocomposites from synthesized carbon nanotubes and magnetite silica nanoparticles. These materials were used to investigate the removal of lead (II) ions and phenanthrenes from water as they are the most toxic pollutants on the US Environmental Protection Agency (EPA) list of priority

pollutants. The study investigated the removal of lead (II) ions and phenanthrenes and not a whole range of heavy metals and polycyclic aromatic hydrocarbons (PAHs). The co-existence of heavy metals (HMs) and polycyclic aromatic hydrocarbons (PAHs) is very common in contaminated environments (Ma *et al.*, 2014). Combined effects in organisms from co-exposure to heavy metals and PAHs have therefore been a subject of observational and experimental studies (Sigel *et al.*, 2011). It is of paramount importance to exploit bioremediation to remove PAHs with combined pollution in these environments

Lead was selected as metal pollutant because of its toxicity and affecting fundamental biochemical processes e.g. inhibiting actions of calcium and interacting with proteins (Patrick, 2006). Continued exposures can cause a toxic stress on the kidney and can inhibit body's ability to produce hemoglobin by interfering with several enzymatic steps in the heme pathway. Lead interferes with a hormonal form of vitamin D, which affects multiple processes in the body, including cell maturation and skeletal growth. Lead exposure may contribute to hypertension and may also diminish sperm concentrations leading to total sperm motility.

Phenanthrene is a low molecular weight, 3-ring polyaromatic hydrocarbon (PAH), and a toxic pollutant pursuant to Clean Water Act (Cohen, 2000). Researchers have reported increased incidences of skin, lung, bladder, liver, and stomach cancers. Phenanthrene can affect the immune systems and also produce reproductive, neurologic, and developmental effects. Phenanhrene coexists with other organic compounds such as alkyl PAHs which are highly toxic (Andersson and Achten, 2015). Some alkyl PAHs tend to be less volatile than parent compound PAHs while others tend to bioaccumulate to a greater degree. This necessitates its removal before

it can undergo further reactions to form complex PAHs compounds which would otherwise be difficult to remove.

Acetylene/argon flow rate was limited to 8 cm^3/min and 1 cm^3/min respectively. Synthesis of carbon nanotubes (CNTs) was done by CVD within working temperature range of 600-700 °C suitable for multiwalled CNTs. The efficiency of the CNT-IPSF/Fe_3O_4 nanocomposites in removal of Pb(II) ions and phenanthrenes was only compared to that of other Fe_3O_4 based adsorbents.

CHAPTER TWO

LITERATURE REVIEW

2.1 Introduction

This chapter underscores useful properties of specific nanomaterials used in fabricating CNT-IPSF/Fe_3O_4 nanocomposites. It examines the synthetic methods for carbon nanotubes and magnetic iron oxides as components of the nanocomposite. Various functionalization techniques are discussed in relation to improving their properties. This is followed by a description of working principles of the relevant equipment employed. It concludes with a summary of key knowledge issues, controversies in literature and how the research gaps were addressed by the research study.

2.2 Fabrication of Nanocomposites

Polymer matrix based nanocomposites have generated a significant attention in the area of nanotechnology, due to decrease of particle dimension to nanoscale. Nanocomposites are a class of materials in which one or more phases with nanoscale dimensions (0-D, 1-D, and 2-D) are embedded in a metal, ceramic, or polymer matrix (Kuchibhatla *et al.*, 2007). Addition of the nanoscale second phase creates a synergy between the various constituents, thus achieving design expectations. The matrix material and interactions between the matrix and the second phase determines the properties of nanocomposites. The second phase (usually a few percent by weight, wt%), which is dispersed within the matrix, has nanoscale dimensions. The interface-to-volume ratio is significantly higher than in conventional composites due to nanoscale size of the reinforcing phase (Zhang *et al.*, 2010). This reduces the volume fraction of the second phase without degradaing the desired properties.

There are three categories of nanoscale reinforcing phase, namely, nanoparticles (0-D), nanotubes (1-D), and nanoplates (2-D). Particle size and distribution plays a great role in the case of nanoparticles. The type of nanoparticles added alters mechanical, electrical, optical, and thermal properties of polymer nanocomposites. The smaller size of nanoparticles is responsible for composites' reinforcement through improved toughness and strength (Fu *et al.,* 2008). However, agglomeration of nanoparticles should be prevented at all costs as small levels of agglomeration decrease the strain-to-failure by several tens of percent.

The nanoparticles should be as small as possible while the index of refraction should remain as similar as possible to the matrix in order to achieve transparency. Excellent use of nanoparticles in polymer nanocomposites through controlled refraction index can be achieved by tailoring the volume fraction of nanoparticles (Althues *et al.*, 2007). This behavior has been shown in polyethylene polymer films filled with silver nanoparticles. The addition of nanoparticles of silica to polyimide has been used to control the transmittance in these nanocomposites.

Studies on the current wastewater treatment technologies have shown limitations in providing adequate water quality for human needs (Malato *et al.*, 2009). More effective, lower cost, robust methods to decontaminate water from source to point-of-use, without further endangering the environment or human health are needed. Although membrane processes can be applied in small-scale water treatment systems, they can become clogged in the event that such water is not initially filtered (Gadipelly *et al.*, 2014). Maintenance can be generally expensive due to regular replacement of these membranes as may be required.

Modern conventional water treatment plants are mainly characterized by a high degree of mechanization and automation. Improved water treatment techniques are vital for effective removal of emerging contaminants. Appropriate, relevant and sustainable technology which is economically friendly needs to be developed in regard to sustainable water technologies (Epstein and Buhovac, 2014). Implementation of such technology needs the cooperation from governments and stakeholders in order to harness any meaningful benefits.

2.3 Nanomaterials

In the past decade, the study of nanomaterials has received particular interest from various researchers due to their exceptional features and properties (Callister and Rethwisch, 2012). Nanomaterials' volume influences the number of atoms present on nanomaterial surface, i.e. an excitation of surface atoms results into a blue shift in optical absorption spectra, with a higher number of atoms being reduced. Nanomaterials exhibit very important properties based on the nanoparticles which they are composed of (Sanchez *et al.*, 2011). Unique property of these nanomaterials is that most of the atoms have high chemical activity and adsorption capacity to many metal ions on the surface of the nanomaterials (Ray, 2010). The surface atoms are unsaturated and are thus subject to combination with other element ions by static electricity. This leads to attachment of lighter metal ions and charged organic molecules onto the nanometerials surface. Although there are many classes of nanomaterials (NMs) (Figure 2.1), main focus was on carbon nanomaterials, nanoparticles and polymeric nanocomposite formation due to their relevance to this study.

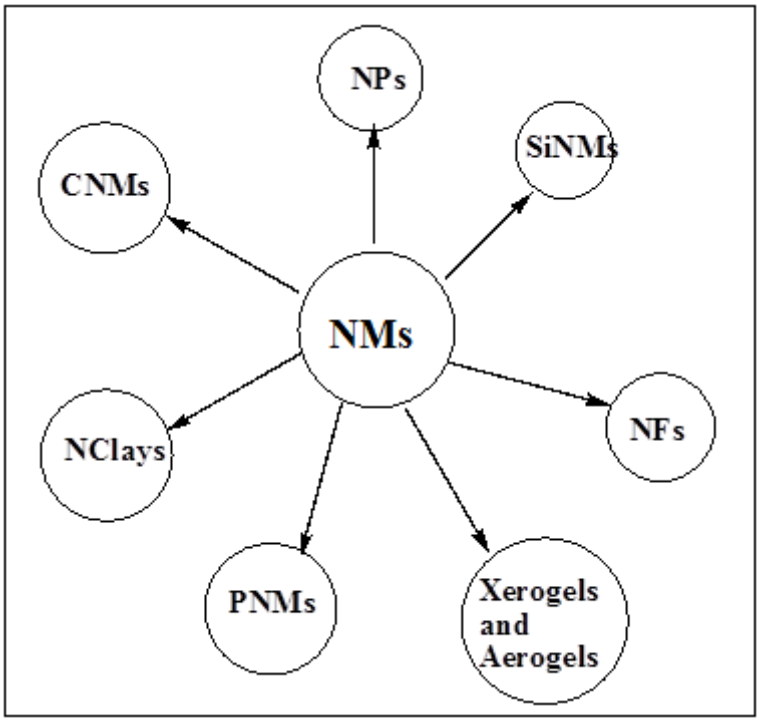

Figure 2. 1 Classification of nanomaterials (Berube *et al.*, 2011)

2.3.1 Carbonaceous Nanomaterials (CNMs)

Carbon nanotubes are made of hollow graphitic layers of graphene sheets which are of two types: the single walled carbon nanotubes (SWNTs) and the multiwalled carbon nanotubes, (MWCNTs) (Figure 2.2) (Trojanowicz, 2006). The lengths and diameters of SWCNTs and MWCNTs are in the orders of several micrometers and nanometers respectively.

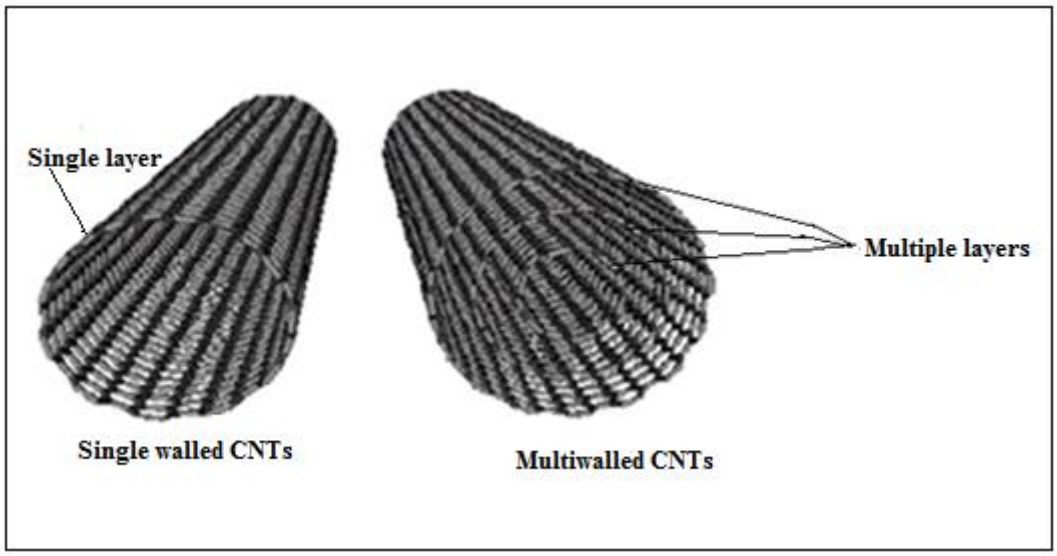

Figure 2. 2 Illustrations of (a) SWCNTs and (b) MWCNTs (Trojanowicz, 2006)

Carbon nanotubes (CNTs) have been proved as better adsorbents than activated carbon for removal of many heavy metals (Alslaibi *et al.*, 2013). Due to the multilayer nature of MWCNTs, the outer walls shield the inner carbon nanotubes from chemical interactions with outside substances (Aliofkhazraei *et al.*, 2016). Under high compressive forces, MWCNTs can bend, twist, and finally buckle without significant damage. They can withstand high temperatures (750 − 2,800 °C) as a result of their strong atomic bonds. In fact, carbon nanotubes may possess many pores which act as hosts to incoming pollutant molecules.

The structure of carbonaceous materials consists of well-defined energy or band gaps separating the valence and conduction bands (Wei *et al.*, 2009). The adsorption of incoming molecules into the carbonaceous materials results in their high aspect ratios. Furthermore, creation of a large number of inter-tubular spaces acts as suitable sites for adsorption. This leads to high mass transfer due to strong solute-sorbent interactions leading to fast adsorptions. The release of such adsorbates by solvent washing has the advantage of its relative simplicity with no effect of diffusion.

Strong capillary forces in nanotubes may allow for interactions between CNTs and target pollutants through either van der Waals attractive forces or dipole−induced-dipole interactions (Zare *et al.*, 2015) and can facilitate adsorbents orientation for the sorbate molecules. The CNTs removes many of the polar pollutants due to the *pi-pi* (π-π) interactions, hydrogen bonding, covalent bonding, and electrostatic interactions. The **π** electron rich CNT surface allows **π-π** interactions with organic molecules having C=C bonds or benzene rings, such as polycyclic aromatic hydrocarbons (PAHs). Organic compounds which have -COOH, -OH, $-NH_2$ functional groups could also form hydrogen bond with the graphitic CNT surface (Peng *et al.*, 2012). The hydrogen bonds of the interfacial organic molecules form between the first two layers of the double-layer structure and also within each layer. This hydrogen-bond network is confined within the double layer, which means that no "dangling hydrogen bonds" appear on the surface of the double-layer structure. This formation of hydrogen bonds stabilizes the double-layer structure and makes its surface hydrophobic hence graphene surface is perfectly wettable on the atomic scale and becomes hydrophobic once it is covered by this double layer of organic molecules (Akaishi *et al.*, 2017).

2.3.2 Synthesis of Carbon Nanotubes (CNTs)

There exist three major categories of techniques for synthesizing carbon nanotubes: the laser ablation, catalytic arc discharge, and CVD (Harris, 2009). A number of carbon sources such as acetylene, ethylene, propylene, methane, benzene, toluene etc. or other carbon feedstock are heated to higher temperatures in argon atmosphere in presence of a catalyst. The catalyst material usually in solid form is placed on ceramic crucibles inside the furnace before heating. Decomposed carbon species dissolve in the metal nanoparticles until supersaturation is reached followed by carbon precipitation.

Chemical vapour deposition CVD method allows synthesis of CNTs giving a variety of forms, such as powder, thin or thick films aligned or entangled straight or coiled nanotubes at predefined sites on a substrate (Szabó *et al.*, 2010). Chemical vapour deposition has better control over growth parameters than other synthesis methods. Carbon source, catalyst and growth temperature are the three main parameters for CNTs synthesis in the CVD. Multiwalled carbon nanotubes (MWCNTs) are formed at low-temperature (600–900 °C) while single walled carbon nanotues (SWCNTs) form at higher temperature (900–1,200 °C). Transition metals such as Fe, Co, Ni are the most commonly used catalysts for CNTs growth. Argon is used to provide the inert atmosphere.

The main impurities in CNTs synthesis is the nontubular carbons (NTCs) which form alongside the desired CNTs (Fan *et al.*, 2006). Several oxidation purification methods such as acid treatment are employed to remove the impure NTCs. More importantly, these procedures generate oxygen-containing functional groups, for example OH, C=O, and COOH, which increase the polarity, hydrophilicity, and ion-exchange capability of the CNTs. However, CNT fragmentation limits any given acid-oxidation procedure. Dispersion of the CNTs agglomerates using high ultrasonic power contributes towards undesired fragmentation.

2.3.3 Functionalization of CNTs

Many nanomaterials with distinct external functionalization features are desirable due to enhancement of their surface properties for excellent adsorption studies (Gorjizadeh and Kawazoe, 2010). Attachment of functional groups onto the nanomaterials induces unique characteristics to the adsorbents such as high selectivity and rapid desorption (Khajeh *et al.*, 2013). The interactions of nanomaterial's surface

with the analytes of interest through attachment of various moieties lead to improved hydrophilicity or polarity of adsorbent. Amino and oxygen groups are known to coordinate to transition metals via electrostatic interactions. Velickovic *et al.* (2013) functionalized MWCNT with ethylenediamine by amide bond formation via the carboxyl groups on the oxidized CNT surface (Figure 2.3) and quantified Cd(II) uptake from water samples (Veličković *et al.*, 2013).

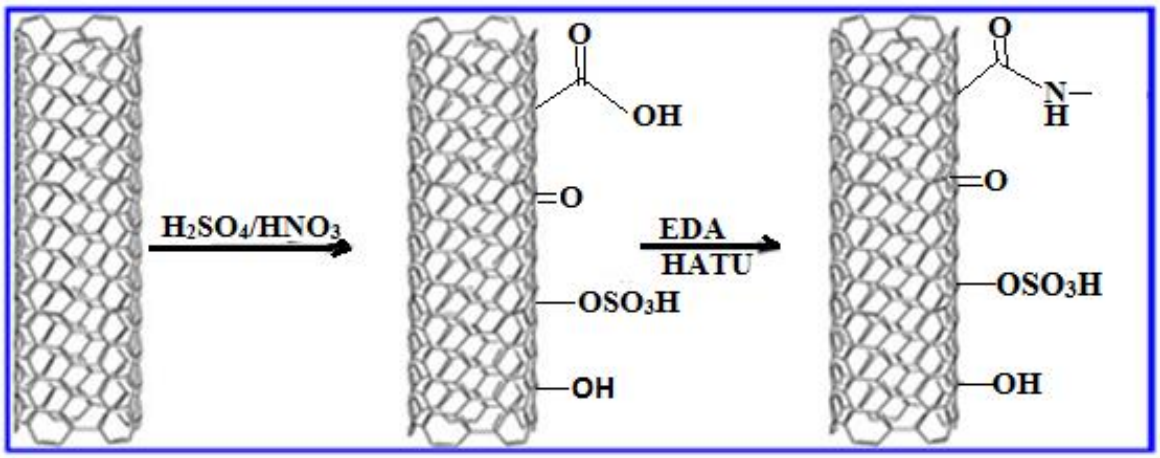

Figure 2. 3 CNTs functionalization process (Spitalsky *et al.*, 2010)

The oxidation of CNTs can introduce functional groups such as hydroxyl, carboxyl, and carbonyl groups on the CNTs surface (Abuilaiwi *et al.*, 2010). Examples of such oxidizing agents are nitric acid, hydrogen peroxide, potassium permanganate e.t.c. The oxidation of CNTs leads to their increased surface area through removal of impurities and the attachment of oxygen-containing functional groups. During such oxidation processes, the end tips open up creating more surface defects which makes such point to be active sites for further reactions (Musameh *et al.*, 2011). The creation of active sites leads to formation of surface charge which is determined by the pH and ionic strength of the solution (Xu *et al.*, 2005). In fact, the determination of pH at point of zero charge (pH_{PZC}) provides information on whether a nanomaterial will adsorb at lower or higher pH than the pH_{PZC}.

2.4 Nanoparticles (NPs)

The nature of nanoparticles largely depend on their independent compositions and dependent surface structures (Sun *et al.*, 2012). The physical and chemical properties of nanoparticles usually deviate from those in their bulk form due to a decrease in their particle sizes. Furthermore, many of the atoms exist on or near their surfaces (Kucki *et al.*, 2013).

2.4.1 Magnetic Nanoparticles

Properties of magnetic nanopartcles are determined by many factors such as the chemical composition, the type of the crystal lattice, the particle size and shape, the morphology (for structurally non-homogeneous particles), the interaction of the particle with the surrounding matrix, and the neighboring particles (Baaziz *et al.*, 2014). By manipulating nanoparticle size, shape, composition and structure, the magnetic characteristics of the material can greatly be controlled. The use of iron oxide MNPs has found extensive applications in a variety of fields. Both forms of iron oxide nanoparticles, Fe_3O_4 (magnetite) and Fe_2O_3 (maghemite), have superparamagnetic properties (Qu *et al.*, 2013). Such nanoparticles easily respond to a magnetic field, but after the field is removed no magnetic property remains due to negligible remanence and coercivity.

Such property is suitable in many separation applications in which there is no possibility of agglomeration. Providing shell around magnetic nanoparticles protects them against degradation (Lu *et al.*, 2007). Magnetic separation is achieved through mixing particles with affinity to target species within the heterogeneous solution. External magnetic fields are then applied to separate the tagged particles from the solution.

2.4.2 Nanoparticles as Adsorbents

Nanoparticles with sizes of between 1−100 nm find key applications in many research fields such as chemistry and material sciences (Mahmoudi *et al.*, 2011). The use of metal and metal oxide nanoparticles as conventional sorbents in separation techniques has resulted in excellent morphological properties for adsorption purposes (Ren *et al.*, 2011). The high surface area of magnetic nanoparticles makes them suitable sorbents in separations using applied magnetic field (Ghosh and Paria, 2011). However, it should be pointed out that pure inorganic nanoparticles (such as Fe_3O_4 and Fe_2O_3) can easily form large aggregates, which may alter their magnetic properties. Modification of nanoparticle surface via organic chelating groups greatly minimizes aggregate formation (Li *et al.*, 2011).

2.5 Synthesis of Iron Oxides Nanoparticles

During the last few years, a large portion of the published articles have described efficient routes towards attaining shape-controlled, highly stable, and narrow size distribution magnetic nanoparticles (MNPs) (Khandhar *et al.*, 2012). Magnetite (Fe_3O_4) or its oxidized form maghemite (γ-Fe_2O_3) are by far the most commonly employed nanoparticles that possess Fe^{3+} cations occupying tetrahedral sites and octahedral sites of a cubic inverse spinal structure in an 'fcc' closed packing (Umut, 2013). In this section, a number of synthetic methods and their mechanisms are discussed.

2.5.1 Solvothermal Method

A solvothermal process is a chemical reaction (or a transformation) between precursor(s) in a solvent (in a close system) at a temperature higher than the boiling temperature of this solvent and under high pressure (Figure 2.4). The solvothermal

method is almost identical to the hydrothermal method except that the solvent used here is non-aqueous. The temperature can be elevated much higher than that in hydrothermal method. The solvothermal method normally has better control than hydrothermal method in terms of the size and shape distributions, and the crystallinity of the nanoparticles.

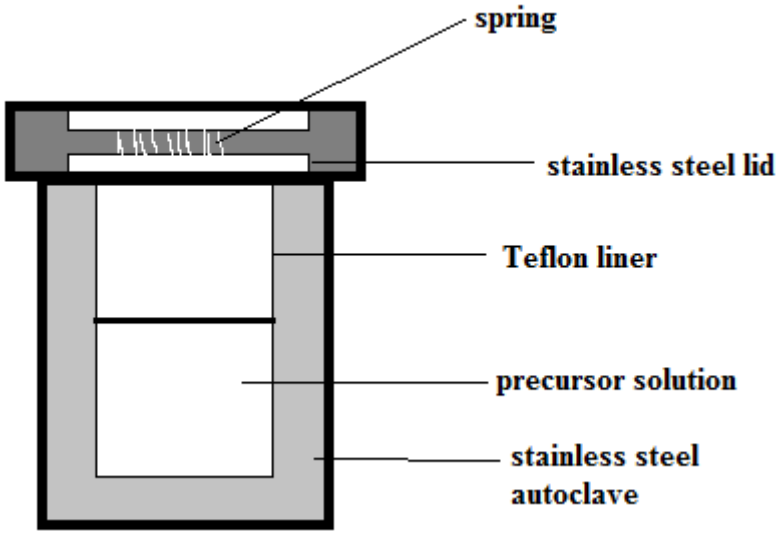

Figure 2. 4 Set-up for solvothermal process

A typical synthesis procedure involves hydrolysis of Fe^{3+} salt followed by addition of ethylene glycol to form $Fe(OH)_2$ and finally reacting the $Fe(OH)_2$ formed with $Fe(OH)_3$ to form Fe_3O_4 as shown by equations 2.1 - 2.3 (Tian *et al.*, 2011);

$$Fe^{3+} + 3OH^- \rightarrow Fe(OH)_3 \quad \textbf{2.1}$$

$$10Fe(OH)_3 + C_2H_6O_2 \rightarrow 2H_2CO_3 + 10Fe(OH)_2 + 6H_2O \quad \textbf{2.2}$$

$$2Fe(OH)_3 + Fe(OH)_2 \rightarrow Fe_3O_4 + 4H_2O \quad \textbf{2.3}$$

The Fe_3O_4 fine particles prepared had a better crystallinity and highly uniform sizes. The advantage of this method is that the size of the synthesized magnetite

nanoparticles can be controlled easily through adjusting reaction temperature in the ethylene glycol.

2.5.2 Sol Gel Process

Sol-gel process is a wet chemical process for the synthesis of colloidal dispersion of inorganic and organic inorganic hybrid materials (Brinker and Scherer, 2013). In the sol-gel method, sols are formed by the addition of organic molecules (OMs) to Fe(III) ions colloidal dispersions. The Fe_3O_4 is finally formed by some thermal treatment of the concentrated solution (gel) obtained. A simple scheme of sol-gel method for iron oxides synthesis is shown in figure 2.5.

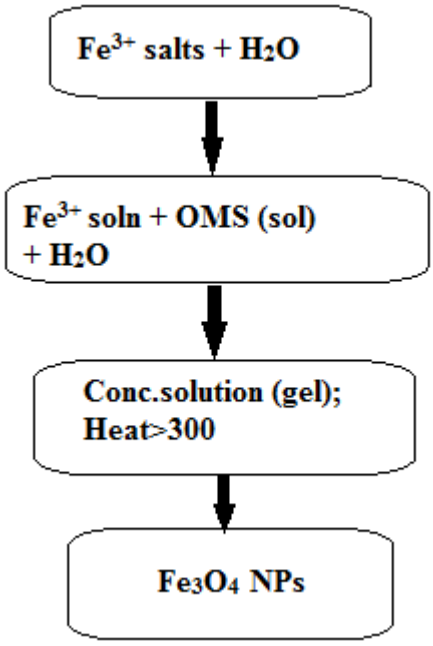

Figure 2. 5 Flow diagram of the sol gel process

The precursors can be hydrolyzed by an acid or base besides using water as solvent. The formation of a polymeric form of the gel is induced by acid catalysis at room temperatures. The final crystalline state of the product is obtained by further heat treatment (Equations 2.4 - 2.5);

$$Fe^{3+} + H_2O \xrightarrow{deprotonation} Fe(OH)_x^{3-x} \quad \textbf{2.4}$$

$$Fe^{3+} + H_2O \xrightarrow{Oxidation} \xrightarrow[pH\ 9,\ Temp\ 60^0]{Dehydration} Fe_3O_4 \quad \textbf{2.5}$$

The synthesis of metal oxides by sol-gel synthesis has proven extremely versatile since it allows the formation of a large variety of metal oxides at relatively low temperatures. The main advantages of sol-gel process are (i) pure, monodispersed materials with a predetermined structure are obtained, (ii) the particle size and its microstructure are well controlled, and (iii) the ability of the embed molecules to maintain their stability and properties within the sol-gel matrix.

However, this method leads to generation of a 3-D oxide networks which limits its efficiency during the formation of independent, disconnected nano sized particles (Ochanda *et al.*, 2009).

2.5.3 Co-Precipitation

Co-precipitation is the formation of precipitates at higher temperatures through addition of an alkali e.g. ammonium hydroxide to a mixture of soluble Fe^{2+} and Fe^{3+} ions salts. Iron oxides (Fe_3O_4 or γ-Fe_2O_3) are usually prepared by addition of alkali to iron salt solutions and keeping the suspensions for ageing. The hydroxylation of the ferrous and ferric ions under anaerobic conditions at pH > 8 leads to the formation of black precipitates of the Fe_3O_4 MNPs (Jolivet *et al.*, 2004). The main reactions taking place in the formation of black Fe_3O_4 MNPs is outlined in equations 2.6 - 2.9;

$$Fe^{3+} + 3OH^- \rightarrow Fe(OH)_3 \quad \textbf{2.6}$$

$$Fe(OH)_3 \rightarrow FeOOH + H_2O \quad \textbf{2.7}$$

$$Fe^{2+} + 2OH^{-} \rightarrow Fe(OH)_2 \text{.....} \textbf{2.8}$$

$$2FeOOH + Fe(OH)_2 \rightarrow Fe_3O_{4\downarrow} + 2H_2O \text{.....} \textbf{2.9}$$

The above reactions take place very fast and the black crystals form immediately upon addition of the FeOOH. It is required that the whole process takes place in the absence of air/oxygen to prevent the synthesized crystals from oxidation into ferric hydroxide (γ-Fe_2O_3). In order to produce good, uniform and monodispersed nanoparticles, it is necessary to avoid nucleation during growth process (Ziegler and Eychmüller, 2011).

Co-precipitation process takes advantage of the large amount of nanoparticles synthesized at the end of the process. This technique is the simplest and most efficient chemical pathway to obtain iron oxide nanoparticles despite the fact that the control of particle size is limited since kinetic factors are controlling the growth of the crystal. The low-temperatures applied in co-precipitation method together with well controlled nanoparticle sizes gives this method an added advantage against other conventional powder synthesis techniques (Nidhin *et al.*, 2008). This process leads to production of ultrafine particles with high-purity (Chen *et al.*, 2005).

Magnetite nanoparticles are known to have higher surface to volume ratios leading to high surface energies. This results in minimization of their surface energies through particle aggregation. Moreover, magnetite core nanoparticles are susceptible to loss of some magnetism through oxidation. In many cases, such side reactions are avoided by providing inert shell on the core nanoparticles to maintain the stability of the synthesized magnetic iron oxide NPs. Silica coating has shown success in providing such protective layer around the nanoparticles in addition to further functionalization

for the core shell nanoparticles (Wu *et al.*, 2009). The other problem of nanoparticles is aggregation which normally affects dispersibility of the nanoparticles. Surfactants such as oleic acid employs the strong chemical bond between the carboxylic acid in oleic acid and the amorphous layer of the iron oxide nanoparticles to stabilize the nanoparticles (Wu *et al.*, 2004).

2.5.4 Thermal Decomposition

Thermal decomposition, or thermolysis, is a process by which a compound chemically decomposes by breakdown of chemical bonds in its structure. Much success in synthesizing Fe_3O_4 nanoparticle with controlled size has only been achieved through thermal decomposition. The decomposition of $Fe(acac)_3$ (acac-acetylacetonate), or $Fe(CO)_5$ followed by oxidation can lead to high-quality monodispersed iron oxide NPs at relatively higher temperatures. Some attempts have been made towards replacing $Fe(CO)_5$ with iron acetylacetonate [$Fe(acac)_3$] since $Fe(CO)_5$ is very expensive and toxic. The production of Fe_3O_4 nanoparticles produced in this case were of narrow size distribution (Sun *et al.*, 2004). The synthesis of nanoparticles with narrow diameter distribution, high saturation magnetic moment and magnetic stability using non-toxic chemicals has been a challenging task which is possible with thermal decomposition method.

2.5.5 Microemulsion

Microemulsion method involves dispersion of two immiscible phases especially a hydrocarbon and water in the presence of a surfactant (McClements, 2012). At the interface between the oil and water, the hydrophobic and the hydrophilic tails of the surfactant molecules dissolve in the oil phase and aqueous phase respectively. Some of the surfactants employed in this process are sodium lauryl sulfate, triton X, and

polyethylene glycol (Vidal *et al.*, 2006). The exchange of reactants between the phases is facilitated by the dispersion of water/oil droplets in a continuous phase (Dong *et al.*, 2002). There are three specific classes of droplet type microemulsions: oil-in-water (o/w, meaning spherical oil droplets dispersed in water), water-in-oil (w/o, i.e. spherical water droplets dispersed in oil) and water-in-supercritical carbon dioxide (w/sc-CO_2 which stands for water droplets dispersed in supercritical carbon dioxide). Many metal oxide nanoparticles like SiO_2, GeO_2, TiO_2 and Fe_2O_3 have been synthesized using the microemulsion route (Figure 2.6).

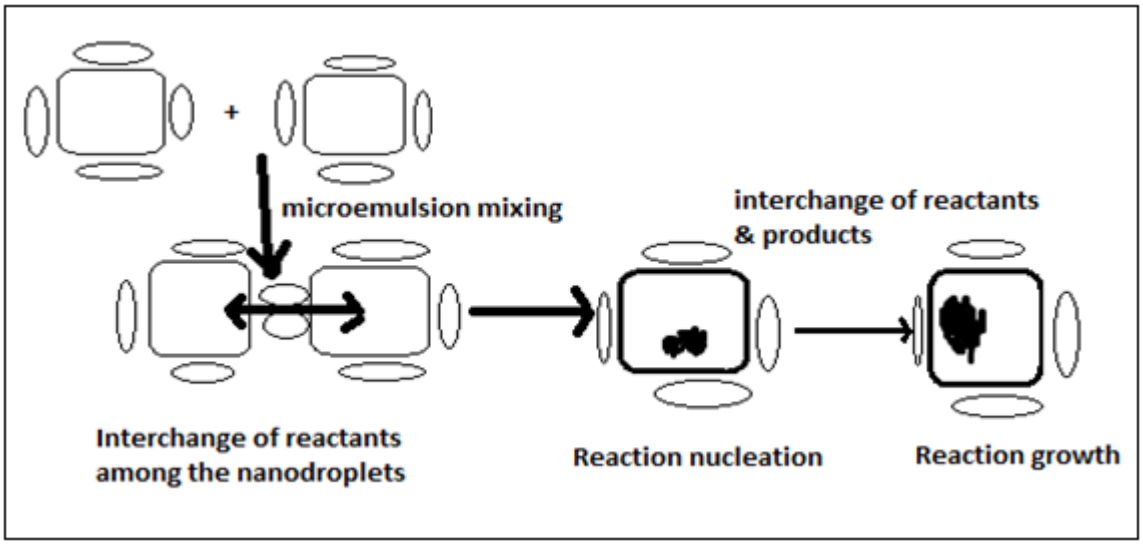

Figure 2. 6 Flow diagram for microemulsion process

Microemulsion has been proved as an efficient route for nanoparticles synthesis. Hexagonal nanostructured hematite has been synthesized by mixing $FeCl_3$ and NH_4OH overnight in microemulsion systems in order to achieve equilibrium. However, expensive oils and surfactants coupled with low yield, and difficult in removal of product from the emulsion are some of the disadvantages of this method (Tavakoli *et al.*, 2007). The aggregation of the produced NPs can be eliminated through several washing processes and further stabilization treatments.

2.5.6 Hydrothermal Synthesis

Hydrothermal synthesis is a method of crystallizing substance in a sealed container (autoclave) from high temperature aqueous solution (130 to 250 °C) at high vapour pressure (0.3 to 4 MPa) (Ahmad and Phul, 2015). At elevated temperatures, reactants dissolve forming fluids with different physico-chemical properties. A simple hydrothermal route for hematite synthesis involves reaction of ammonium ferrous sulfate with hydrazine hydrate in a Teflon lined autoclave of 200 ml capacity at pH of 3-5 as shown in equation 2.10;

$$N_2H_4 + Fe^{2+} + 4H_2O \xrightarrow{pH\ 3-5} 2NH_4 + 2H^+ + 2\alpha\text{-}FeOOH \xrightarrow{150^0C} \alpha\text{-}Fe_2O_3 + H_2O \ldots \textbf{2.10}$$

The simplicity and versatility coupled with the possibility of synthesized nanoparticles exhibiting good morphology and percent yield are some of the advantages of this method (Lu *et al.*, 2007). Such process leads to formation of nanoparticles with diameters of 27 nm and a saturation magnetization of 20 emu g^{-1} at room temperature.

2.5.7 Sonochemical Synthesis

This is a chemical reaction driven by intense ultrasonic waves, which are strong enough to cause dissolution, oxidation and hydrolysis. Ultrasonic irradiation of aqueous liquids generates free H^+ and OH^- radicals. These radicals can recombine to produce H_2 and H_2O_2. These resultant strong oxidants and reductants in turn are utilized during various sonochemical reactions (Equations 2.11 – 2.14) in aqueous solutions (Bang and Suslick, 2010);

$$H_2O \rightarrow H^+ + OH^- \quad \ldots\ldots\ldots\ldots\ldots\ldots\ldots\ldots\ldots\ldots \textbf{2.11}$$

$$H^+ + H^+ \rightarrow H_2 \quad \ldots\ldots\ldots\ldots\ldots\ldots\ldots\ldots\ldots\ldots\ldots\ldots \textbf{2.12}$$

$$OH^- + OH^- \rightarrow H_2O_2 \ldots\ldots\ldots\ldots\ldots\ldots\ldots\ldots \textbf{2.13}$$

$$FeSO_{4(s)} \rightarrow Fe^{2+}_{(aq)} + SO^{2-}_{4(aq)} \ldots\ldots\ldots\ldots\ldots\ldots \textbf{2.14}$$

The oxidant H_2O_2 then initiates oxidation of Fe^{2+} (Equation 2.15 – 16);

$$2Fe^{2+} + H_2O_2 \rightarrow 2Fe^{3+} + 2OH^- \ldots\ldots\ldots\ldots\ldots\ldots \textbf{2.15}$$

$$Fe^{2+} + 2Fe^{3+} + 8OH^- \rightarrow Fe_3O_4 + 4H_2O \ldots\ldots\ldots \textbf{2.16}$$

The set-up for sonochemical experiments is shown in figure 2.7.

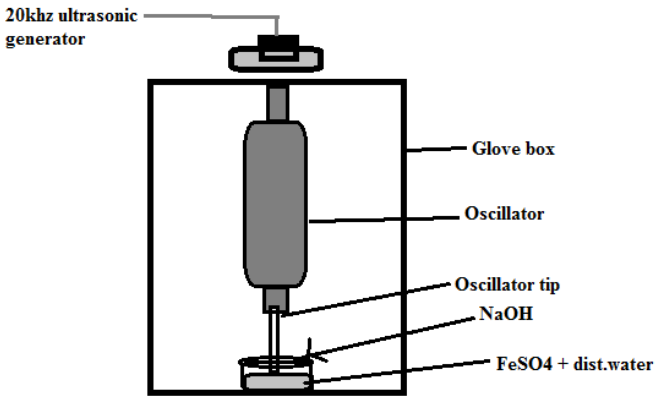

Figure 2. 7 Set-up for Sonochemical process

Vijayakumar *et al.* (2000) reported a sonochemical synthetic route for preparing the pure nanometer-size Fe_3O_4 powder with particle size of 10 nm (Vijayakumar *et al.*, 2000). The prepared Fe_3O_4 NPs had very low magnetization value of 1.25 $emug^{-1}$ at room temperature revealing their superparamagnetic property. Wu *et al.* (2008) has recently developed a sonochemical synthetic method for preparing amorphous nanoscopic iron oxide by sonolysis of $Fe(acac)_3$ under Argon. This process produced nanoparticles with high magnetization values (Wu *et al.*, 2008).

Although these methods have their successes, they have low control over particle shape and sizes. Furthermore, the synthesized nanoparticles suffer from aggregation and oxidation. In the following section, various methods for functionalizing iron oxide NPs are discussed.

2.6 Functionalization of Iron Oxides Nanoparticles

2.6.1 Silica Coated Nanoparticles

Coating magnetic nanoparticles with silica via sol-gel approach has shown progress in the synthesis of magnetic nanoparticles. Silica is a material that is widely used in many sample preparations due its chemical inertness which protects the magnetic core from leaching in acidic environment. Silica is also capable of forming abundant silanol groups on its surfaces making it hydrophilic, a necessity in further modifications (Zhang and Zhao, 2009). Finally, the modified nanoparticles are able to provide more adsorptive sites for rapid and quantitative adsorption of Cd^{2+}, Cu^{2+}, Hg^{2+}, and Pb^{2+} ions. The silica particles are used to synthesize the core shell nanoparticles using modified Stöber approach (Figure 2.8). The amount of silica content added and the reaction process determines the thickness of the shell on the core particles.

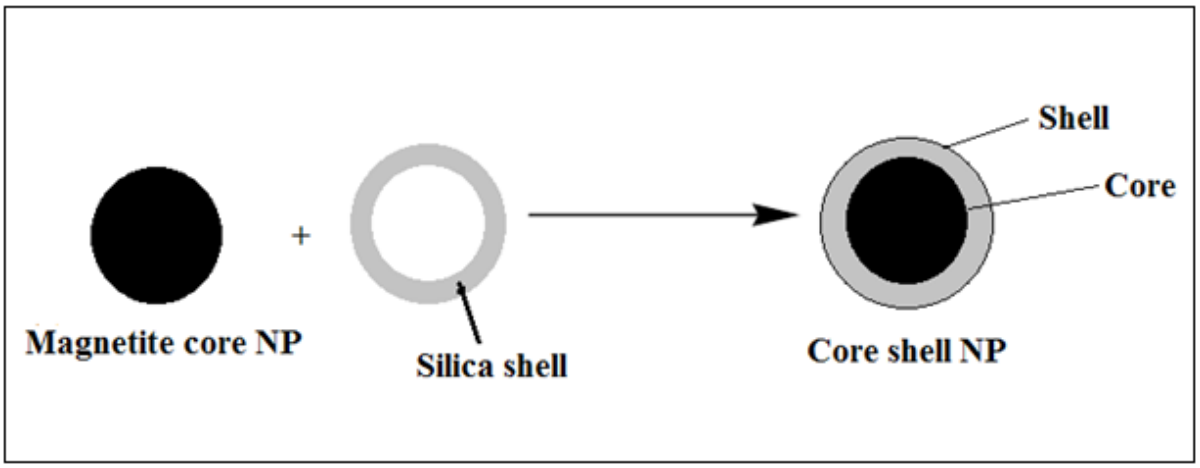

Figure 2. 8 Formation of Core shell NPs

In this study, preparation of magnetic nanoparticles was followed by silica coating around the magnetic nanoparticles by hydrolysis and condensation of tetraethyl orthosilicate (TEOS).

2.6.2 Surfactants Coated Nanoparticles

Surfactants are amphiphilic molecules composed of a hydrophilic or polar moiety known as *head* and a hydrophobic or nonpolar moiety known as *tail*. The surfactant molecules form aggregates known as micelles in water. The hydrophillic ends of a micelle point into the interior of water while the hydrophobic end remains on the surface (Figure 2.9).

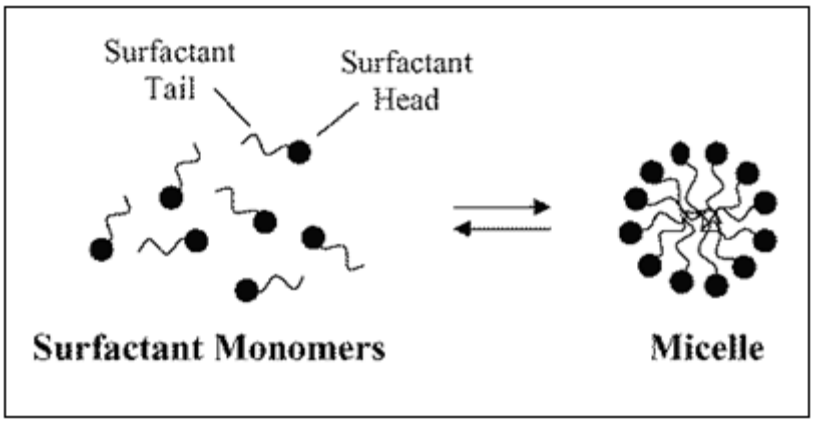

Figure 2. 9 Illustration of surfactant action

The hydrophobic effect and repulsive force are the main forces associated with surfactants (Oh and Park, 2011). Adsorption onto surfactant surfaces or interfaces significantly improves their surface or interfacial free energy. Surfactants such as oleic acid ($CH_3(CH_2)_7CH=CH(CH_2)_7CO_2H$) forms a bulk protective monolayer and highly uniform particles during synthesis of ferrite nanoparticle. Water-soluble Fe_3O_4 nanoparticles surrounded by polyethylene glycol (PEG) have also been synthesized in aqueous medium (Mukhopadhyay *et al.*, 2011).

2.7 Formation of Nanocomposites

The performance of membrane systems is largely decided by the membrane material (Gan *et al.*, 2006). Improved mechanical and thermal stability of the membrane can be realized through incorporation of functional nanomaterials into their structures. Formation of non-covalent interactions by the CNTs with many molecules has opened more research in the utility of such orientations in complexes. In particular, nano-sized inorganic material-blended composite membranes are attractive because of their enhanced properties, such as high selectivity, higher hydrophilicity, and enhanced fouling resistance(Karşı, 2014).

Dispersion of CNTs in a polymer solution could be very difficult to achieve due to the strong van der Waals interactions between them (Han and Fina, 2011). However, the homogenous dispersion can be realized by various CNTs functionalization schemes. Covalent functionalization of CNTs by strong acids inevitably generates defects on the walls of CNTs which degrades its electrical properties (Banerjee *et al.*, 2005). Non-covalent functionalization of CNTs using polysulfone polymer overcomes these limitations. Polysulfone molecules are planar conjugates with sp^2 hybridized structures and they can disperse CNTs easily through π-π interactions.

Polysulfones are members of thermoplastic polymers known for their toughness and stability at high temperatures (Mallick, 2007). They contain the sub-unit aryl-SO_2-aryl, the defining feature of which is the sulfone group (Figure. 2.10). Polysulfone allows easy design and preparation of membranes, with reproducible properties and controllable size of pores down to 40 nanometers. However, it has low resistance to some solvents and undergoes weathering; which can be offset by adding other materials into the polymer.

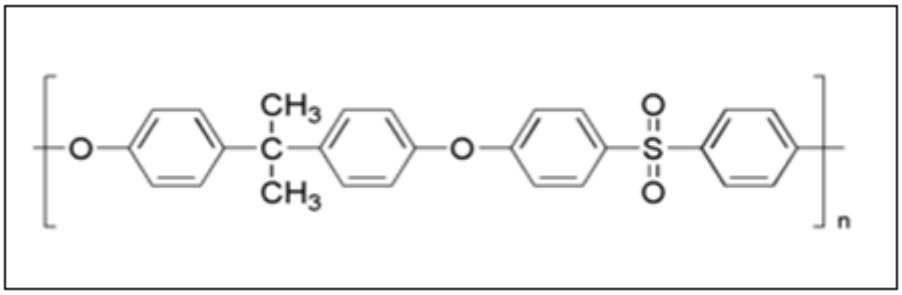

Figure 2. 10 Polysulfone polymer

Incorporation of inorganic nanoparticles into polymeric system can enhance mechanical and thermal stability of polymeric membranes, reducing the negative impact of compaction and heat on membrane permeability. Silver nanoparticles have been doped or grafted on surface of polymeric membranes to inhibit bacterial attachment and biofilm formation (Hajipour *et al.*, 2012). Addition of oxidized MWNT at low weight percentage (up to 1.5 wt. %) also increases the hydrophilicity and permeability of polysulfone membranes (Tang *et al.*, 2009). The strong adsorption and magnetic separation are the advantages of such CNTs-magnetite nanocomposites.

2.8 Analytical Techniques

2.8.1 Scanning Electron Microscopy (SEM)

A scanning electron microscope (SEM) is a type of electron microscope that produces images of a sample by scanning over it with a high energy focused beam of electrons (Goldstein *et al.*, 2012). The electrons interact with electrons in the sample, producing secondary electrons, back-scattered electrons, and characteristic X-rays that can be detected and that contain information about the sample's surface topography and composition (Figure 2.11). The electron beam is generally scanned in a raster scan pattern, and the beam's position is combined with the detected signal to produce an image. The electron beam can be focused to a spot approximately 1 nanometer in diameter, and microscopes are able to resolve details ranging from 1–20 nm in size. To avoid accumulating charge on the surface, samples must be electrically conductive; but nonconducting samples are often coated with an ultrathin coating of metal.

The types of signals produced by a SEM include secondary electrons, back-scattered electrons (BSE), characteristic X-rays, light (cathodoluminescence), specimen current and transmitted electrons. The signals result from interactions of the electron beam with atoms at or near the surface of the sample. In the most common or standard detection mode of secondary electron imaging (SEI), the SEM can produce very high-resolution images of a sample surface, revealing details less than 1 nm in size (Figure 2.11).

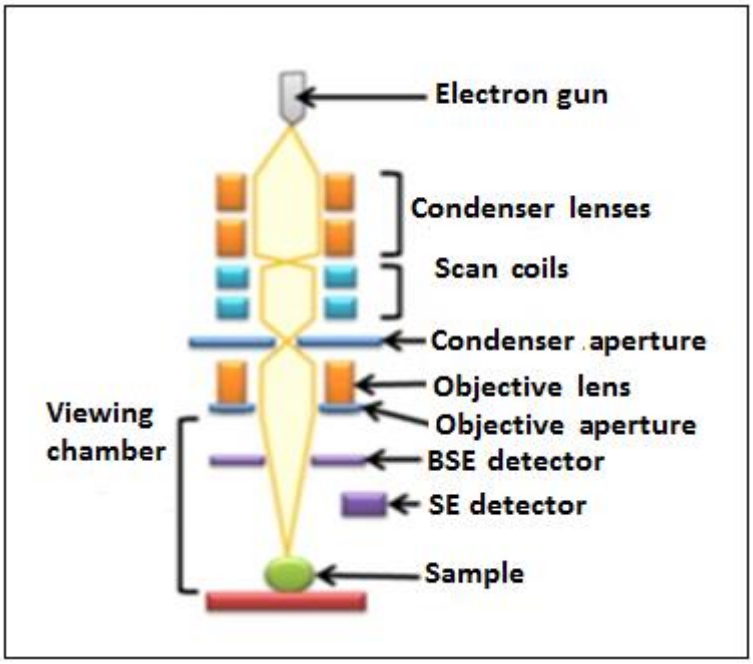

Figure 2. 11 Schematic Diagram of a SEM

Due to the very narrow electron beam, SEM micrographs have a large depth of field yielding a characteristic three-dimensional appearance useful for understanding the surface structure of a sample.

A wide range of magnifications is possible, from about 10 times to more than 500,000 times. Back-scattered electrons (BSE) are beam electrons that are reflected from the sample by elastic scattering. BSE are often used in analytical SEM along with the spectra made from the characteristic X-rays, because the intensity of the BSE signal is strongly related to the atomic number (Z) of the specimen. BSE images can provide information about the distribution of different elements in the sample. For the same reason, BSE imaging can image colloidal gold immuno-labels of 5 or 10 nm diameter, which would otherwise be difficult or impossible to detect in secondary electron images in biological specimens. Characteristic X-rays are emitted when the electron beam removes an inner shell electron from the sample, causing a higher-energy electron to fill the shell and release energy. These characteristic X -rays are used to

identify the composition and measure the abundance of elements in the sample (Grigorian *et al.*, 2008).

The electron beam-specimen interaction equally generates x-ray photons. These characteristic x-rays are caused by the ionization of inner shell electrons when the electron beam energy exceeds critical ionization energy. The relaxation of outer shell electrons into vacancy generated by ejected inner shell electron (usually K shell) yields characteristic x-rays, specific to each element. Energy-dispersive x-ray spectroscopy measures the x-ray intensity as a function of energy whereas wavelength dispersive x-ray spectroscopy measures x-ray intensity as a function of wavelength dispersion based on Bragg‟s diffraction.

2.8.2 Transmission Electron Microscopy

In a TEM analysis, an electron beam interacts with the sample to form a photographic image (Goldstein *et al.*, 2012). TEM transmits the beam of electrons through a thin sample onto a screen or a camera/detector. It has a large number of lenses. The condenser lenses (2 - 4 depending on the microscope) are responsible for the amount of illumination that reaches the sample and control beam intensity or brightness. The objective lens focuses the beam of electrons onto the sample and applies a small amount of magnification. The intermediate and projector lenses magnify the beam and project it onto the camera (CCD or film) or screen to form an image.

It takes only a few seconds to obtain a micrograph (microscope image). The image is a result of the projected beam intensity: Transmitted electrons are detected as light areas in the micrograph; darker areas occur where electrons have been scattered or absorbed by the sample, thus reducing the number of electrons reaching the camera or screen. Figure 2.12 shows schematic diagram of a TEM.

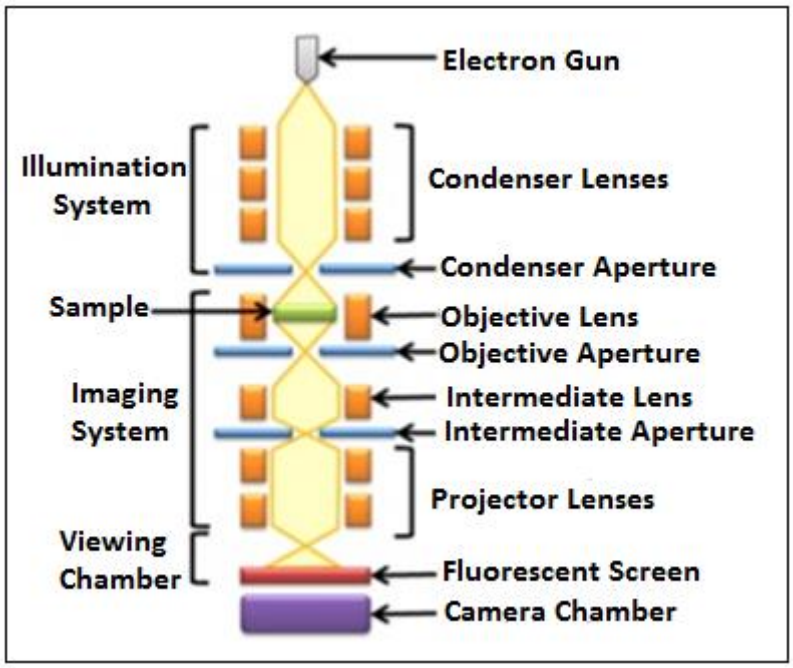

Figure 2. 12 Schematic illustration of a TEM (Ding *et al.*, 2011)

The primary electron beam can also be deflected with no loss in energy resulting in elastically scattered electrons. Elastically scattered electrons are transmitted obliquely relative to the primary beam through a sample and can be used in the generation of electron diffraction patterns (diffraction contrast) since they adhere to Bragg's law of diffraction. The interaction of the primary electron beam with matter similarly results in inelastically scattered electrons which are transmitted obliquely through the sample with loss in energy. Electron energy loss value is element specific and unique to bonding or coordination environment hence important in elemental analysis.

Transmission and absorption of primary electrons by the sample occur as thicker and bright regions for heavy and light elements respectively in the bright field image mode. The image takes a two-dimensional projection on a phosphor screen whereby

the crystal structure can similarly be mapped using high resolution transmission electron microscopy (HRTEM).

2.8.3 Crystallography

X-ray powder diffraction (XRD) is a rapid analytical technique primarily used for phase identification of a crystalline material and can provide information on unit cell dimensions (Suryanarayana and Norton, 2013). The analyzed material is finely ground, homogenized, and average bulk composition is determined. X-ray diffraction is now a common technique for the study of crystal structures and atomic spacing.

X-ray diffraction is based on constructive interference of monochromatic X-rays and a crystalline sample (Suryanarayana and Norton, 2013). X-rays are generated in a cathode ray tube by heating a filament to produce electrons, accelerating the electrons toward a target by applying a voltage, and bombarding the target material with electrons. When electrons have sufficient energy to dislodge inner shell electrons of the target material, characteristic X-ray spectra are produced. These spectra consist of several components, the most common being K_α and K_β. K_α consists, in part, of $K_{\alpha1}$ and $K_{\alpha2}$. $K_{\alpha1}$ has a slightly shorter wavelength and twice the intensity as $K_{\alpha2}$. The specific wavelengths are characteristic of the target material (Cu, Fe, Mo, Cr). Filtering, by foils or crystal monochrometers, is required to produce monochromatic X-rays needed for diffraction. $K_{\alpha1}$and $K_{\alpha2}$ are sufficiently close in wavelength such that a weighted average of the two is used. Copper is the most common target material for single-crystal diffraction, with CuK_α radiation = 1.5418Å. The interaction of the incident rays with the sample produces constructive interference (and a diffracted ray) when conditions satisfy Bragg's Law (Equation 2.17);

$$n\lambda = 2d \sin \theta \quad \text{..... } \mathbf{2.17}$$

where *d* is the inter-lattice spacing and *θ* is the incident angle (Figure 2.13).

This law relates the wavelength of electromagnetic radiation to the diffraction angle and the lattice spacing in a crystalline sample. By scanning the sample through a range of 2θ angles, all possible diffraction directions of the lattice should be attained (Figure 2.13).

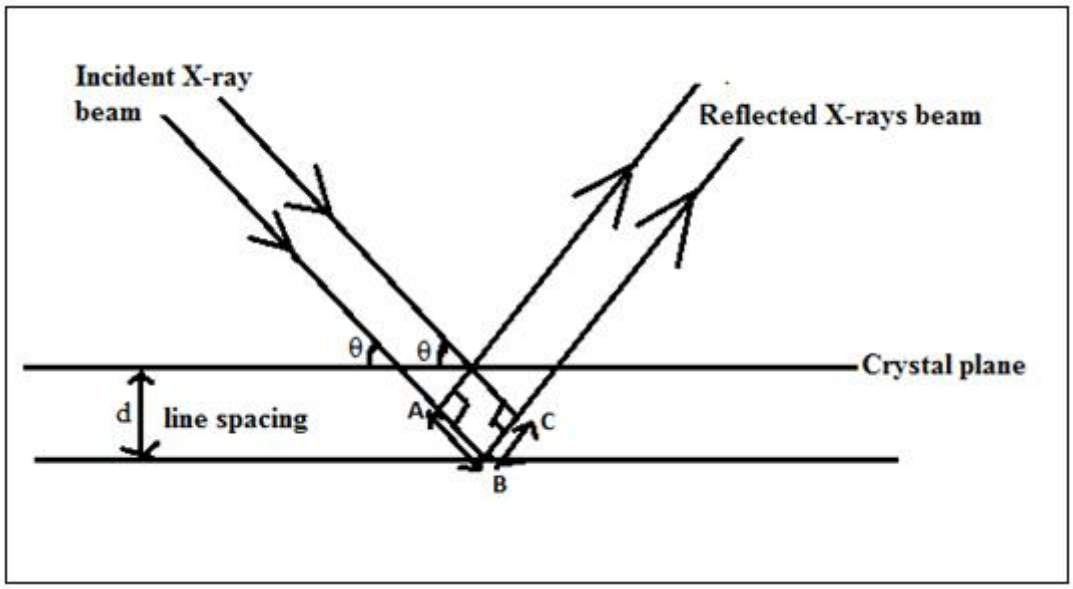

Figure 2. 13 Diffraction of X-ray

Conversion of the diffraction peaks to d-spacings allows identification of the mineral by comparison of d-spacings with standard reference patterns because each mineral has a set of unique d-spacings. The identification of a given crystal structure is usually done by correlating the diffraction pattern obtained with known standard diffraction files i.e. Joint Committee on Powder Diffraction Standards (JCPDS). The Scherrer equation (Equation 2.18) is important in the estimation of crystallite thickness (Chipera and Bish, 2002);

$$t = \frac{0.9\lambda}{(B\cos\Theta)} \quad \text{..... } \mathbf{2.18}$$

where t, λ, θ and B are the crystallite thickness, wavelength of the x-rays, Bragg angle and Full-Width at Half-Maximum respectively of the peak (radians).

2.8.4 Infrared Spectroscopy

Fourier transform infrared spectroscopy (FTIR) analysis is an analytical testing technique used to identify organic and some inorganic materials through the application of infrared radiation (Kumar *et al.*, 2015). This technique measures the absorption of infrared radiation by the sample material versus wavelength. When a material is irradiated with infrared radiation, absorbed IR radiation usually excites molecules into a higher vibrational state. The wavelength of light absorbed by a particular molecule is a function of the energy difference between the at-rest and excited vibrational states. The wavelengths that are absorbed by the sample are characteristic of its composition and structure. The patterns of absorption bands at the various wavelengths throughout the infrared region (or the FTIR spectrum) are unique to each material. Once the spectrum is produced, computer searches of reference libraries assist in the material's identification. A schematic diagram of an FT-IR is shown in figure 2.14.

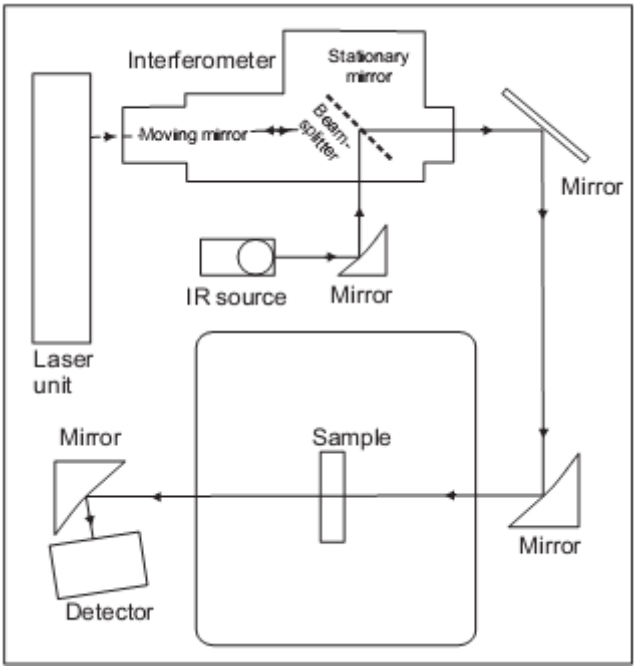

Figure 2. 14 Schematic diagram of an FT-IR Spectrometer (Griffiths and Haseth, 2007)

The FTIR spectra are usually presented as plots of intensity versus wavenumber (in cm^{-1}). Wavenumber is the reciprocal of the wavelength. The intensity can be plotted as the percentage of light transmittance or absorbance at each wavenumber. A molecular vibration occurs when atoms in a molecule are in periodic motion while the molecule as a whole has constant translational and rotational motion (Wilson *et al.*, 2012). This vibration is excited when the molecule absorbs a quantum of energy, E, corresponding to the vibration's frequency, ν, according to the relation $E = h\nu$ (where h is Planck's constant). A fundamental vibration is excited when one such quantum of energy is absorbed by the molecule in its ground state. When two quanta are absorbed the first overtone is excited, and so on to higher overtones. The vibrational states of a molecule can be probed in a variety of ways. The most direct way is through infrared spectroscopy, as vibrational transitions typically require an amount of energy that corresponds to the infrared region of the spectrum.

2.8.5 Ultra-Violet/Visible Spectroscopy

This technique involves the excitation of π-electrons or non-bonding electrons in molecules by ultraviolet or visible light energy to higher anti-bonding molecular orbitals (Mark, 2001). The longer the wavelength of light electrons can absorb, the more easily the electrons are excited. When light is absorbed by a material, valence (outer) electrons are promoted from their normal (ground) states to higher energy (excited) states. Electromagnetic radiation is passed through the sample which is held in a small square-section cell of usually 1 cm wide internally (Figure 2.15). Radiation across the whole of the ultraviolet/visible range is scanned over a period of approximately 30 seconds, and radiation of the same frequency and intensity is simultaneously passed through a reference cell containing only the solvent. Photocells then detect the radiation transmitted and the spectrometer records the absorption by comparing the difference between the intensity of the radiation passing through the sample and the reference cells (Figure 2.15).

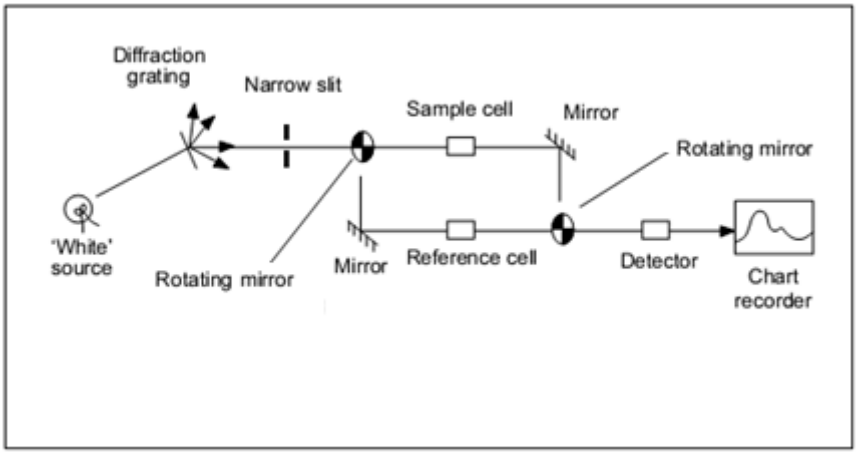

Figure 2. 15 Schematic diagram of UV-Visible spectrometer

The spectrum is produced by comparing the currents generated by the sample and the reference beams. The wavelength at which maximum absorption occurs is given the

symbol λ_{max} which is frequently sufficient to identify a substance, although identification is not the most common use of this technique.

The energies of the orbitals involved in electronic transitions are fixed, with sharp absorption peaks in ultraviolet/visible spectroscopy. However, broad absorption peaks are seen because a number of vibrational energy levels are available at each electronic energy level, and transitions can occur to and from the different vibrational levels which results in peak broadening. Comparison of the spectra of different compounds and relative strength of light absorbing molecules (chromophores) is made using a corrected absorption value.

2.8.6 Atomic Absorption Spectroscopy

The concentration of elements in a sample is quantitatively determined by an atomic absorption spectroscopy (Ghaedi *et al.*, 2008). This technique is based on the principle of light absorption by elements in gaseous state at very specific wavelengths (Figure 2.16). The sample can be in many forms such as aqueous, organic solution and even solid provided it is soluble. The solution of the analyte is drawn into the AAS flame in order to be ionized into gaseous phase. Standards of the element are run to obtain the calibration curve which is used to determine the concentration of the sample analyte.

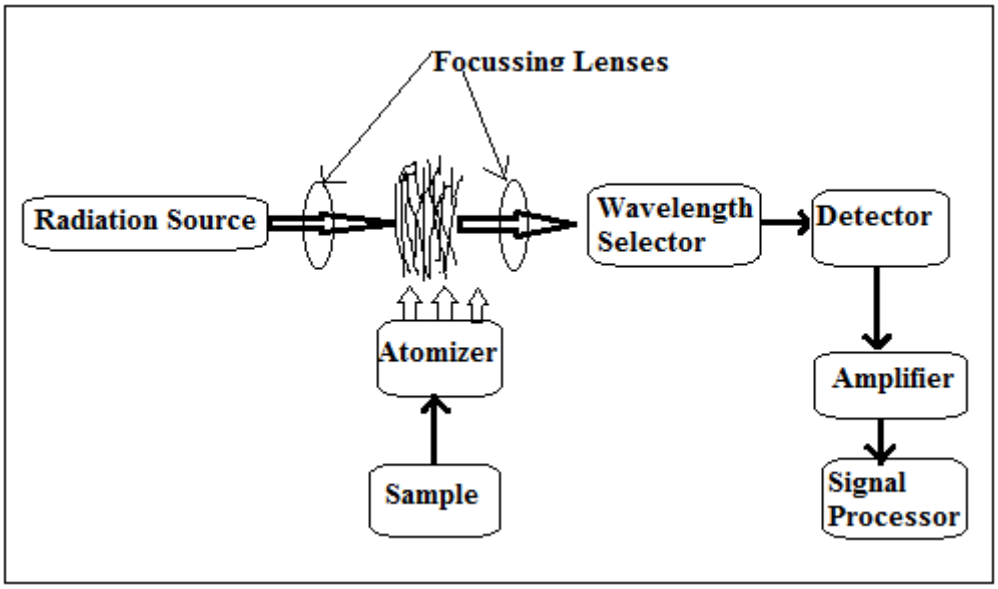

Figure 2. 16 Flow diagram for AAS analysis

Absorption of a defined quantity of energy (radiation of a given wavelength) enables the promotion of the electrons in the atomizer to higher orbitals (excited state). A particular electron transition in a particular element is related to a certain wavelength. The width of an absorption line for each wavelength of an element is in the order of a few picometers (pm) while each wavelength corresponds to only one element. The detector measures radiation flux for a sample in units of absorbance which is related to analyte concentration or mass from the Beer-Lambert Law (Equation 2.19);

$$A = \varepsilon lc \quad \textbf{2.19}$$

where A-absorbance; Ɛ-molar absorptivity, l = length of tube (1cm); c = concentration of solution in moldm^{-3}. The Beer–Lambert's law relates the light attenuation to the properties of the material through which light is travelling.

2.8.7 Superconducting Quantum Interference Device (SQUID)

The quantum design SQUID uses a magnetic property measurement system (MPMS) to monitor very small changes in magnetic flux and determine magnetic properties of a sample (Kleiner *et al.*, 2004). In particular, it is the only method which allows directly determination of overall magnetic moment of a sample in absolute units. The superconducting quantum interference device (SQUID) consists of two superconductors separated by thin insulating layers to form two parallel Josephson junctions**.**

When the sample is moved up and down it produces an alternating magnetic flux in the pick-up coil .The magnetic signal of the sample is obtained via a superconducting pick-up coil with four windings. This coil is, together with a SQUID antenna, part of a whole superconducting circuit transferring the magnetic flux from the sample to an rf SQUID device which is located away from the sample in the liquid helium bath. This device acts as a magnetic flux-to-voltage converter. This voltage is then amplified and read out by the magnetometer's electronics (Figure 2.17).

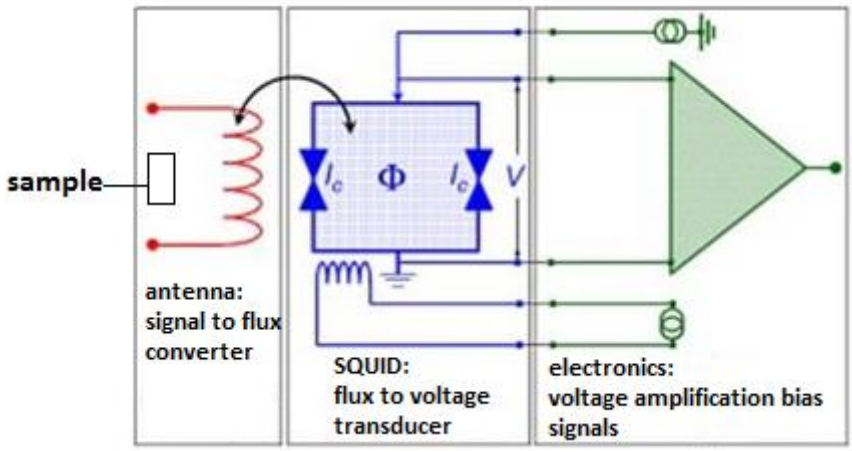

Figure 2. 17 Flow chart for SQUID

The instrument has maximum sensitivity in the range of 10^{-9} emu with data being collected between H = O to ±50 kOe and T = 1.7 K - 400 K. It involves samples of sizes 20 to 40 mg or even less if the material is strongly magnetic (Nagl and Wolfbeis, 2008).

As magnetic flux is increased, the screening current also increases, but when the magnetic flux reaches half a quantum, the junctions become momentarily resistive. The screening current changes sign when the applied flux reaches half of a flux quantum. At exactly one flux quantum, the screening current goes to zero.

A plot of magnetic induction (B) as a function of the magnetic field strength (H) forms a hysteresis loop (Figure 2.18). The first quadrant shows the changes in behaviour as the magnetization of the material proceeds. The magnetic moments are oriented parallel to this field as an external magnetic field of strength H is applied. The magnetization is said to be saturated when all magnetic moments are oriented. The second quadrant shows the demagnetization curve of the hysteresis loop. The most important magnetic properties of a material such as remanence (Br) and coercivity (Hc) are represented by the shape of the demagnetization curve. The behavior of the magnetization curves in the first two quadrants resembles those in the third and fourth quadrant though in the opposite direction.

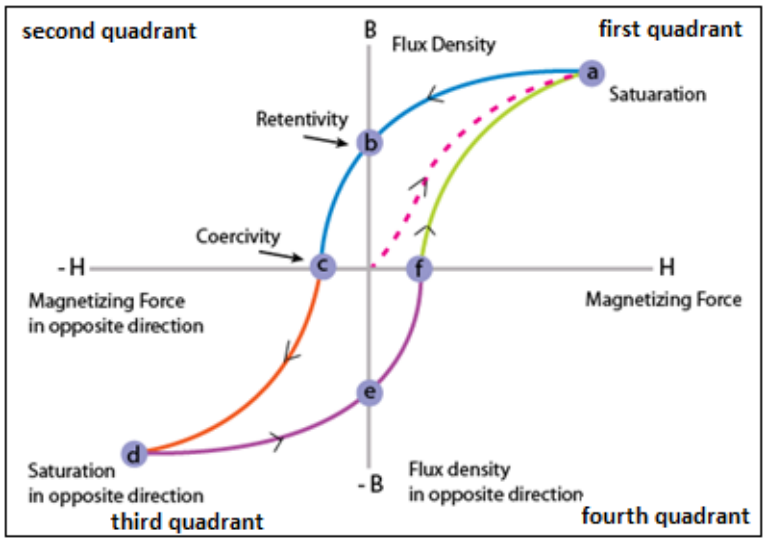

Figure 2. 18 Hysteresis loop for a magnetic material (Carrey *et al.*, 2011)

Materials can be classified as diamagnetic, paramagnetic, ferromagnetic or ferromagnetic based on their behavior in magnetic field (Akbarzadeh *et al.*, 2012). Diamagnetic materials have fully filled orbital shells with no unpaired electrons. Application of an applied magnetic field to such electronic orientations results in no net magnetic moments. On the other hand, paramagnetic materials have their orbitals partially filled with electrons leading to an unpaired electronic system. When magnetic field is applied to such electronic system, the unpaired electrons align themselves in the direction of the applied field producing a net magnetic moment.

Ferrimagnetic and antiferromagnetic materials have incompletely filled 3d subshell whose electrons produce spin magnetic moments through spin alignment. Reversal of electron spins in adjacent cations due to anti-parallel spin alignments characterizes the ferrimagnetic materials. In ferrimagnetic and antiferromagnetic materials, remanence (M_R) does not fall in the origin since such materials retain some magnetization after applied magnetic field is removed. Since ferromagnetic material can reach saturation at laboratory applied fields, they have hysteresis loops that are sigmoidal and flat-

topped. Superparamagnetism is a type magnetism found in small nanoparticles of ferrimagnetic or ferromagnetic materials. Materials are said to be in superparamagnetic state when their magnetization appears to be zero upon removal of an external magnetic field. In this state, the nanoparticles can be magnetized by an external magnetic field.

The development of water treatment technologies have been driven by discovery of new rarer contaminants, the promulgation of new water quality standards, and cost (Najm and Trussell, 1999). A number of methods such as coagulation, filtration with coagulation, precipitation, ozonation, adsorption, ion exchange, reverse osmosis and advanced oxidation processes have been used for the removal of water pollutants from polluted water and wastewater (Gupta *et al.*, 2012). However, these methods have been found to be limited as they often involve high capital and operational costs. Among the possible techniques for water treatments, the adsorption process by solid adsorbents shows potential as one of the most efficient methods for removal of water contaminants in wastewater treatment.

In recent years, the search for low-cost adsorbents with pollutant-binding capacities has intensified. Natural adsorbents made from agricultural wastes and industrial wastes have been utilized due to their low-cost adsorbents. However, the adsorption capacities of such low-cost adsorbents are much lower and such adsorbents have much smaller surface areas (Babel and Kurniawan, 2003). Engineered adsorbents exhibit highest adsorption capacities and surface areas since they are produced under strict quality control.

Functionalized CNTs are able to adsorb a multiplicity of water pollutants mainly by weak intermolecular interactions (van der Waals forces) and ion exchange

mechanisms (Goyal *et al.*, 2011). These attraction forces can be superimposed by π-πinteractions in the case of aromatic adsorbates or by electrostatic interactions between surface oxide groups and ionic adsorbates. Polymeric adsorbents can be beneficially applied for recycling of valuable chemicals from process wastewaters.

Polymers such as polysulfone have been suggested as suitable matrices for CNTs (Wang *et al.*, 2007). The addition of iron oxides nanoparticles to polymeric membranes has been shown to increase membrane surface hydrophilicity, water permeability, or fouling resistance. This study has developed a well-designed chemical modification for CNT-IPSF polymeric shells by functionalizing with iron oxides magnetic nanoparticles during fabrication of CNT-IPSF/Fe_3O_4 nanocomposites. The nanocomposites were characterized for specific adsorptive properties and its efficiency in removal of lead (ii) ions and phenanthrenes from contaminated waters was compared to that of activated carbon in the market to ascertain its suitability.

CHAPTER THREE

MATERIALS AND METHODS

3.1 Research Design

This study involved fabrication and characterization of CNT-IPSF/Fe_3O_4 nanocomposites from synthesized carbon nanotubes (CNTs), magnetite NPs and core shell NPs. This is followed by determining efficiency of fabricated CNT-IPSF/Fe_3O_4 nanocomposites in removal of lead and phenanthrene from polluted water samples and the findings compared to that of commercial activated carbon. Experimental methods of sample analysis using specific equipment are discussed.

3.2 Synthesis and Characterization of Nanomaterials

3.2.1 Carbon Nanotubes (CNTs)

The CNTs were synthesized by thermal catalytic chemical vapour deposition (CCVD), using a chemical vapour deposition (CVD) reactor at temperatures of 600–700 °C, a range that supports synthesis of MWCNTs (Yan *et al.*, 2008). Approximately 0.1 g iron powder on ceramic boat was placed in modified glass tube as bed reactor for Lindberg tube furnace (Model TF55035C-1). Iron catalyst was chosen due to high carbon diffusion rate in the metal and wide temperature window (600−1500 °C) of CVD for a range of carbon precursors. Ceramic boats were used as support for both iron catalyst and also CNTs formed because they can withstand high temperatures (Grigorian *et al.*, 2008).

The process involved passing acetylene/argon through flow rate meters at optimal flow rate of 8 cm^3/min and 1 cm^3/min respectively through a tubular reactor (Figure 3.1) for 30 minutes. At this flow rate, argon could carry enough of the acetylene gas

(source of CNTs) into the reactor. Besides this rate, the CNTs source has enough time for decomposition and deposition on the catalyst.

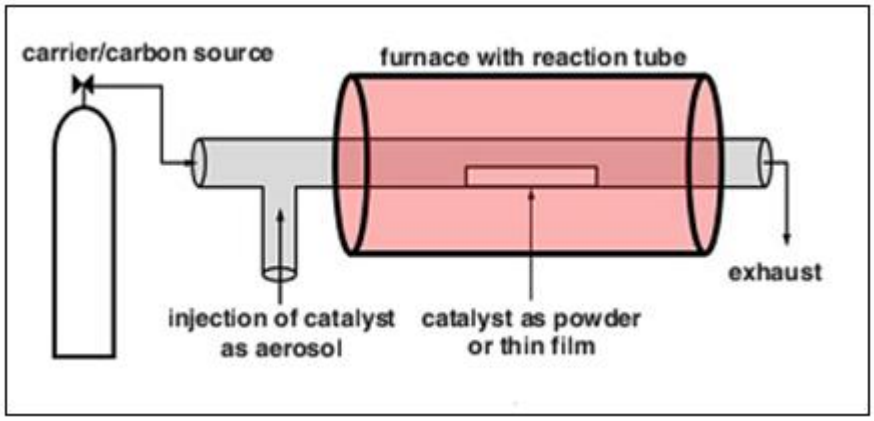

Figure 3. 1 A set-up for chemical vapour deposition process

The CNTs were allowed to grow in the presence of catalyst by bottom-up method and then collected upon cooling the system to room temperature. The CNTs were soaked in concentrated nitric acid at room temperature for 12 hours in order to dissolve iron catalyst particles. They were filtered through 0.45µm ceramic filter and washed with deionized water until neutral pH was achieved. Sonication of CNTs was done for 30 minutes to disperse the CNTs followed by centrifugation (Blanch, 2010).

CNTs were dried at 450 °C for 60 minutes before subsequent experimental use to remove amorphous carbon as well as allow creation of pore-structures during the activation process thus improving the structure. Synthesized CNTs were characterized by SEM, TEM and EDX for their morphology, size and elemental composition respectively.

3.2.2 Magnetite Nanoparticles

Magnetic magnetite particles (MMP) were prepared via solvothermal reaction according to the method previously reported (Wakeman and Williams, 2002). The

material used included approximately 2.7 g $FeCl_3 \cdot 6H_2O$, 80 mL ethylene glycol, 7.2 g sodium acetate and 2 ml polyethylene glycol which were added into an 80 mL capacity modified stainless-steel autoclave, at optimal 200 °C for 8 hours. The MMP were washed with deionized water to neutral pH, and dried at room temperature in a vacuum oven. Black MMPs formed were characterized using UV-Vis, FTIR and SEM techniques.

3.2.3 Functionalization of Magnetite Nanoparticles

Magnetite nanoparticles were coated by silica through sol-gel process (Deng *et al.*, 2008), where about 0.1 g of the MMP were dispersed in presence of ethanol, followed by 25 mL deionized water and 2.0 ml aqueous ammonia. The silica coating was done by adding tetraethyl orthosilicate (TEOS) and mixture was stirred for optimal 12 hours at room temperature. The MMP-SM were then washed with water to neutral pH, and dried on glass plate at 60 °C for 2 hours in a vacuum oven to eliminate its oxidation in air. Analytical techniques such as UV-VIS, FTIR, SEM, XRD and SQUID-MPMS were employed to characterize the silica-coated magnetite nanoparticles based on absorption maxima, functional groups, morphology, particle structure and size, and magnetic property respectively.

3.2.4 Fabrication and Characterization of CNT-IPSF/Fe_3O_4 Nanocomposites

CNT-IPSF polymer solution was prepared by phase inversion method (Gohil and Ray, 2009) with modification through blending synthesized CNTs with polysulfone (PSF) polymer as follows. A bout 0.1 g CNTs were mixed with 10 ml N, N-dimethylformamide (DMF) with constant stirring while 5 g of PSF was also mixed separately with 50 ml DMF with stirring to make its solution at 50 °C. The two solutions were mixed in a shaking water bath at 50 °C to make CNT-PSF solution.

About 0.3 g of $Fe_3O_4.SiO_2$ nanoparticles were added to CNT-PSF polymer solutions and the mixture ultrasonicated for 1 hour. The CNT-IPSF/Fe_3O_4 polymer solutions were immediately cast onto a glass plate with the aid of an aspirator. The solution was stirred with 1 % (w/v) aqueous polyvinyl alcohol (PVA), 1 % maleic acid solution and the nanocomposites were then heated at 60 °C for 30 minutes followed by overnight drying in ambient air. The structure of the nanocomposites was characterized by SEM, and EDX techniques. During the SEM analysis, the nanocomposite was protected from destruction during the imaging process (Nehl *et al.*, 2006).

3.3 Efficiency of CNT-IPSF/Fe_3O_4 Nanocomposites on Removal of Pb(II) ions

3.3.1 Preparation of Standards and Sample Solutions

All chemicals used were of analytical-reagent grade, unless otherwise specified and were purchased from Sigma Aldrich Co. Ltd. The $Pb(NO_3)_2$ stock reagent (331.208 g/mol) was dissolved in distilled water to obtain 1000 mg/L stock solution. Standard solutions at concentrations of 1, 2, 4, 6 and 8 mg/L Pb(II) ions were obtained by diluting portions of the stock solution. The calibration curve for Pb(II) ions was determined by running the standards on flame atomic absorption spectrometry (Unicam Solar 32). To adjust the pH, 0.1 mol/L HNO_3 (69 % A.R) and 0.1 mol/L NaOH (≥ 98 %) solutions were used. The effect of similar heavy metal ions (Zn^{2+}, Cu^{2+}, and Cd^{2+}) and anionic ligands (NO_3^-, NH_3 and EDTA) on adsorption was studied. Desorption studies were done using desorption solutions of 0.1M HNO_3. About ten nanocomposite samples were analyzed in each case with the batch tests done in triplicates. Blanks were also run alongside sample solutions to eliminate errors in metal ions concentration obtained.

The adsorption capacity of adsorbent, qe (mg/g) was calculated using equation 3.1;

$$q_e = [(C_o - C_e) * V]/W \quad \text{..... } \mathbf{3.1}$$

where V - volume of aqueous solution in litres and W - weight of nanocomposites used in grams

3.3.2 Optimization of Adsorption Parameters

3.3.2.1 Determination of pH_{pzc}

Determination of point of zero charge is important since the fabricated nanocomposite may contain some functional groups. It was therefore necessary to investigate the pH at which such groups have no effect on adsorption process. Solid addition method was used to determine the pH_{PZC} (Adelodun *et al.*, 2014). About 1 M of nitric and hydrochloric acid solutions was shaken in six 25 ml flasks with pH of 2-12. This was followed by adding 0.05 g of the nanocomposites to each of the 25 ml solutions on a shaker (120 rpm) for 24 hours. Final pH values of the solutions were determined after 5 minutes of settling. The initial pH values were plotted against the final pH values in order to determine the pH_{PZC} along the horizontal axis.

3.3.2.2 Effect of Adsorbent Dosage on Pb(II) ions Adsorption

About 50 ml aliquot solutions having 2 mg/L and 4 mg/L of the Pb^{2+} ions solutions were placed in two sets of conical flasks. Each of the nanocomposite masses (0.02, 0.04, 0.06, 0.08, 0.1 and 0.12 g) was added to each set of stoppered conical flasks and agitated (120 rpm) for 60 minutes. Upon settling, the mixtures were filtered and the Pb(II) ions concentrations were determined by an air acetylene flame atomic absorption spectrophotometer.

3.3.2.3 Effect of Contact Time on Pb(II) ions Adsorption

The influence of time on the interaction of the adsorbent with the Pb(II) ions was performed at optimum pH. The adsorption studies were carried out by adding 0.05 g of nanocomposites into two sets of 50 ml conical flasks each containing 2 mg/L and 4 mg/L Pb(II) ions solutions before shaking. This was followed by varying contact times for adsorption at 10, 20, 30, 60 90, 120 and 240 minutes of agitation and 15 minutes of centrifugation. The concentrations of the Pb(II) ions in the supernatants were then measured by an air acetylene flame atomic absorption spectrophotometer.

3.3.2.4 Effect of pH on Pb(II) ions Adsorption

Two sets of 50 ml aliquots standards (2 mg/L and 4 mg/L) of Pb(II) solutions were prepared at different pH values (1, 2, 3, 4, 5, 6 and 7). The pH was then adjusted (by addition of 0.1M HCl or NaOH) regularly to avoid formation of hydroxides by target cations through precipitation. About 0.05 g of the nanocomposites was put into each of the flasks (stoppered 100 mL flasks) and agitated using a suitable shaker (120 rpm) for 60 minutes (optimum contact time) at 25 °C. The suspensions were filtered and the concentration of Pb^{2+} ions was determined using air acetylene atomic absorption spectrophotometer.

3.3.3 Kinetics Model for Pb(II) ions Adsorption

The nanocomposites interacted with Pb(II) ions as a function of time at optimum pH 5. The adsorption studies were carried out by adding 0.05 g each of CNT-IPSF/Fe_3O_4 nanocomposites into 50 ml conical flasks containing 2 mg/L Pb(II) ions solutions. The mixtures were shaken for different contact times from 10 to 250 minutes followed by centrifugation for 15 minutes. The Pb(II) ions concentrations in the

supernatants were determined after 10, 20, 30, 60 90, 120, 180 and 250 minutes of agitation by air acetylene flame atomic absorption spectrophotometer.

In the control experiments, 0.05 g of standard adsorbent of activated carbon was placed into plastic bottles with 50 ml of 2 mg/L of Pb(II) solutions at pH 5 and time intervals of 10-250 minutes. The mixtures were treated in similar way and the residual Pb(II) ions determined by AAS. The adsorption data obtained were fitted to adsorption kinetic models.

3.3.4 Isotherms Model for Pb(II) ions Adsorption

The initial concentrations of the Pb(II) ions ranged between 2 and 12 mg/L. A 0.05 g of the CNT-IPSF/Fe_3O_4 nanocomposites was shaken with Pb(II) ions standards at pH 5 for 60 minutes (optimized contact time) at 25 °C on a rotatory shaker to ensure removal equilibrium was reached. The removal of the adsorbent was done after 10 minutes of centrifugation followed by determination of Pb^{2+} ions concentrations by AAS.

For control experiments, 0.05 g of standard adsorbent of activated carbon was put into plastic bottles with 50 ml of 2, 4, 6, 8, 10 and 12 mg/L of Pb(II) solutions at 25 °C and pH 5, and mixture shaken for 60 minutes of contact time. The mixtures were treated in similar way and residual Pb(II) determined by AAS. The adsorption data obtained were fitted to adsorption isotherms models.

3.3.5 Effect of Counter ions on Pb(II) ions Adsorption

3.3.5.1 Effect of Cations

A 0.05 g of CNT-IPSF/Fe_3O_4 nanocomposites were agitated with 2 mg/L Pb(II) ions initially without other cations and the Pb(II) ions concentrations adsorbed were

determined. A further experiment involved agitating 0.05 g of the nanocomposites with 50 ml batch solution containing optimal 2 mg/L of similar divalent cations (Pb(II), Zn(II), Cu(II), and Cd(II) ions). The uptake of these metal ions by the nanocomposites was then determined.

Control experiment involved agitating 0.05 g of CNT-IPSF/Fe_3O_4 and activated carbon adsorbents separately with optimal 2 mg/L containing Pb(II), Zn(II), Cu(II) and Cd(II) ions. The removal efficiency (%) of the adsorbents for the cations was determined.

3.3.5.2 Effect of Anions/Ligands

The effect of anions and ligands were studied by agitating 0.05 g nanocomposites with 2 mg/L Pb(II) ions solutions initially without NO_3^-, NH_3 and EDTA and later spiked with concentrations 2.0 and 4.0 mg/L of NO_3^-, NH_3 and EDTA. Blank samples without similar anion/ligands were used. The Pb(II) ions in each case were determined.

Control experiments involved putting 0.05 g CNT-IPSF/Fe_3O_4 nanocomposites and activated carbon adsorbents into plastic bottles with each 2 mg/L of Pb(II) ions solution spiked with 2 mg/L of NO_3^-, NH_3, EDTA. The removal efficiency (%) of the Pb(II) ions by adsorbents was determined. The pH was controlled by adding 0.1M HCl or NaOH solutions

3.4 Efficiency of CNT-IPSF/Fe_3O_4 Nanocomposites on Removal of Phenanthrenes

3.4.1 Preparation of Standards and Sample Solutions

All chemicals used methanol (99.8 %) and phenanthrenes (99 %) were of analytical grade purchased from Aldrich Sigma Co. Ltd. Working solutions from phenanthrenes (1000 µg/L) were prepared by further dilutions in methanol. A set of standards of phenanthrene solutions at the concentration of 5-100 µg l^{-1} was made in methanol and were stored at room temperature (26 ± 2 °C). Phenanthrene concentrations were obtained using UV–visible Spectrocopy (Specord R-200 Plus) from absorbance of phenanthrenes at 293 nm as per literature (Mateen *et al.*, 2015). Percentage (%) phenanthrenes removal by the nanocomposites was then calculated.

3.4.2 Optimization of Adsorption Parameters

3.4.2.1 Effect of Adsorbent Dose on Phenanthrenes Adsorption

Approximately 20 ml aliquot solutions having initial concentration of 15 and 20 µg/L of the phenanthrene solutions was placed in conical flasks. Each of the masses (2, 4, 6, 8, 10, and 20 mg) of the nanocomposites was added to each set of the conical flasks and agitated (120 rpm) for 60 minutes. The mixtures were filtered followed by determination of phenanthrene concentrations by UV–Visible Spectrophotometer.

3.4.2.2 Effect of Contact Time on Phenanthrenes Adsorption

The adsorption studies were carried out by adding 6 mg of nanocomposites into conical flasks each containing 20 ml of 15 and 20 µg/L phenanthrene solutions. Each set of the mixtures were agitated and aliquots of the filtrates from the conical flasks drawn after 5, 10, 20, 30, 40 and 60 minutes of agitation time. Amounts of phenanthrenes in the aliquots were quantified with UV–Vis Spectrophotometer.

3.4.2.3 Effect of pH on Phenanthrenes Adsorption

Approximately 20 ml aliquots of 15 and 20 µg/L phenanthrene solutions in conical flasks were prepared at different pH values 1, 4, 7, 8 and 12. Nitric acid and sodium hydroxide solutions (0.1 M) were used to set the pH of the solutions before adsorption commenced. About 6 mg of the nanocomposites was added to each flask and agitated in a shaker (120 rpm) for 60 minutes at 25 °C. The suspensions were filtered and the concentration of phenanthrene was determined using UV–Vis Spectrophotometer.

3.4.3 Kinetics Model for Phenanthrenes Adsorption

The adsorption kinetics was carried out in continuously stirred conical flasks each containing 6 mg of nanocomposites in 20 ml of 20 µg/L phenanthrenes solutions at 25 °C. Ten experiments involved the use of two 20 ml portions of 20 µg/L of phenanthrenes solutions in which one portion was treated with 6 mg of nanocomposites while the other portion was treated with 6 mg activated carbon standard adsorbent (control) at different adsorptions times of 5, 10, 20, 30, 40 and 60 minutes and analyzed for residual phenanthrenes concentration by UV-Vis spectrometry. The adsorption data obtained were fitted to adsorption kinetic models.

3.4.4 Isotherms Model for Phenanthrenes Adsorption

Approximately 6 mg of the CNT-IPSF/Fe_3O_4 nanocomposites was shaken with 20 ml of phenanthrenes standards at pH 5 for 60 minutes (optimized contact time) at 25 °C on a rotatory shaker in order to attain equilibrium. The mixtures were centrifuged for 10 minutes to allow distinct separations to occur. The phenanthrenes concentrations were determined by UV-Vis spectrophotometer.

In the control experiments, 6 mg of standard adsorbent of activated carbon was put into plastic bottles with 20 ml of 1, 2, 4, 6, 8 and 10 µg/L of phenanthrenes solutions

at 25 °C and pH 5, and mixture shaken for 60 minutes of contact time. The mixtures were treated in similar way and residual phenanthrenes determined by UV-Vis spectrophotometer. The adsorption data obtained were fitted to adsorption isotherms models.

3.4.5 Effect of PAHs on Phenanthrenes Adsorption

Effect of PAHs was studied by agitating 6 mg CNT-IPSF/Fe_3O_4 nanocomposites in 20 ml portions of 20 µg/L phenanthrenes solutions initially without the selected PAHs (naphthalene and anthracene) and later each spiked with 20 µg/L PAHs concentrations. Blank samples without the selected PAHs were used.

Control experiments involved agitating 6 mg of CNT-IPSF/Fe_3O_4 nanocomposites and standard activated carbon adsorbents in ten conical flasks with each 20 ml batch solutions containing 20 µg/L mixtures of phenanthrenes, naphthalene and anthracene solutions. The removal efficiency (%) of the adsorbents for the PAHs was determined. Removal efficiency of the fabricated nanocomposites was compared to other Fe_3O_4 based adsorbents to determine its suitability in applications.

3.5 Application of CNT-IPSF/Fe_3O_4 Nanocomposites in Wastewater Treatment

3.5.1 Wastewater Sampling

Water samples of about one litre capacity containing industrial effluents were collected from Nairobi river using a standard sampling technique (Patnaik, 2010). Care was taken to avoid contamination of the sample during sampling, handling and transport to the laboratory by using polyethylene bags for lead ions and glass containers for phenanthrenes as leaching and adsorption are minimal. Sample preparation protocol was followed. The samples were immediately cooled (on ice) before further analysis.

3.5.2 Removal of Pb(II) ions and Phenanthrenes from Wastewater

Water samples were filtered and portions of it analyzed to obtain initial concentrations of Pb(II) ions and phenanthrenes using AAS and UV-Vis spectrophotometer respectively. The rest of water samples were stored at 4 °C in a refrigerator for further analysis. 50 mL each of the wastewater samples whose pH had been adjusted to 5 was gently agitated with 0.05 g of nanocomposites on a rotatory shaker (120 rpm) for 1 hour at 25 °C. The mixtures were filtered through No. 1 paper filter and the nanocomposites washed three times using 0.1M HNO_3 and methanol for the two techniques respectively before determining the final concentrations. Control experiments used 0.05 g commercial activated carbon on 50 ml wastewater samples and agitated at fixed temperature 25 °C for one hour and at 120 rpm. The standard adsorbent was washed three times before determining residual Pb(II) ions and phenanthrenes in the resultant filtrates. Comparison of their percentage (%) removal efficiencies was done to establish if the nanocomposites prepared was more efficient than the standard adsorbent employed.

3.6 Desorption Studies on CNT-IPSF/Fe_3O_4 Nanocomposites

3.6.1 Desorption Studies Using Pb(II) ions

The strength of the adsorption process was determined by desorption studies while reusability of the nanocomposites was investigated against regeneration experiments. Each of the 0.05 g nanocomposites was continuously stirred with 50 ml of 2 mg/L Pb(II) solutions in plastic bottles to allow adsorption to take place. After filtration, each nanocomposite with Pb(II) ions load was transferred to each conical flask containing 50 ml desorption solvents of H_2O, 0.1 M HNO_3, and 0.1 M EDTA. The

mixtures were shaken at 120 rpm for 18 hours followed by determination of the concentration of Pb(II) ions after desorption.

The experiment was repeated using 0.05 g of commercial activated carbon adsorbent into each of the plastic bottles (pools) containing 2 mg/L Pb(II) ions solution and treated in the same manner as for the nanocomposites and the Pb(II) ions in filtrates was determined.

3.6.2 Desorption Studies Using Phenanthrene

Each of the 6 mg nanocomposites was continuously stirred with 20 ml of 20 µg/L phenanthrene solutions in conical flasks to allow adsorption to take place. Upon filtration, each adsorbent with phenanthrenes load was transferred to each conical flask containing 20 ml desorption solvents of methanol, n-hexane and acetone. The mixtures were shaken at 120 rpm for 18 hours followed by determination of the concentration of phenanthrenes after desorption.

Control experiments involved putting 6 mg of commercial activated carbon adsorbent into each of the conical flasks (pools) containing 20 µg/L phenanthrene solutions, agitating at 120 rpm for 18 hours. The phenanthrene in filtrates after washing spent adsorbent with methanol, n-hexane and acetone was determined by UV-Vis spectrometer.

3.7 Regeneration Studies on CNT-IPSF/Fe_3O_4 Nanocomposites

3.7.1 Regeneration of CNT-IPSF/Fe_3O_4 Nanocomposites Using Pb(II) ions

Adsorption experiments were carried out on the CNT-IPSF/Fe_3O_4 nanocomposites by agitating 0.05 g of prepared nanocomposites with Pb^{2+} ions at varying initial concentrations (1, 2. 4, 6, 8 and 10 mg/L). After adsorption process, the

concentrations of Pb(II) ions adsorbed onto the nanocomposites and residual Pb(II) ions in filtrates were determined to find out if there was any significant adsorption by the nanocomposites. Desorption studies were performed by shaking the resultant Pb-loaded adsorbent with 20 mL of 0.10 M HNO_3 in water shaker bath for 1 hour, the Pb(II) ions were separated magnetically and the nanocomposite was dried. The dried nanocomposites were added to fresh Pb(II) ions solutions followed by agitating the mixture mechanical shaker, and the spent adsorbent was separated from the solution. The Pb-loaded adsorbent was mixed with 20 mL of 0.10 M HNO_3, shaken and separated from the mixture. This desorption adsorption process at each concentration was repeated three times to investigate reusability of nanocomposites from % desorption efficiencies after third cycle.

3.7.2 Regeneration of CNT-IPSF/Fe_3O_4 Nanocomposites Using Phenanthrene

To investigate the reusability of the adsorbent, desorption and adsorption studies on the CNT-IPSF/Fe_3O_4 nanocomposites were carried out. After adsorption process desorption studies were performed by mixing resultant phenanthrene-loaded adsorbent with 20 mL of acetone in water shaker bath for 1 hour, filtered and the phenanthrenes desorbed was determined. The spent adsorbent was dried and agitated with fresh 20 ml of 20 µg/L phenanthrenes solution to allow adsorption to take place. The spent nanocomposite was shaken in fresh 20 ml acetone (1hour) and separated from the solution followed by drying and determination of phenanthrenes desorbed. The process was repeated three times to determine desorption efficiencies of the first three desorption adsorption cycles for possible reuse of the adsorbent.

3.8. Experimental Methods of Analysis

3.8.1 Samples Preparation for SEM and TEM characterization

The specimen was cut to size using a rotating saw with diamond-impregnated fine blades. The sizes ranged from a few centimeters in a normal SEM and a few millimeters for TEM. The surfaces were polished to get a flat face by gluing it externally on a metallic mount. This was followed by grinding the surface on abrasive paper. One portion was characterized by TEM (Jeol 200kV FEGTEM Model: 2100F)

The remaining portion of specimen was etched using a suitable chemical etchant ethanol. The specimen was rinsed thoroughly in a non-reactive solvent (e.g., acetone) to prevent further corrosion. Specimens were sputter coated using pure carbon as it gives an almost undetectable signal. The samples were thinned to create foils of 0.1 to 10m m in thickness. Samples were then analyzed by SEM (JOEL JSM 6480LV) for morphology (Pathan *et al.*, 2010).

3.8.2 Samples Preparation for XRD

XRD applications required samples with small particle sizes between a couple of micron to a maximum of 100 micron to achieve a representative sample. Samples were ground to reduce particle/crystallite size. The fine powder was mixed with a binder and pressed into the steel ring to get a mechanical stable sample. The sample was mounted and fed into XRD (Shimadzu XRD-6000) which used X-ray to characterize crystalline material (Hillier, 2000).

3.8.3 Samples Preparation for FTIR

A small amount of powder sample just enough to cover the tip of spatula was mixed with KBr powder. The mixture was subsequently ground for 3-5 minutes in a mortar to fine powder until crystallites (less than 5 mm in diameter), became somewhat

"pasty" and stuck to the mortar. The paste was pressed in Quik Hand press for 2 minutes to form a thin and transparent pellet. The collar together with the pellet was put into the sample holder of FT-IR (Shimadzu FTIR-8400) for analysis (Madejová, 2003).

3.8.4 Samples Preparation for UV-VIS

At least 1ml of samples was put in standard quartz cuvette. 2-5 mL of the solvent used to disperse your material was used to measure the solvent background and for any necessary dilution of the sample. A cuvette with samples was put into UV-VIS spectrometer (Shimadzu V-700) for analysis (Čapek *et al.*, 2005)

3.8.5 Samples Preparation for AAS

1 ml standard solutions of metal ions were put in cuvettes and run to standardize and calibrate the instrument. This was followed by running 1 ml analyte samples to determine their concentrations in the AAS (Unicam Solar-32) (Tüzen, 2003).

3.8.6 Samples Preparation for SQUID

Samples were placed in a capsule. A wad of cotton was placed in the capsule to hold the sample orientation. A small hole was poked in the top of the capsule to allow air to be pumped out. The capsule was inserted inside the straw at the slit. A piece of Kapton tape was placed over the bottom of the straw to keep the sample from sliding out the bottom of the straw and finally loaded into the SQUID equipment (Quantum Design MPMS-3 SQUID VSM) (Fagaly, 2006).

3.9 Data analysis

The results of the analyses in all measurements were done in triplicates and the arithmetic mean obtained by use of equation 3.2;

$$\bar{x} = \sum_i x_i / n \quad \textbf{3.2}$$

Where; $\bar{x}$- arithmetic mean of the samples, x_i - sample measurements and n-population.

Comparison of experimental means of methods of analysis, AAS and UV-VIS was done using ANOVA (Kothari, 2004). XRD data was fitted into the Gaussian and Lorentz distributions to determine the full width at half maximum (FWHM) for determination of crystallite size.

CHAPTER FOUR

RESULTS AND DISCUSSIONS

4.1 Introduction

This chapter presents results and discussions on the synthesis and characterization of carbon nanotubes (CNTs), magnetite and silica coated magnetite nanoparticles, and the fabricated CNT-IPSF/Fe_3O_4 nanocomposites. The pH_{PZC} was obtained since the fabricated CNT-IPSF/Fe_3O_4 nanocomposite has acidic functional groups which may interfere with pollutants' removal. Optimal parameters of adsorption such as adsorbent dosage, contact time, initial concentrations and pH are discussed. Efficiency of fabricated CNT-IPSF/Fe_3O_4 nanocomposites was probed and results compared to that of the commercially available activated carbon adsorbent.

The removal efficiency was investigated based on adsorption features such as contact time, initial concentrations, counter ions and PAHs. Adsorption kinetics and isotherm models were also fitted to the adsorption data to find out the best fit kinetic and isotherm model for pollutants' adsorptions. Application of the adsorbents in the removal of Pb(II) ions and phenanthrenes from wastewater is discussed. Desorption efficiencies of various reagents used were evaluated to determine the best reagent for desorption of the adsorbed Pb(II) ions and phenanthrenes from the adsorbent. Besides the removal capacities reported, desorption-adsorption studies were done to determine regeneration and reusability on the nanocomposites. Data analysis of raw data (Appendices 1-25) for removal of Pb(II) ions and phenanthrenes from both aqueous solutions and wastewater was done.

4.2 Synthesis and Characterization of Carbon Nanotubes (CNTs)

4.2.1 Morphology of CNTs

Morphology of CNTs was determined by scanning electron microscopy (SEM) using a beam of high moving electrons focused at the surface of solid specimen (Goldstein *et al.*, 2012). The SEM image of the prepared carbon nanotubes is shown in figure 4.1. This SEM image shows a configuration of the CNTs material with abundant threadlike entities with diameters in the range 20 - 30 nm. The SEM image further provides evidence of entangled entities characteristic of multiwalled carbon nanotubes (MWNTs). It was difficult to make out the accurate length of the MWNTs from the SEM observation due to the twisting, but the length could be several tens of nanometers.

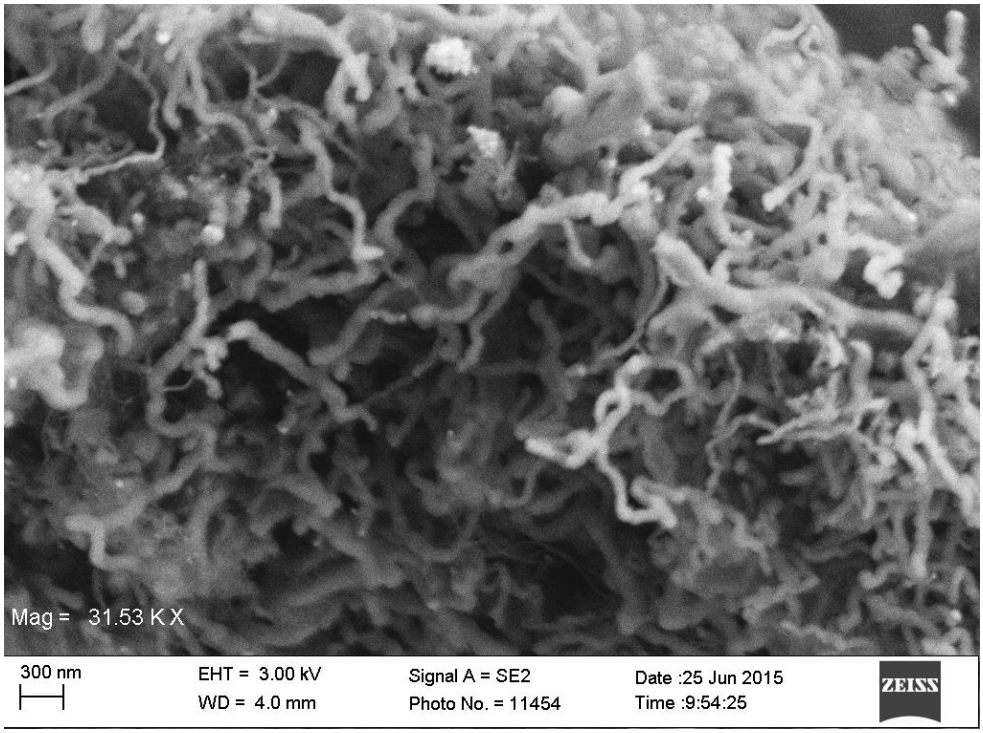

Figure 4. 1 SEM image of the CNTs

The SEM image depicts CNTs with very thin like broadcast of needles with nanotubes density spreading in a very large nanometer range. The SEM micrograph

obtained also shows entangled CNTs, with thin threads of nanotubes which are very appropriate for applications in nanocomposites manipulations.

4.2.2 Microstructure of CNTs

Transmission electron microscopy (TEM) was used to identify the internal structure of carbon nanomaterials. The TEM image in figure 4.2 reveals that the nanotubes obtained display different morphologies under optimized conditions. The TEM image also shows that the enlarged nanotubes exhibit shiny spots on their surfaces depicting presence of carbon molecules which necessitates purification of the nanotubes (Li *et al.*, 2010). Further observations confirm that the long threadlike nanotubes could be in the range of tens of nanometers. Such TEM analysis could easily give information on internal thickness of the nanotubes through proper measurements.

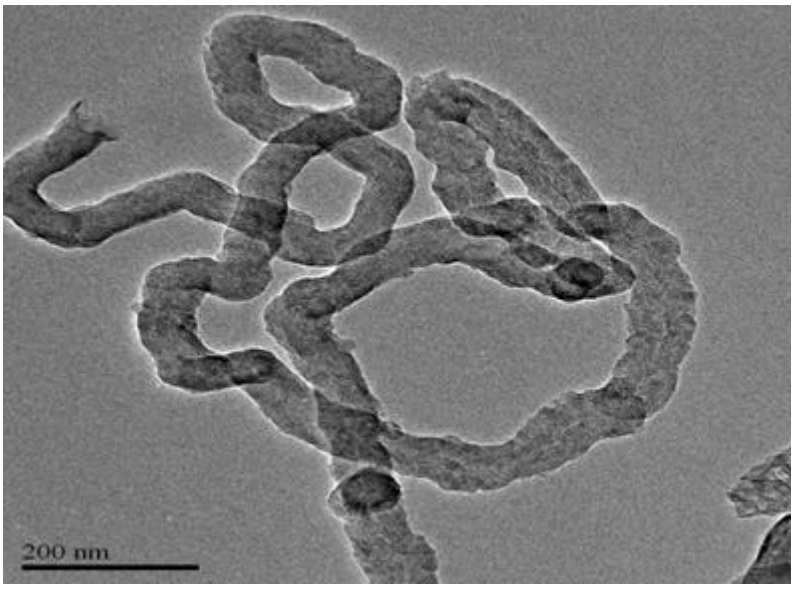

Figure 4. 2 TEM of the CNTs

The mean outer diameter of CNTs was 20-30 nanometers which are in the range for the multiwalled carbon nanotubes. The end tips of the carbon nanotubes are open revealing active sites for further functionalization.

4.2.3 Elemental Analysis

The binding energies of iron (Fe) in the EDS spectrum (Figure 4.3) for CNTs (inset) are depicted by peaks around 0.7, 6.4 and 7.1 keV. The four peaks in the spectrum represent energies for C, O, Si and Fe. The C peak at 0.3 keV contributes to formation of COO− functionality on the surface of CNTs upon oxidation. The finding of this study correlates well with the synthesis of CNTs using silver nanoparticles which had peak at 0.2 for C (Laoui *et al.*, 2015).

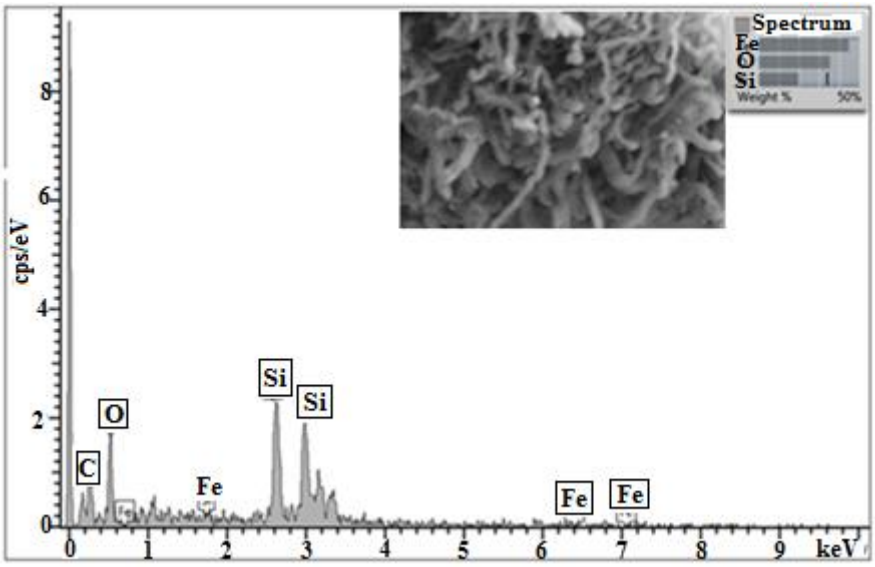

Figure 4. 3 EDS spectrum of MWCNTs

The presence of C and O atoms could signify oxidation by HNO_3 during purification process which may lead to –COO– groups on the CNTs. The end tips of many MWCNTs were opened, indicating the breaking of the C=C bond along the graphene layers of the co-axial tubes (Pierard *et al.*, 2001). The layered structure of the MWCNTs remained largely intact, which indicates that there was no real damage to the MWCNTs during the oxidation process.

The nature of carbon nanotubes formed depends on the synthesis method (bottom-up or top-bottom method) used. In this study, the thread-like CNTs were synthesized

using chemical vapour deposition with ethylene gas as the main source of carbon. During purification of CNTs, their surfaces are linked to different functional groups depending on the oxidizing agent employed (Datsyuk *et al.*, 2008). The presence of these functional groups modifies the surfaces of the CNTs which facilitates further linkages. A modified surface site can lead to increased surface area suitable in many adsorption processes.

The type of catalyst used as substrate also influences the morphology of the formed CNTs. Iron catalyst is suitable in this case since it can withstand high temperatures and the CNTs can easily be absorbed into the molten iron and grow on the iron catalyst substrate by bottom up growth mode.

4.3 Characterization of Magnetite and Silica Coated Magnetite Nanoparticles

4.3.1 Absorption in Electromagnetic Spectrum

The UV-Vis spectrum for magnetite and core shell nanoparticles is shown in figure 4.4a and 4.4b respectively.

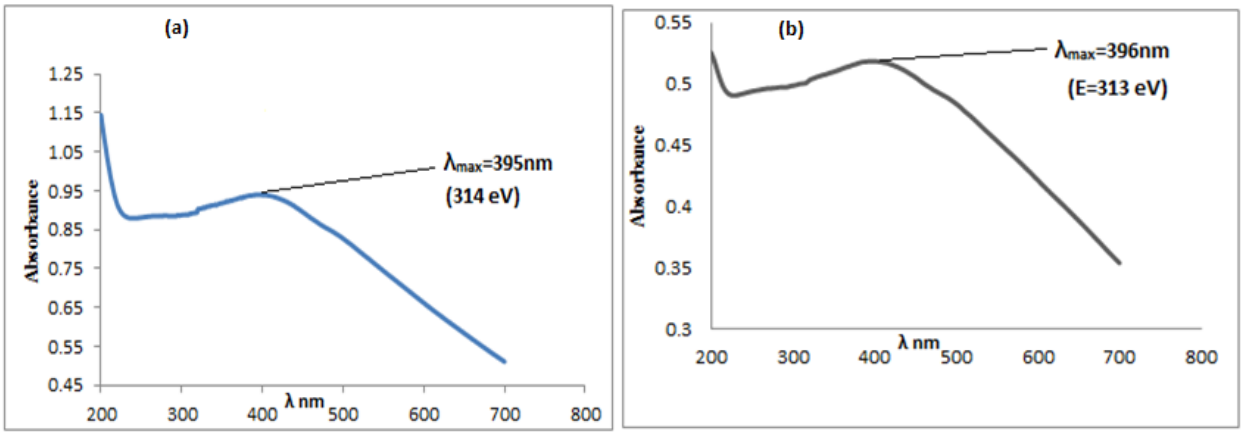

Figure 4. 4 UV-Vis for (a) magnetite NPs (Fe_3O_4) and (b) core shell NPs ($Fe_3O_4.SiO_2$)

It is evident that the magnetite and core shell nanoparticles absorbed at 395 nm to 396 nm respectively. During absorption of the UV energy by an atom or molecule, electrons can be promoted from their ground state to an excited state through rotation or vibration (Valeur and Santos, 2012). These vibrations and rotations have discrete energy levels, which are packed on top of each electronic level. The excitation of electrons (π, δ or n electrons; charge transfer electrons; and d and f electrons) is related to specific radiation in the UV-visible region. Many inorganic species reveal charge-transfer absorption which exists in charge-transfer complexes. In such complexes, the components must have electron donating and accepting properties.

A shift in the spectra implies some physical properties of the sample have changed (Storhoff *et al.,* 2000). In the UV-Vis spectroscopy, the presence of a shift could imply that the electronic structure has been modified by the dopants (silica shell). Dopant atoms can now act as activation centers for scattering. A shift in UV-Vis absorptions from magnetite and core shell nanoparticles could be explained from the concepts of plasmonics. Plasmons are oscillations of free electrons that result from the formation of a dipole in the material due to electromagnetic waves. Free electrons of metallic nanoparticle (MNP) exist in the surfaces of the nanoparticles. When incident light interact with these nanoparticles, the free electrons in its surface will oscillate. During absorption, the light waves oscillate, leading to a constant shift in the dipole that forces the electrons to oscillate at the same frequency as the light. Therefore, the corresponding blue shift or red shift appears.

The band-gap energy is related to the absorbance peak wavelength. Conversion of peak wavelength into band-gap energy was calculated from the Einstein-plank's relation (Equation 4.1);

$$E = hc/\lambda \text{.....} \textbf{4.1}$$

where E = band gap energy, h = planck's constant, c = velocity of light, λ = maximum absorbed wavelength.

By putting the respective values in the above equation, the obtained energy of band gap was 3.14 eV (Equation 4.2) and 3.13 eV (Equation 4.3) for (a) magnetite NPs and (b) core shell NPs at 395 nm and 396 nm respectively;

$$Em = \frac{(6.626 \times 10^{-34}\ Js)(3.0 \times 10^{8} m/s)}{(395 \times 10^{-9}\text{m})(1.602 \times 10^{-19} J)} = 3.14\ eV \text{.....} \textbf{4.2}$$

$$Ecs = \frac{(6.626 \times 10^{-34}\ Js)(3.0 \times 10^{8} m/s)}{(396 \times 10^{-9}\text{m})(1.602 \times 10^{-19} J)} = 3.13\ eV \text{.....} \textbf{4.3}$$

where Em and Ecs are band gap energies for magnetite and core shell respectively. The UV-Vis spectroscopy revealed that the core shell NPs were in nanoparticle form showing enhancement in band gap energy, which is higher than the corresponding magnetite NPs. The results obtained, proved that the core shell synthesized were quite stable and in nano range of less than 100 nm (Lahure, 2015).

Shifting of the absorption peak to a higher wavelength side was due to the addition of tetraethyl orthosilicate(TEOS). The decrease in band gap energy of a material due to an increase in particle size, resulted in a red-shift in wavelength from 395 nm (Figure 4.4a) to 396 nm (Figure 4.4b) (Pala *et al.*, 2009). Such a shift in band gap is related to size quantization effect occurring due to discrete energy levels. The energy levels cease to be discrete as the size of the particle increases which decreases the band gap energy of the material. The synthesized core shell NPs had smaller band gap energy implying their higher stability arising from silica shell (Kulkarni *et al.*, 2014). Consequently, the above results correlate closely well with other workers when they

used pure magnetite NPs (Huang *et al.*, 2014). The band gap energy of 3.13 eV for core shell nanoparticles confirms formation of nanosized particles which agrees with that which obtained band gap energy for nano-β-HgS as 3.6 eV from the UV–visible spectral measurement (Marimuthu *et al.*, 2012).

4.3.2 Determination of Functional Groups

Infrared spectroscopy is an absorption method in the wavelength region of 1 to 100 µm and extends from the region of the visible light to longer wavelengths and smaller frequencies (Pogue *et al.*, 2001). Fourier transform infrared spectroscopy was used to analyze the surface of the magnetite core before and after functionalization with silica to form core shell nanoparticles (Figure 4.5).

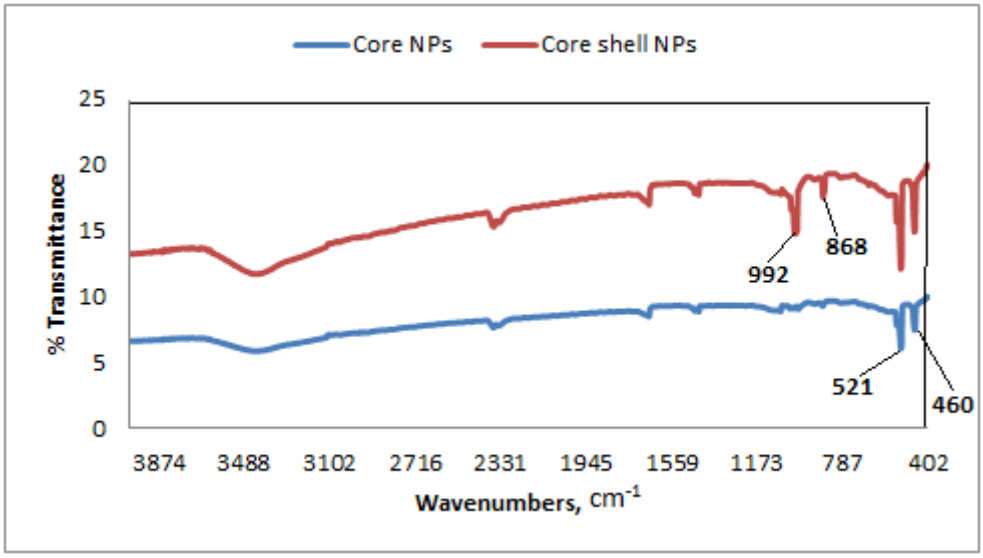

Figure 4. 5 IR spectra for magnetite core and core shell nanoparticles

The presence of absorption band between 460 cm^{-1} and 521 cm^{-1} is assigned to the vibrations of Fe–O bonding in magnetite core (Fe_3O_4) nanoparticles (Yang *et al.*, 2008). Previously, it was reported that the absorption band for Fe-O occurred at 570 and 400 cm^{-1} wave number (Jayaprabha and Joy, 2014). However, in the present study, the band for Fe-O shift towards lower wave number of 521 cm^{-1} as a result of

rearrangement of localized electrons on the particle surface due to the breaking of the large number of bands on the surface atoms (Ngo *et al.*, 2010). The absorption band at 521 cm^{-1} could also be due to the Fe–O bonds in tetrahedral positions of the spinel inverse structure of the magnetite nanoparticles.

In the spectrum of the core shell nanoparticles, additional bands were found at 992 cm^{-1} and 868 cm^{-1} which confirmed stretching−vibration bands for Si–O and Si–O–Si bonds respectively. The Si−O and Si–O–Si stretching vibration bands confirmed the formation of SiO_2 shell on Fe_3O_4 core nanoparticles. Other studies found that strong network of Si−O bond developed at 1020 – 1040 cm^{-1} due to addition of TEOS (Kulkarni *et al.*, 2014).

4.3.3 Morphology of Core and Core Shell NPs

The SEM analysis was done to determine surface distribution of synthesized nanoparticles. The SEM micrographs of the magnetite core (Fe_3O_4) (Figure 4.6a) and core shell ($Fe_3O_4.SiO_2$) nanoparticles are shown in Figure 4.6b. Large quantities of aggregated magnetite nanoparticles with moderately uniform and oval shapes were observed (Figure 4.6a). A clear, dispersed and distinct spherical particles were obtained (Figure 4.6b) with the addition of TEOS content.

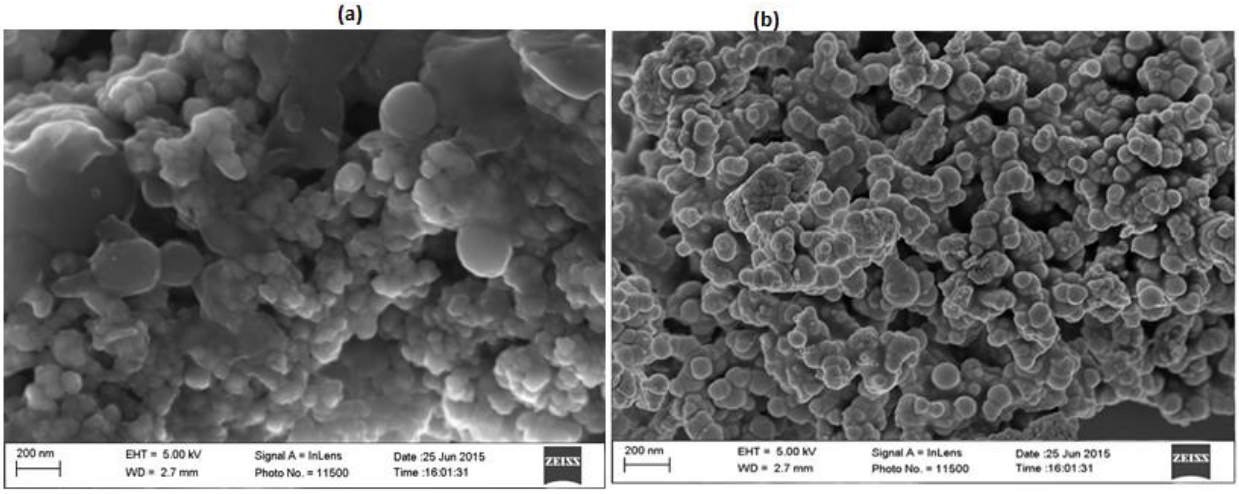

Figure 4. 6 SEM micrograph for (a) magnetite core and (b) core shell NPs

Studies have found that variation in amount of the TEOS, silica-coated magnetite particles leads to uniform and more monodispersed due to the reduction in their relative sizes (Zhao *et al.,* 2005). Figure 4.6b also shows that the nanoparticles were arranged in a closed packed manner, with varying pores depicting porosity of the synthesized nanoparticles. This property of the nanoparticles could be well suited for many applications involving its incorporation during nanocomposites fabrication (Wei *et al.*, 2012; Sodipo and Aziz, 2013).

4.3.4 Crystallite Structure and Size

4.3.4.1 Structure of Nanoparticles

X-ray powder diffraction (XRD) is a rapid analytical technique primarily used to analyze particles for their crystallinity with additional information on their unit cell dimensions (Suryanarayana and Norton, 2013). The synthesized core shell nanoparticles were analyzed using X-ray diffractometry (Shimadzu, XRD-6000) with CuKα radiation source using nickel. The XRD pattern for the core shell nanoparticles is shown in figure 4.7.

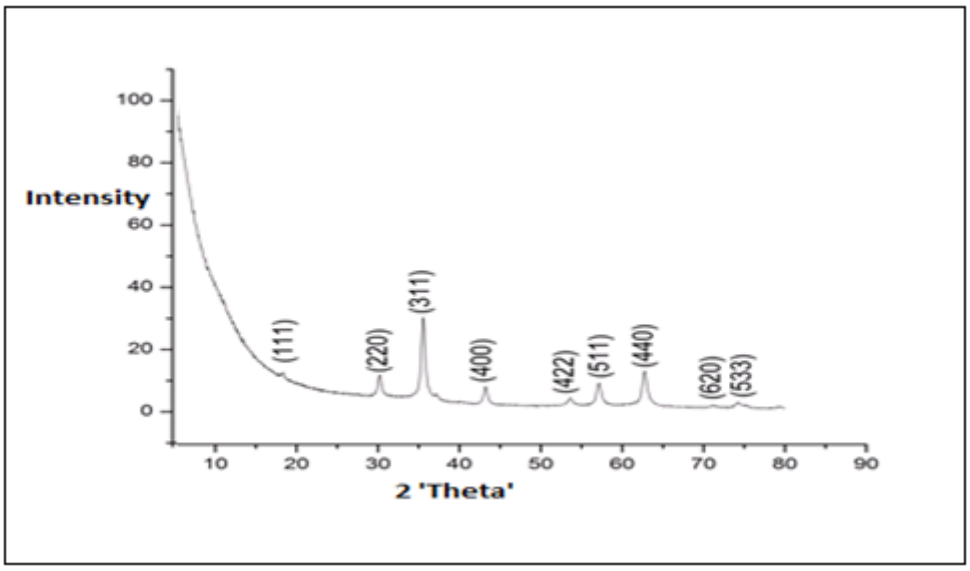

Figure 4. 7 XRD pattern for Core Shell NPs

The X-ray diffraction pattern of the core shell NPs matched the same pattern for the magnetite (Fe_3O_4) phase as compared to standard XRD patterns reported elsewhere (Xu *et al.*, 2010). The sharp peaks that appeared approximately at 2θ = 30.20°, 35.52°, 43.20°, 57.21°, and 62.73° belonged to the $Fe_3O_4.SiO_2$ nanocrystalline structure. A comprehensive characterization of the precursor by single crystal X-ray crystallography shows the presence of Fe_3O_4-SiO_2 coordination environment. The crystal structure of magnetite nanoparticles has an inverse spinel pattern exhibiting alternating octahedral and tetrahedral-octahedral layers (Blaney, 2007). Furthermore, the magnetite unit cells adhere to the face-centered cubic pattern with crystal lattice.

Studies have found that the bulk magnetite particles exhibit twinning along the cubic plane; with the main crystallographic direction occurring on the (111) plane (Lopez *et al.*, 2010). The diffraction pattern showed that the synthesized core shell nanoparticles were crystalline, while the position and the relative intensity of the diffraction peaks matched the standard XRD data (JCPDS file No. 19-0629) (Zhan *et al.*, 2011). The peaks at (220), (311), (400), (422), (511) and (440) planes correspond to a cubic unit

cell, for a cubic spinel structure due to the strongest reflection that proceeds from the (311) plane. The ferrimagnetic property based on the theoretical framework describes the crystal structure of magnetite nanoparticles. The spinel structure of crystallized magnetite contains oxygen ions in close packed cubic arrangement while the gaps are filled by the smaller Fe ions. The tetrahedral site of the gaps contain Fe ion surrounded by four oxygen atoms while the octahedral site has Fe ion surrounded by six oxygen atoms.

Two magnetic sub-lattices X and Y, having spins antiparallel to each other are formed from tetrahedral and octahedral sites. Since the tetrahedral and octahedral sites differ, magnetite structural formula, $[Fe^{3+}]X\ [Fe^{3+},Fe^{2+}]Y\ O_4$ arise from the interactions of the iron ions between and within the two types of sites. The crystalline structure for the prepared core shell nanoparticles has an inverse spinel structure arising from the particular arrangement of cations on the X and Y sub-lattices (Senz *et al.*, 2001).

4.3.4.2 Crystallite Size

Peak width of the crystallites varies inversely with crystallite size i.e. as the peak gets broader, the crystallite size gets smaller (Rehani *et al.*, 2006). The peak width broadening is most pronounced at greater angles 2θ. Further, the instrumental profile width broadening is also largest at large angles 2θ. However, peak intensity is usually weakest at larger 2θ angles. Therefore, the use of a single more intense peak, often gives better results from diffraction peaks between 30 and 50 deg 2θ. It has been shown that at below 30 deg 2θ, the peak asymmetry compromises profile analysis.

From figure 4.7, the most intense peak appearing at 35.52 deg 2θ was used in determination of crystalline sizes. Fitting the XRD data to Gaussian (Figure 4.8a) and

Lorentz line profile (Figure 4.8b), two patterns were obtained from which crystallite size was determined.

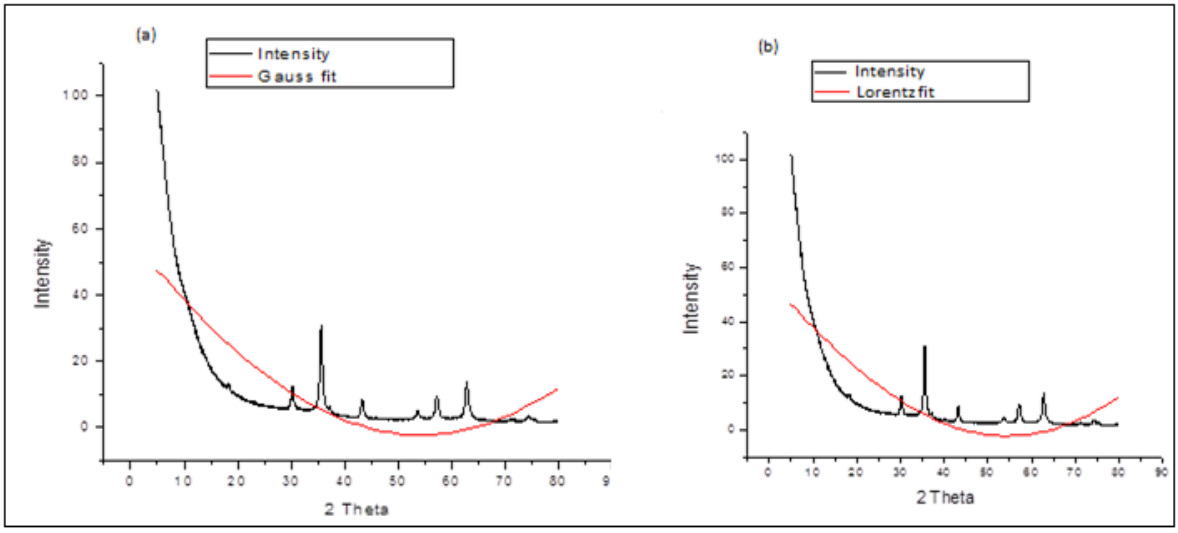

Figure 4. 8 Line profiles for (a) Gaussian and (b) Lorentz for magnetite silica NPs

The crystallite size for the most intense peak at D(311) was determined from the two line profiles using the Debye-Scherrer formula 4.4;

$$T = C\lambda/Bcos\theta = C\lambda/[\left(B_{sp}^2 - B_{St}^2\right)^{\frac{1}{2}}cos\theta] \quad \text{.....4.4}$$

where T is the thickness of crystal, λ the wavelength of the X-rays, θ the Bragg angle, and C is the Scherrer shape constant, corresponding to the value for core shell nanoparticles. B is the full-width at half-maximum (FWHM) of the peak (radians) corrected for instrumental broadening. B_{sp} and B_{st} are the FWHMs of the sample and of a standard, respectively. This means that FWHM is the width of a spectrum curve measured between those points on the *y*-axis which are half the maximum amplitude. The sample shows very intense peaks, indicating the ultra-fine nature and a small crystallite size (Ghandoor *et al.*, 2012). Crystallite size measurements (Table 4.1) were determined as 22.4 nm from the strongest reflection of the (311) peak, based on

the Debye-Scherrer approximation, which assumes that small sizes of crystallites causes line broadening (Shaaban *et al.*, 2013).

Table 4.1 Determination of particle size

Line profile	θ	$B_{Standard}$	B_{Sample}	βcosθ	C	λ	T	$T_{average}$
Gaussian 2θ = 35.52	17.72	54	178	118.09	0.9	350	26.7	22.4 nm
Lorentz 2θ = 35.52	17.72	54	272	207.61	0.9	350	18.1	

The T value of 22.4 nm confirms that the synthesized core shell particles were in the nanoscale range 1-100 nm for nanoparticles. Such small particle sizes increases the surface area of the adsorbent for adsorptions studies.

4.3.5 Magnetic Property of Core Shell NPs

4.3.5.1 Magnetization Curve

Magnetic behaviour of different magnetic substances is demonstrated by a plot of magnetic flux density, B(M), against applied magnetic field, H (Chen, 2013). The magnetization curve of the synthesized core shell ($Fe_3O_4.SiO_2$) nanoparticles at room temperature is shown in figure 4.9.

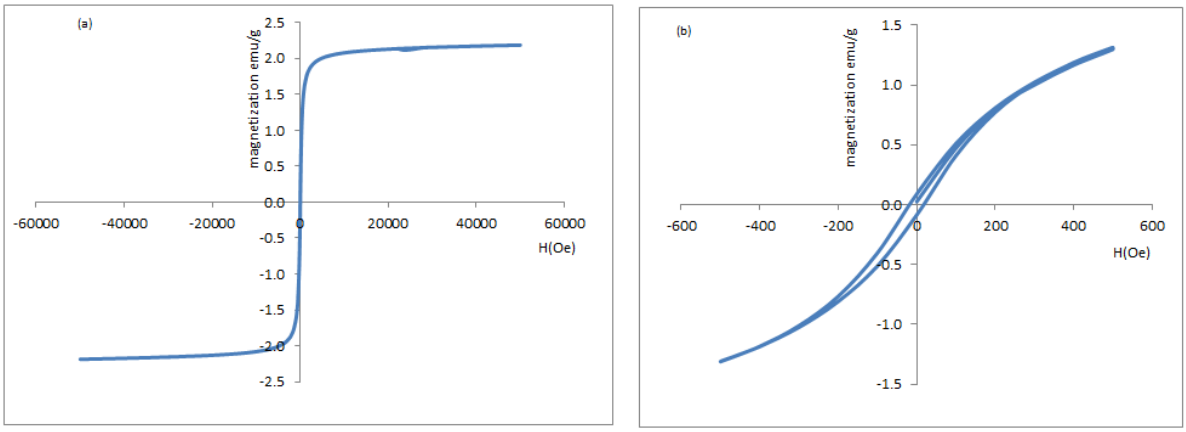

Figure 4. 9 Magnetization Curve for (a) synthesized $Fe_3O_4.SiO_2$ nanoparticles and (b) its expanded low field region at room temperature

From figure 4.9a, the greater the amount of current applied, H(Oe), the stronger the magnetic field in the component B(M). In figure 4.9b, the curve ‘oa’ is non-linear because the material is being magnetized as the applied field is applied. Most of the magnetic domains are aligned with maximum magnetization at point “a” where any additional increase in the applied magnetic field had very little change in magnetization. The material is said to be at the point of magnetic saturation (2.2 emu g^{-1}). When H(Oe) is reduced to zero, the magnetization curve change from point "a" to point "b" showing that some magnetic flux reduced with magnetizing force. On reversal of the magnetizing force, the curve moves to point "c", where the magnetization is zero. This is called the point of coercivity on the curve where the reversed magnetizing force has flipped enough of the domains so that the net flux within the material is negligible (Sadaka *et al.*, 2007). When the magnetizing force was increased in the negative direction, the material again became magnetically saturated upon reaching point "d". As H(Oe) increases from d, the magnetization increases back to point “a” in a different path through “e” and “f”.

Hysteresis curves relate changes in magnetization M, with applied magnetic field H(Oe), and such changes depend on magnetic domains in the material (Cullity and Graham, 2011). Although domains are magnetized in different directions, each domain has uniform magnetization which can be less than saturation magnetization Ms, or even zero. This is because any system exists in a state of minimum energy. The directions in which the magnetization is allowed for a material can be restricted due to the crystalline nature of most materials. Certain crystallographic directions which are parallel to magnetization are preferred. This means that upon deviation of magnetization from such directions, an extra cost (anisotropy) is required. Studies

have shown that anisotropy energy can be minimum when its magnetization is aligned along (220), (311), (400), (422) directions. This is the case for core shell NPs in this study along (311) which is an easy axis since magnetic field is applied in this direction thus resulting in saturation magnetization.

4.3.5.2 Saturation Magnetization

In order to identify the magnetic property of the prepared core shell nanoparticles, different types of magnetism and their response to magnetic fields must be well understood. A memory of an applied field (called hysteresis) is retained by magnetic materials upon removal and when magnetization is plotted against magnetic field, magnetism is revealed in form of a hysteresis loop (Cullity and Graham, 2011). Ferrimagnetic materials exhibit a hysteresis loop which is narrower about the origin than antiferromagnetic materials due to smaller coercivities. This could also be explained in terms of their ability to be demagnetized such that ferromagnetic materials are easily demagnetized than antiferromagnetic materials. The prepared core shell NPs have thin hysteresis loop with coercivity close to zero showing they could be ferrimagnetic (Dormann and Fiorani, 2012). Furthermore, its external field response followed a sigmoidal curve, a characteristic property of such material (Kolhatkar *et al.*, 2013).

A related term is the saturation magnetization, Ms, which is the maximum induced magnetic moment that can be obtained in a magnetic field; beyond which no further increase in magnetization occurs. The Ms of the core shell nanoparticles was determined as 2.2 emu g^{-1}. This value was almost equivalent to 3.21 emu g^{-1} for silica coated magnetite nanoparticles (He *et al.*, 2007), but less than 7.5 emu g^{-1} for synthesized magnetic mesoporous silica−graphene oxide (MMSP-GO) (Wang *et al.*,

2013) and 90-92 $emug^{-1}$ for the bulk Fe_3O_4 (Cornell and Schwertmann, 2003). The lower density of the magnetic component in the nanoparticle samples could have resulted in the smaller saturation magnetization, M_s value. The lower Ms values could also be due to the diamagnetic nature of the thick silica shell used in coating the magnetic cores (He *et al.*, 2007).

4.4 Morphology and Elemental Analysis of CNT-IPSF/F_3O_4 Nanocomposites

The structure of the CNT-IPSF/Fe_3O_4 nanocomposites was characterized by SEM–EDAX technique. The SEM micrograph of the fabricated CNT-IPSF/Fe_3O_4 nanocomposites is shown in figure 4.10.

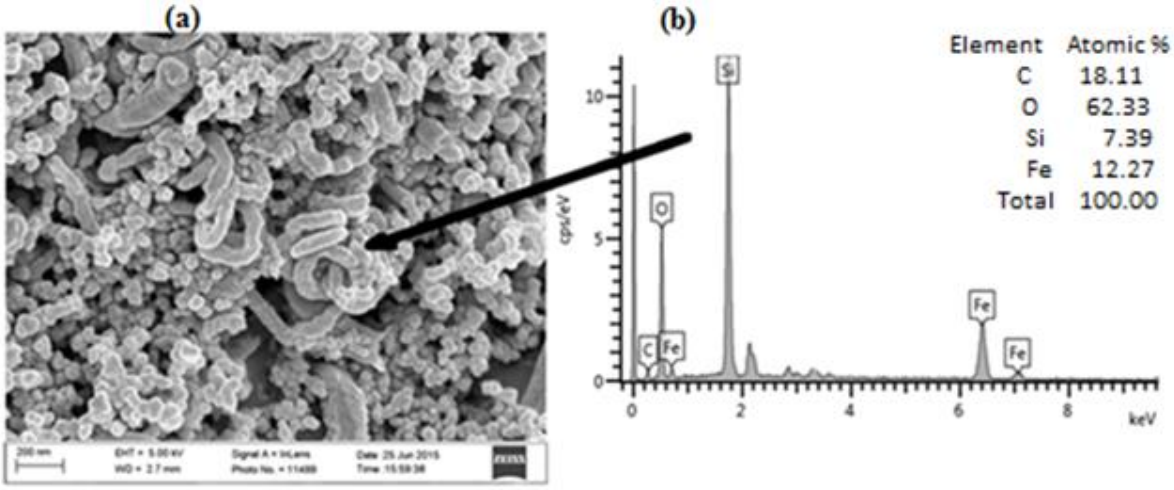

Figure 4. 10 SEM Micrograph of CNT-IPSF/Fe_3O_4 nanocomposite and its Elemental Analysis

From figure 4.10a, the surface of the CNT-IPSF/Fe_3O_4 nanocomposites is irregular and rough with open porous structure suitable in adsorption studies. Such structure allows the pollutants to be trapped onto the nanocomposite surface during adsorption studies. The large cavities of the pores allows penetration of pollutants into the nanocomposite surface (Saravanan and Ravikumar, 2015). The cylindrical needle-like threads of CNTs can be seen intertwined with the core shell nanoparticles. The SEM

micrograph revealed closely packed and uniform structure with higher surface area suitable for adsorption studies.

In addition, the EDS spectrum for the CNT-IPSF/Fe_3O_4 nanocomposites is shown in figure 4.10b. The binding energies of La, Ka and Kb shells correspond to peaks at around 0.7, 6.4 and 7.1 keV respectively for Fe. The other three peaks mainly for C, O and Si atoms are shown in the spectrum. The oxidation of CNTs leads to attachment of COO- group on the surface of CNTs as shown by the C and O peaks at 0.3 and 0.5 respectively in the spectrum. From the EDX analysis, Fe, O and C atoms are the main constituents in the fabricated nanocomposites. The finding of this study correlates well with the synthesis of biocompatible magnetic iron oxides using oleic acid (OA) which obtained only three peaks for C, O and Fe where C was for OA functionality on the surface of iron oxides nanoparticles (Mahdavi *et al.*, 2013b).

4.5 Removal of Pb(II) ions Using CNT-IPSF/Fe_3O_4 Nanocomposites

4.5.1 Optimization Parameters

4.5.1.1 The pH_{PZC} of CNT-IPSF/Fe_3O_4 Nanocomposites

A number of methods for determining the point of zero charge (pH_{PZC}) in materials have been proposed such as potentiometric titration, non-specific ion adsorption and methods based on the mobility of charged particles in an electrical field (Appel *et al.*, 2003). However most of the research on nanocomposite materials has focused on the use of solid addition method due to its simplicity. The pH_{PZC} was used to investigate whether the surfaces of nanocomposites had polar functional groups attached. From the pH_{PZC} curve of the sample, the pH_{PZC} value was found to be around 4.5 (Figure 4.11).

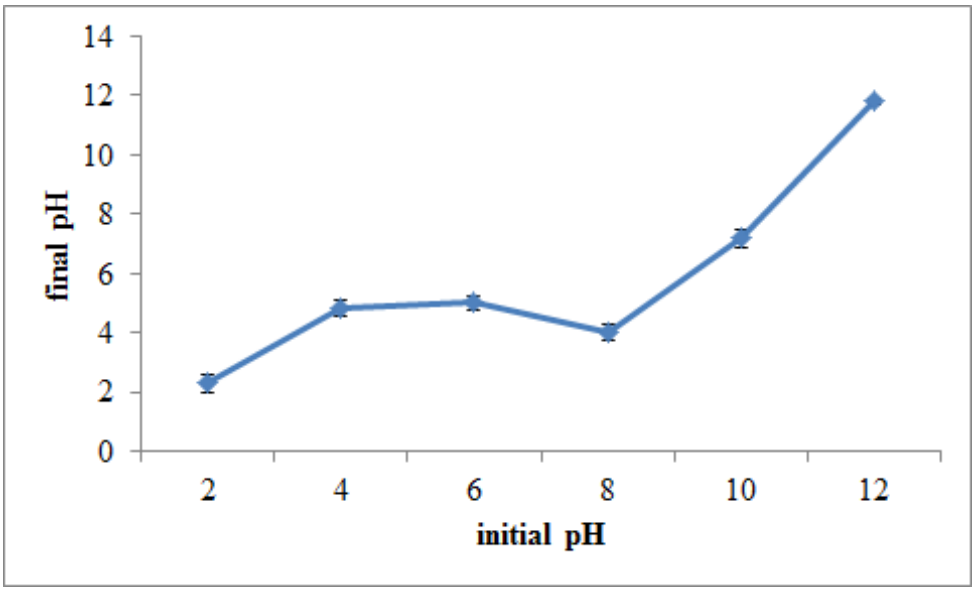

Figure 4. 11 Plot showing the pH_{PZC} for CNT-IPSF/Fe_3O_4 nanocomposites

This study used pH > 4.5 for removal of Pb(II) ions from the solution, hence all the adsorption experiments were conducted at optimal pH 5. The findings of pH_{PZC} = 4.5 from this study are close to 4.4 from the study on polysaccharide extract (Onditi *et al.*, 2016). The presence of acidic oxygen-bearing functional groups, such as –COOH and −OH groups on the nanocomposite surface was confirmed (Smičiklas *et al.*, 2000). At pH_{PZC} values 6-8, such groups become negatively charged due to abstraction of H ions thus acting as vacant sites for attraction of positively charged metal ions (Crabtree, 2009). The nanocomposites required no further functionalization because the MWCNTs had initially been functionalized using mineral acid HNO_3 during purification stage, making it economical. The presence of functional groups enhances binding of the Pb^{2+} ions onto the adsorbent surface through electrostatic interaction or by cation exchange. The saturation point of adsorption features on the nanocomposites was investigated at lower detectable Pb(II) ions concentrations of 2 and 4 mg/L.

4.5.1.2 Effect of Adsorbent Dosage on Pb(II) ions Adsorption

The adsorption of lead(II) ions on adsorbent was studied by varying the adsorbent dosage from 0.02 – 0.12 g while keeping other operational parameters constant: pH 5 (adjusted by adding 0.1 M HCl or NaOH), shaking speed 120 rpm and temperature 25 °C. The pH of the solution was maintained at a defined value by manually adding 0.1 M HCl and/or NaOH solutions.

The removal efficiency of the Pb(II) ions was measured for different masses of adsorbent using lead (II) ions concentration of 2 mg /L and 4 mg/L (Figure 4.12).

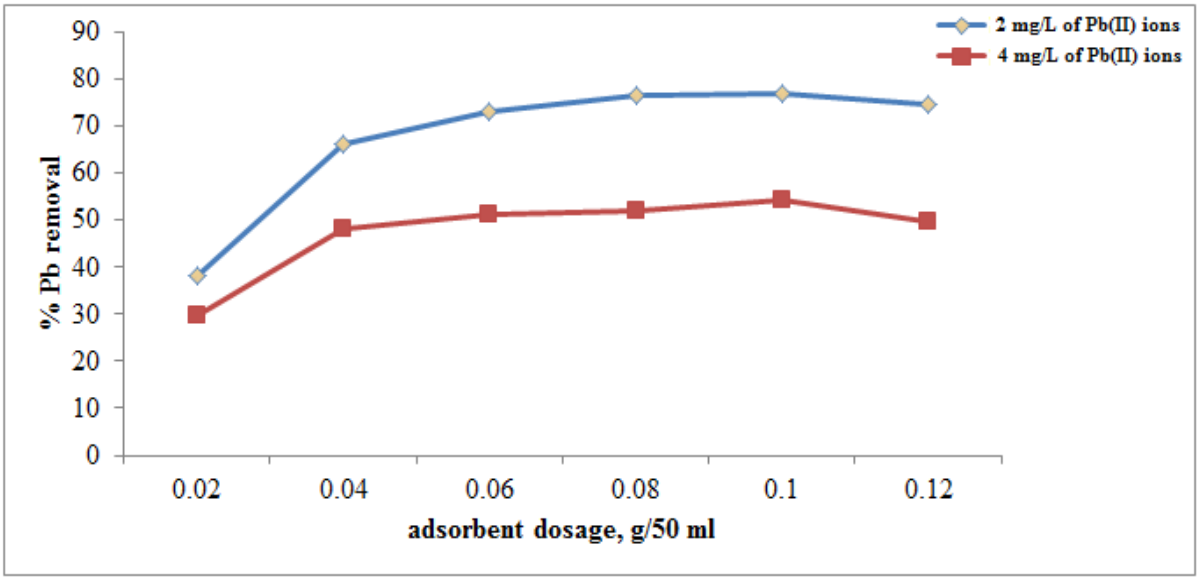

Figure 4. 12 Effect of adsorbent dose on Pb(II) ions adsorption

Removal of lead(II) ions by the adsorbent increased sharply from adsorbent dosage of 0.02 g to 0.04 g but the rate decreased slightly as 0.12 g mass was approached (Figure 4.12). The initial increase in adsorption could be due to the fact that the adsorptive capacity of adsorbent available was not fully utilized at a higher adsorbent dosage in comparison to lower initial Pb(II) ions concentration used (Amarasinghe and Williams, 2007). The adsorption of Pb^{2+} ions reached maximum after 0.05 g

adsorbent dose was applied, achieving removal efficiency of 77 % and 54 % for 2 and 4 mg/L Pb^{2+} ions concentrations respectively. There was a small decrease in metal ions removal as adsorbent dose increased from 0.06 to 0.1 g. This may be due to the fact that an increase in the adsorbent dose could lead to availability of more sites on the adsorbent in relation to constant available Pb(II) ions concentration (Ngah and Fatinathan, 2008).

Other studies also found that there was decreased adsorption of divalent metal ions Cu^{2+}, Zn^{2+} at higher adsorbent doses (Wang and Chen, 2009). Subsequent experiments were therefore conducted using 0.05 g as the optimum adsorbent dose. Results show that with addition of between 0.01 and 0.02 g adsorbent dose, there was higher % removal for 2 mg/L Pb^{2+} ions (38 – 66 %) than for 4 mg/L (29 – 48 %) for Pb^{2+} ions solutions.

4.5.1.3 Effect of Contact Time on Pb(II) ions Adsorption

This study investigated the removal efficiency of Pb^{2+} ions at different contact times in the range of 10 to 240 minutes. The experimental data were measured at 240 minutes to ensure that a full equilibrium was attained. The initial Pb(II) ions concentration was kept constant i.e. 2 and 4 mg/L and a constant adsorbent dose of 0.05 g/50 ml was applied (Figure 4.13).

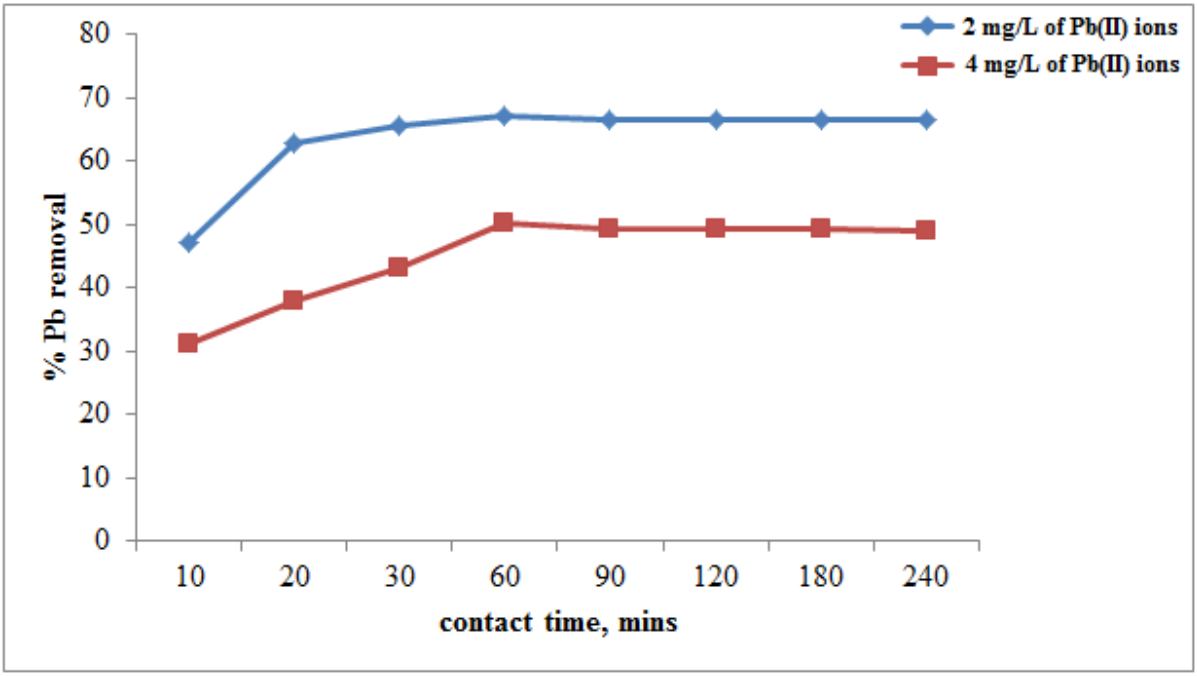

Figure 4. 13 Effect of contact time on Pb(II) ions Adsorption

The rate of adsorption initially increased rapidly, and the optimal removal efficiency was reached within about 60 minutes. Further increase in contact time did not show significant change in equilibrium concentration since the adsorption phase had reached equilibrium and all empty sites had been occupied. It can be observed that the maximum adsorption capacities of Pb(II) ions were about 67.0 % and 50.2 % (Figure. 4.13) after 60 minutes for initial concentrations of 2 and 4 mg/L, respectively. This could be due to easy movement of the Pb(II) ions onto the empty adsorption sites on the surface of the nanocomposites (Al-Degs *et al.*, 2006). It is clear from the above graph that once the equilibrium was reached, further increase in contact time had no significant effect on Pb(II) ions removal. This is because all the available active centers on the adsorbent had been occupied and there was no further sites implying no possibility of any further adsorption (Crini *et al.*, 2007).

There was maximum removal of Pb^{2+} ions of above 50 % at 60 minutes of contact time indicating that optimum conditions had been reached. This means that beyond this optimum time, there was repulsion of the already adsorbed lead(II) ions on the adsorbent and those Pb(II) ions in the aqueous phase (Sreejalekshmi *et al.*, 2009). The mechanism for Pb(II) ions adsorption could be due to attraction of positively charged Pb(II) ions onto negatively charged surface through electrostatic interaction or cation exchange. Further investigations were done using 60 minutes as an optimum time.

4.5.1.4 Effect of pH on Pb(II) ions Adsorption

The pH of the solution influences the adsorbents' surface charge and distribution of the ionic forms of the metal ions (Das *et al.*, 2008). The effects of solution pH on lead(II) removal by the adsorbent was investigated at different pH values (from 1 to 7) using 60 minutes as optimum time and all measurements were made at room temperature for initial Pb(II) ions concentrations of 2 and 4 mg/L as in figure 4.14. The pH of the solution was maintained at a defined value by manually adding 0.1 M HCl and/or NaOH solutions.

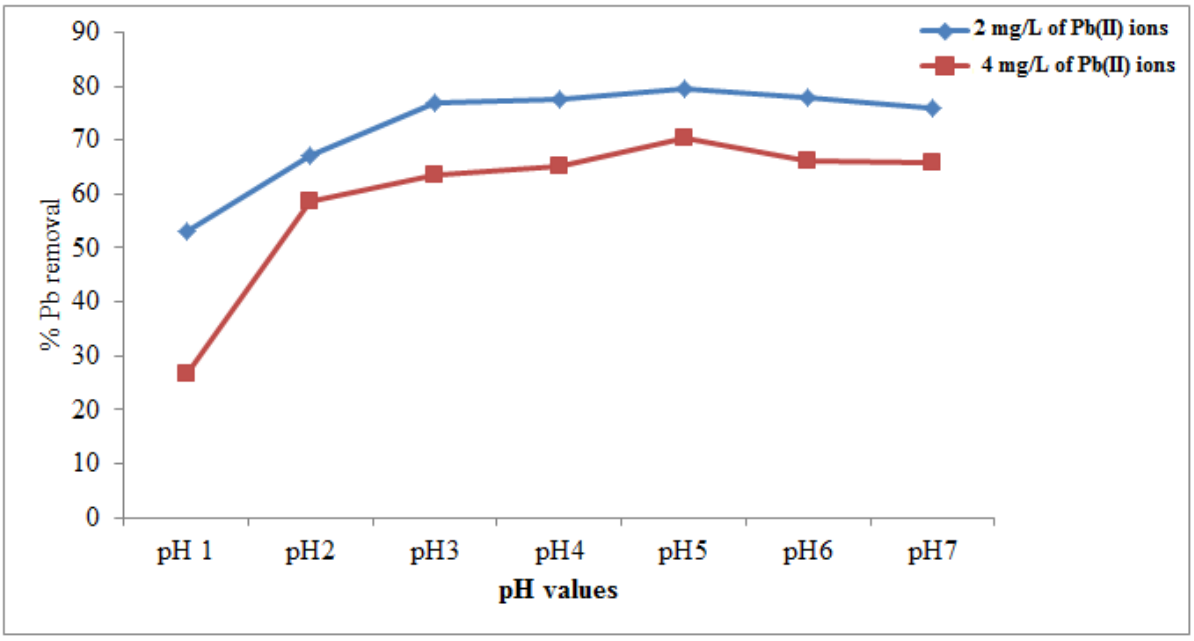

Figure 4. 14 Effect of pH on Pb(II) ions Adsorption

Pb(II) ions adsorption gradually increased as pH was increased from 1 to 2, accounting for 14 % and 32 % increase in Pb(II) ions removal from 2 mg/L and 4 mg/L pb(II) ions solutions. The Pb(II) ions removal is affected by pH of solution whose hydrogen ion concentration determines the amount of metal ions removed. At pH around 4.5, hydrogen ions are likely to compete with Pb(II) ions. At pH values above 5.0, the Pb(II) ions could precipitate as hydroxides thereby decreasing the Pb(II) ions removal (Göksungur *et al.*, 2005). Maximum adsorptions of 79 % and 70 % were determined at pH 5.0 for 2 and 4 mg/L Pb^{2+} ions concentrations respectively. Thus, these results demonstrate that the removal of Pb(II) ions was mainly dependent on the H^{+} ions concentration in the solution. Onditi et al; (2016) in their study observed maximum adsorption of Pb^{2+} ions on polysaccharide extract of 31 % at pH 6 (Onditi *et al.*, 2016).

At lower pH (1-3), the surfaces of the adsorbents are net positively charged due to the protonation of –COO− and –OH functional groups on the nanocomposite. The low

adsorption levels at the pH of 1 was due to repulsion of positively charged Pb(II) ions by the positively charged nanocomposite surfaces (Meena *et al.*, 2005). Above pH 5, deprotonation of surface functional groups occurred which created more negative charges on adsorbent surface that favoured their adsorption. From possible precipitation of cations as hydroxides at pH 5−7, determination of reliable adsorption capacity in this range is not possible.

4.5.2 Kinetics Model for Pb(II) ions Adsorption

4.5.2.1 Effect of Contact Time on Pb(II) ions Adsorption

Adsorption kinetics experiments were carried out on CNT-IPSF/Fe_3O_4 nanocomposites at varying contact times and the results were compared to that of activated carbon, a standard adsorbent in the market. The experimental values for adsorption of lead (II) ions involved agitating 0.05 g/50 mL prepared (CNT-IPSF/Fe_3O_4) and standard (activated carbon) mixtures of 2 mg/L Pb(II) ions concentrations at 10-250 minutes contact times, 25 ℃ and pH5 as shown in figure 4.15.

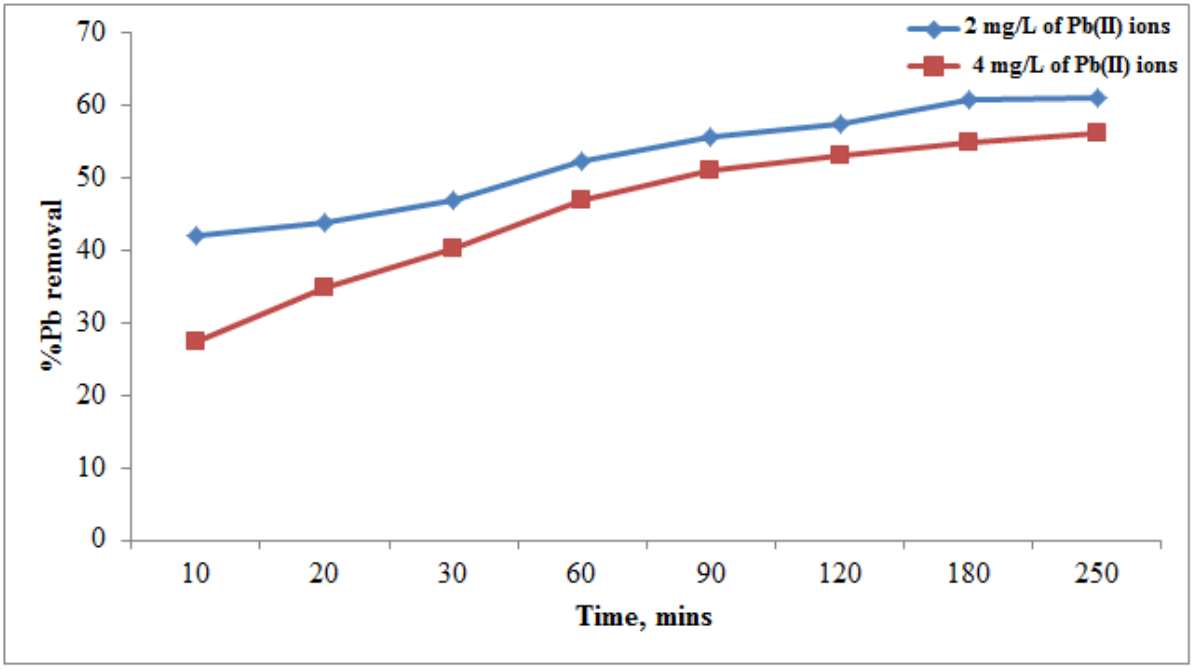

Figure 4. 15 Kinetics for Pb(II) ions adsorption on CNT-IPSF/Fe_3O_4 and activated carbon

The results show that the adsorption rate was fastest up to 60 minutes for both adsorbents due to high initial concentration of Pb (II) ions. As the contact time increases, more and more Pb(II) ions bind onto adsorbent surfaces until no more site is available. Beyond 90 minutes of adsorption, there was no significant change (p=0.05) in adsorption on further increase of the contact time due to the complete utilization of binding sites (Bankar *et al.*, 2009). The CNT-IPSF/Fe_3O_4 nanocomposites had higher percentage Pb(II) ions removal in the whole time range than activated carbon adsorbent (p=0.05) at 2 mg/L of initial Pb(II) ions concentrations.

4.5.2.2 Kinetic Models for Pb(II) ions Adsorption

The presence of functional groups on the surface of the fabricated CNT-IPSF/Fe_3O_4 nanocomposites has been reported to form chemical bonds between the active sites of nanocomposites and divalent Pb^{2+} ions (chemisorption) (Porjazoska *et al.*, 2015).

Kinetic models based on adsorption capacities instead of solution concentrations were thus considered in subsequent analysis.

The study of adsorption kinetics is very useful for understanding the involved mechanisms and the design of future large scale adsorption facilities. The mostly used models in fitting kinetic adsorption experiments are the pseudo-first order, pseudo-second order, intra-particle diffusion and Elovich models (Örnek *et al.*, 2007). In order to examine the mechanism of adsorption process such as mass transfer and chemical reaction, a suitable kinetic model is needed to analyze the rate data. Major models (pseudo-first order and pseudo-second order) in the literature have been extensively applied in batch reactors in this study to describe the transport of adsorbates inside the adsorbent particles. All constants were calculated from the intercept and slope of the line obtained from linearized form of models.

The Pseudo-first-order equation 4.5 is a function the capacity of the solid adsorbent relative to the liquid/solid system.

$$log(Qe - Qt) = logQe - (K_{1p} * t)/2.303 \ldots\ldots\ldots\ldots\ldots \textbf{4.5}$$

where q_e and q_t are the amounts of Pb(II) ions sorbed at equilibrium and at time t (mg/g), respectively, and k_1 is the rate constant of pseudo first-order sorption (l/min) and log q_e and $-\frac{K_{1p}}{2.303}$ are the intercept and slope respectively. Fitting the adsorption data and plotting log (qe-qt) vs time, t for the two adsorbents, the following curves were obtained (Figure 4.16a). The value of the adsorption capacity at equilibrium can be calculated by fitting equation 4.5 to the experimental data.

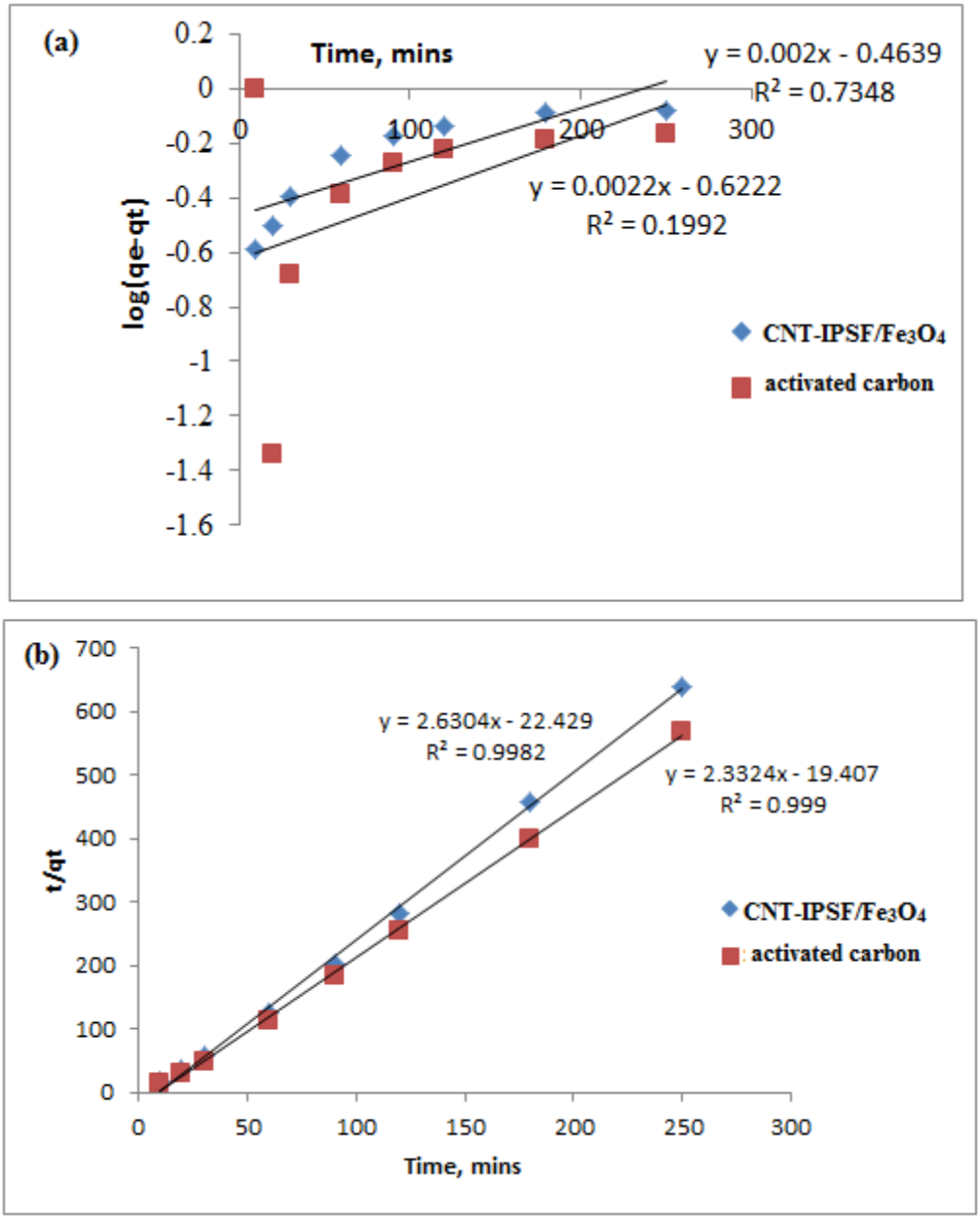

Figure 4. 16 (a) Pseudo-first-order and (b) Pseudo-second-order kinetics for Pb(II) ions on CNT-IPSF/Fe_3O_4 and activated carbon

The values for the pseudo first order kinetics K_1 and R^2 from figure 4.16a and equation 4.5 are indicated in table 4.2.

The linear form of pseudo second order kinetic model is represented by equation 4.6;

$$t/Q_t = 1/K_{2p}Q_e^2 + 1/Q_e t \quad \text{..... 4.6}$$

Figure 4.16b was obtained when t/Q_t vs t was plotted for the two adsorbent types from the adsorption data. The kinetic parameters K_2 and R^2 for pseudo second order from figure 4.16b and equation 4.6 are indicated in table 4.2

Table 4.2 Pseudo-first and Pseudo-second-order kinetics adsorption constants for Pb(II) ions on CNT-IPSF/Fe_3O_4 and activated carbon adsorbents

Kinetics	Parameters	Type of adsorbent	
		CNT-IPSF/Fe_3O_4	Activated carbon
Pseudo 1st order	q_e	0.34	0.24
	$K_{1ρ}$	0.0046	0.005
	R^2	0.7348	0.1992
Pseudo 2nd Order	q_e	0.38	0.43
	$K_{2ρ}$	0.308	0.28
	R^2	0.9982	0.999

The R^2 values for both CNT-IPSF/Fe_3O_4 and activated carbon were greater than 0.99 suggesting adsorption fitted the pseudo second order model through chemisorption that involved sharing of valence forces or exchange of electrons between adsorbent and Pb(II) ions. The pseudo second order model gives the best fit to experimental data from Pb(II) ions adsorptions for the CNT-IPSF/Fe_3O_4 nanocomposites and activated carbon adsorbents studied, which had correlation coefficients of 0.9982 and 0.999 respectively for same initial 2 mg/L Pb(II) ions concentrations.

The amount of adsorbed Pb(II) ions at the equilibrium are similar and consistent with the calculated values. This implies that the pseudo-second-order adsorption mechanism fits the adsorption of Pb^{2+} ions onto nanocomposites adsorbent, and both the adsorbate and adsorbent determine the adsorption process which is controlled by the chemisorption process (Vadivelan and Kumar, 2005).

4.5.3 Isotherm Models for Pb(II) ions Adsorption

4.5.3.1 Initial Pb(II) ions Concentrations

Figure 4.17 shows the adsorption capacities of prepared CNT-IPSF/Fe_3O_4 nanocomposites and standard activated carbon adsorbents at varying initial Pb(II) ions concentrations (2 – 12 mg/L).

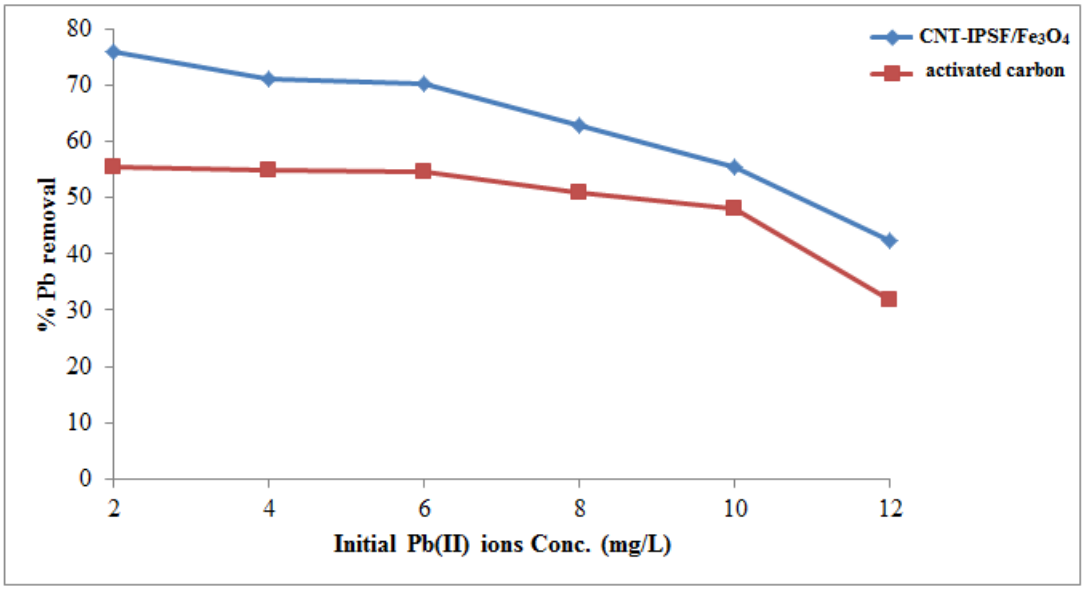

Figure 4. 17 Effect of initial Pb(II) ions concentrations on CNT-IPSF/Fe_3O_4 and activated carbon

Comparison of removal efficiencies showed a gradual decrease from 76 % to 42 % and from 55 % to 31 % for CNT-IPSF/Fe_3O_4 and activated carbon, respectively as the initial Pb^{2+} ions concentration was increased from 2 - 12 mg/L (Figure 4.17). This confirms that the removal efficiency is usually high at lower metal ions concentrations (Fu and Wang, 2011).

4.5.3.2 Isotherm Models for Pb(II) ions Adsorption

In any adsorption process, the adsorption capacity of the adsorbent used influences the removal of impurities from the wastewater (Porjazoska *et al.*, 2015). In such adsorption analysis, the best correlation to the experimental values is determined

followed by the assessment of the isotherm parameters. The Freundlich and Langmuir isotherm were derived from the equilibrium data (Ismail *et al.*, 2013). Langmuir isotherm was explained in linear form equation 4.7;

$$C_e/q_e = 1/q_m.b + C_e/q_m \quad \text{..... } \mathbf{4.7}$$

where C_e is equilibrium concentration of Pb(II) ions solution, q_e is amount of Pb(II) ions adsorbed at equilibrium (mg/g), q_m(mg/g) and b is Langmuir constant. The plot of $\frac{C_e}{q_e}$ against C_e gives straight lines (Figure 4.18a) of slope $1/Q_o$ and intercepts $1/Q_ob$ which were used to calculate Q_e (adsorption efficiency) and b (adsorption energy) as shown in table 4.3

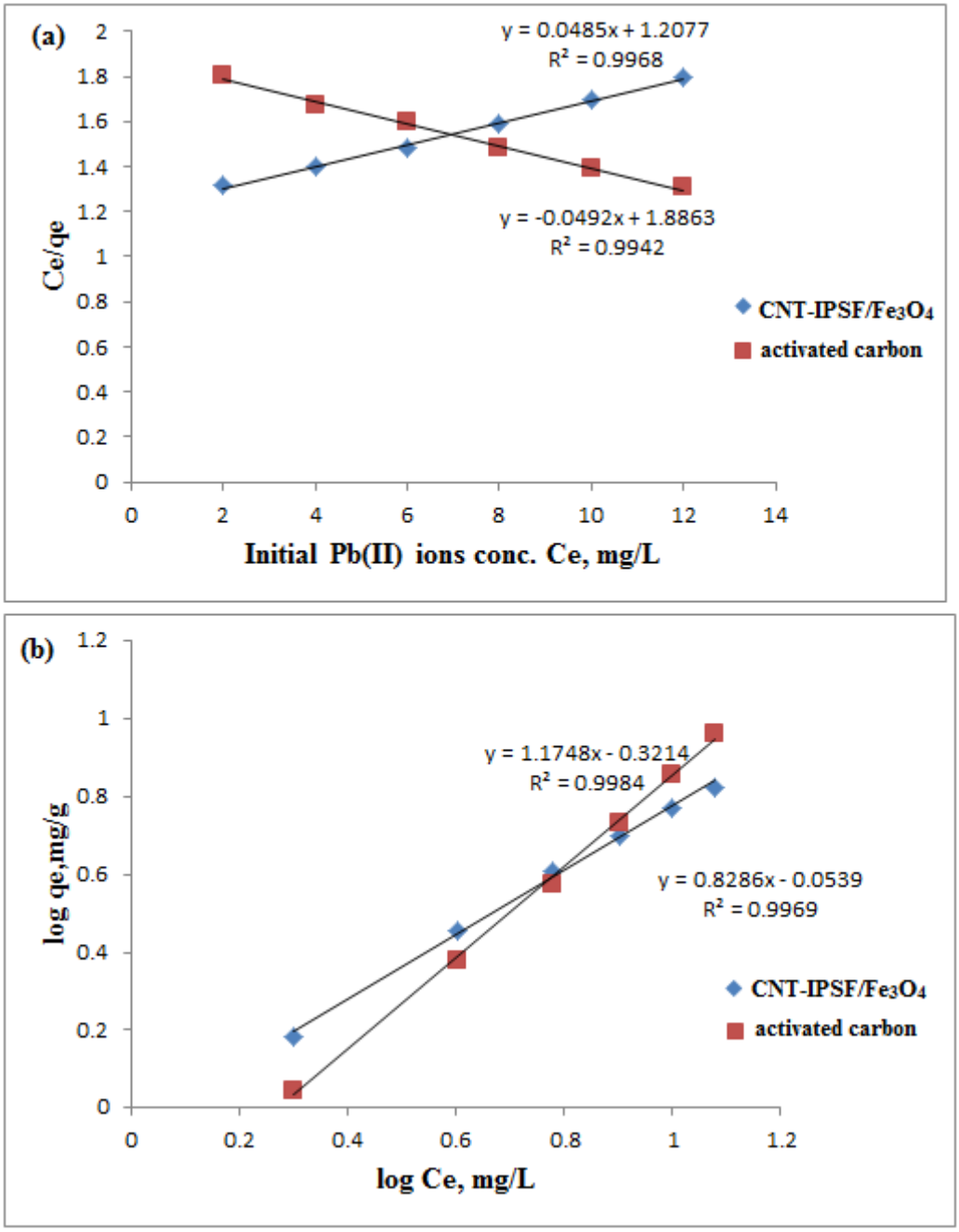

Figure 4. 18 (a) Langmuir and (b) Freundlich isotherms for Pb(II) ions on CNT-IPSF/Fe_3O_4 and activated carbon

The Freundlich isotherm was explained by linear form (Equation 4.8);

$$\log q_e = \log K_f + 1/n \log C_e \quad \text{.....} \mathbf{4.8}$$

where q_e = amount of adsorbed, C_e = equilibrium concentration, K_f = the constant of system and 1/n measures adsorption intensity. The linear plots of log q_e against log C_e

from the adsorption data are shown in figure 4.18b where the values of K_f and 1/n were determined from intercept and slopes.

Accordingly, the R^2 values were above 0.99 (Table 4.3) implying that the Freundlich model fitted the experimental data better than Langmuir model.

Table 4.3 Langmuir and Freundlich adsorption isotherm constant for Pb(II) ions on CNT-IPSF/Fe_3O_4 and activated carbon adsorbents

Isotherms	Parameters	Type of adsorbent	
		CNT-IPSF/Fe_3O_4	Activated carbon
Langmuir	Q_m	20.62	20.33
	b	0.04	0.26
	R^2	0.9968	0.9942
Freundlich	Kf	1.13	2.09
	1/n	0.8286	0.85
	n	1.21	1.24
	R^2	0.9969	0.9984

The calculated dimensionless constant separation factor R_L $\left(\frac{1}{1+bc_o}\right)$ from this study was in the range 0.92 – 0.67 for initial Pb(II) ions concentrations (2 – 12 mg/L) which is less than 1 The R_L values of between 0 and 1confirmed that the adsorption process for Pb(II) ions from aqueous solutions was favourable and suitable (Ngah *et al.*, 2002). The linear form of correlation coefficient value R^2 = 0.9968 (CNT-IPSF/Fe_3O_4) and R^2=0.9942 (activated carbon) for Langmuir isotherm and R^2 = 0.9969 (CNT-IPSF/Fe_3O_4) and R^2=0.9984 (activated carbon) for Freundlich can suggest that both isotherms provide a good result for the adsorption model of Pb(II) ions on the adsorbents.

The linear form of the Langmuir isotherm (Figure 4.18a) indicates that the surface of the CNT-IPSF/Fe_3O_4 nanocomposites is uniform, and all the adsorption sites are equivalent. Freundlich isotherm was chosen to estimate the adsorption intensity of the

adsorbent towards the adsorbate. The magnitude of K_f and n, shows the possibility of an easy separation of heavy metal ions from aqueous solution and a high adsorption capacity respectively. From the Freundlich isotherm model, the Pb(II) ions adsorbed for a unit equilibrium concentration represented by K_f were 1.13 and 2.09 for CNT-IPSF/Fe_3O_4 nanocomposites and activated carbon adsorbents respectively. The K_f value is related to the adsorption intensity. Therefore, the K_f values from this study ($1 < K_f$) confirm that the adsorption capacity was high. The adsorption intensity value for CNT-IPSF/Fe_3O_4 nanocomposites of n=1.21 was $1< n < 10$ representing beneficial adsorption of Pb (II) ions (Zheng *et al.*, 2009).

4.5.4 Effect of Counter Ions on Pb(II) ions Adsorption

4.5.4.1 Effect of Cations

Several divalent cations such as Zn^{2+}, Cu^{2+} and Cd^{2+} present in waste water have been found to interfere with the uptake of Pb(II) ions by adsorbent (Kaewsarn *et al.*, 2001). The effect of these cations on adsorption of Pb(II) ions by CNT-IPSF/Fe_3O_4 nanocomposites was studied and the results are shown in figure 4.19.

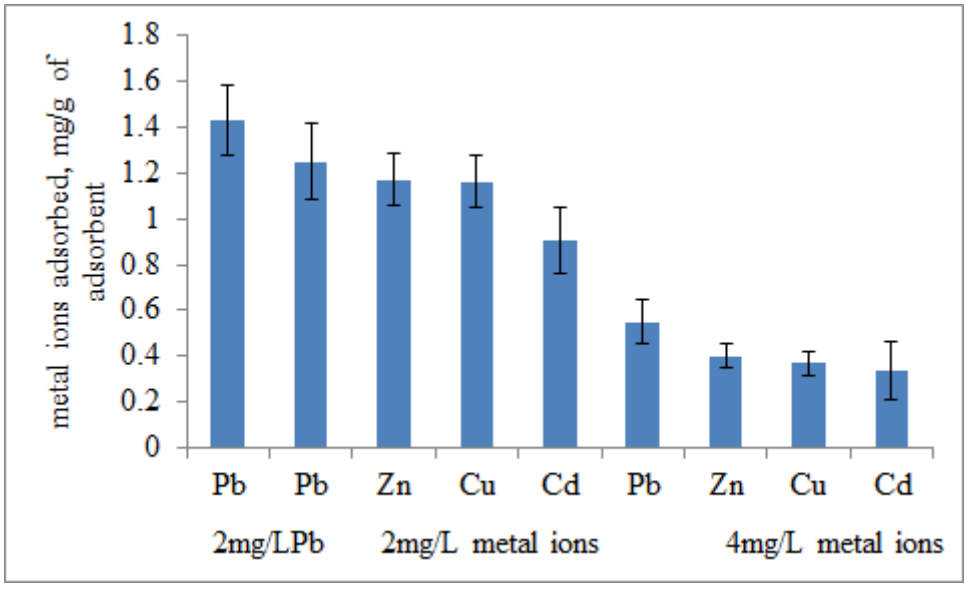

Figure 4. 19 Effect of counter cations on Pb(II) ions adsorption onto CNT-IPSF/Fe_3O_4

The Pb(II) ions concentration was kept constant at 2 mg/L while the concentrations of spiked cations were varied from 2 to 4 mg/L to check their influence on Pb(II) ions adsorption. The adsorption of Pb(II) ions was 1.43 mg/g in the absence of Zn^{2+}, Cu^{2+}, Cd^{2+} ions but dropped to 1.23 and 0.55 mg/g when the solutions were spiked with 2 mg/L and 4 mg/L, respectively of Zn^{2+}, Cu^{2+}, Cd^{2+} ions. This could be due to competition between the Pb(II) ions and counter ions for the same binding sites on the adsorbent. It can also be seen that counter ions (Zn^{2+}, Cu^{2+} or Cd^{2+}) at 4 mg/L concentration greatly reduced Pb(II) ions adsorption as compared to when 2 mg/L spiked concentrations were used. This is because adsorption is concentration dependent and it decreases with increase in concentration (Kim *et al.*, 2002).

Control experiment involved agitating 2 mg/L batch solutions of Pb^{2+}, Zn^{2+},Cu^{2+} and Cd^{2+} ions solutions with 0.05 g of CNT-IPSF/Fe_3O_4 and activated carbon adsorbents separately and determining adsorption of the metal ions (Figure 4.20).

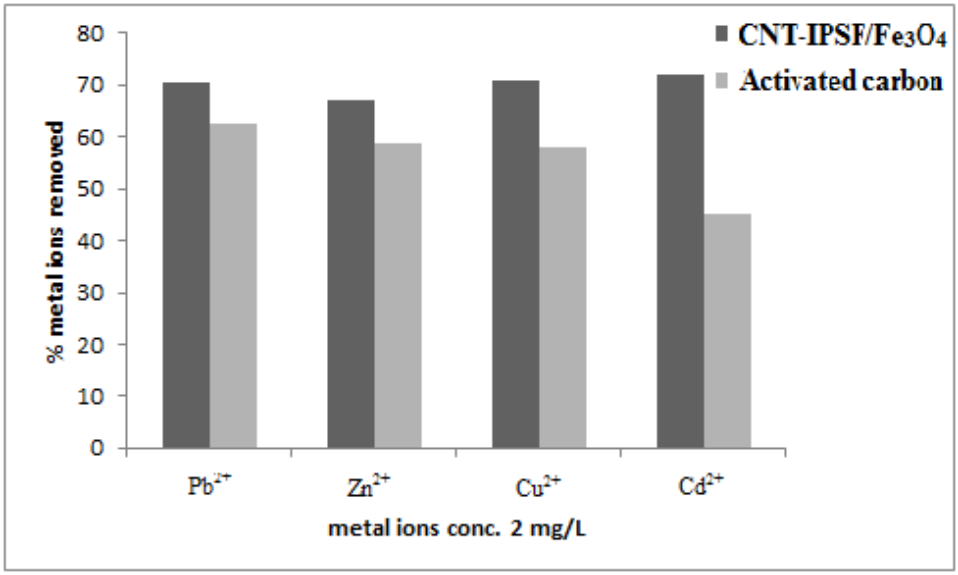

Figure 4. 20 Effect of 2 mg/L cations adsorption onto CNT-IPSF/Fe_3O_4 and activated carbon

It can be seen that the CNT-IPSF/Fe_3O_4 nanocomposites had higher removal efficiency (≥70 %) for all cations studied than activated carbon adsorbent (p=0.005). The fabricated nanocomposite was least affected by any of the counter cations hence could be applied in removal of cationic pollutants from aqueous solutions.

4.5.4.2 Effect of Anions and anionic Ligands

The effect of nitrate ions, ammonia and EDTA ligands on lead (II) ions removal was also studied as shown in figure 4.21.

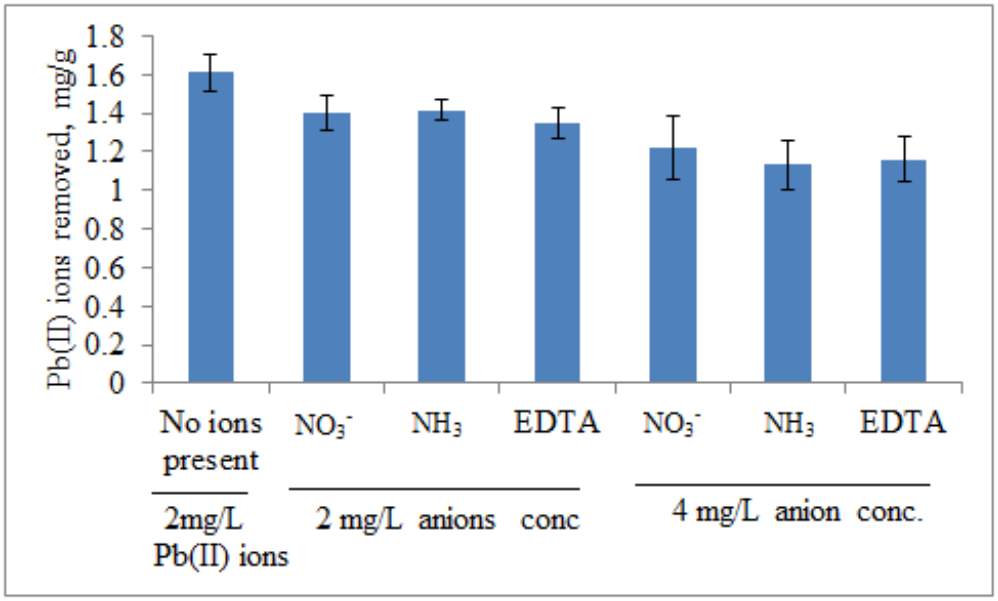

Figure 4. 21 Effect of anions and ligands for Pb(II) ions adsorption onto CNT-IPSF/Fe_3O_4

As observed in figure 4.21, the absence of nitrate ions, ammonia and EDTA led to Pb(II) ions adsorption of 1.61 mg/g. The introduction of 2 mg/L anion/ligands into the batch solutions had less effect on the removal of Pb(II) ions. This could be due to their ability to form soluble compounds with Pb(II) ions thus not inhibiting Pb(II) ions adsorption. However, when 4 mg/L of nitrate ions, ammonia and EDTA were introduced, the Pb(II) ions removal dropped to 1.22, 1.13 and 1.15 mg/g respectively.

This was due to the fact that Pb(II) ions combine strongly with nitrate ions, ammonia and EDTA at higher concentrations forming complexes with high stabilities thus limiting Pb(II) ions adsorption onto the nanocomposites (Deng *et al.*, 2007).

When concentrations of NO_3^- ions increase, the ionic strength is increased. At higher ionic strength, the adsorption of lead(II) ions onto the adsorbent is decreased due to combination of the anion with Pb(II) ions forming respective compounds. The nitrate ions also limits adsorption of lead(II) ions by pairing their charges thus reducing the binding of lead (II) ions onto the adsorbent surface (Sheela and Nayaka, 2012).

Comparison of Pb(II) ions removal by both prepared CNT-IPSF/Fe_3O_4 and standard activated carbon adsorbents revealed that EDTA reduces Pb(II) ions adsorption onto the adsorbents by similar percentage margins of 48.14 and 46.24 % respectively (Figure 4.22). This confirms that the ability of the CNT-IPSF/Fe_3O_4 nanocomposites for Pb(II) ions removal from aqueous solution is not largely affected by such anion/ligands in the solutions.

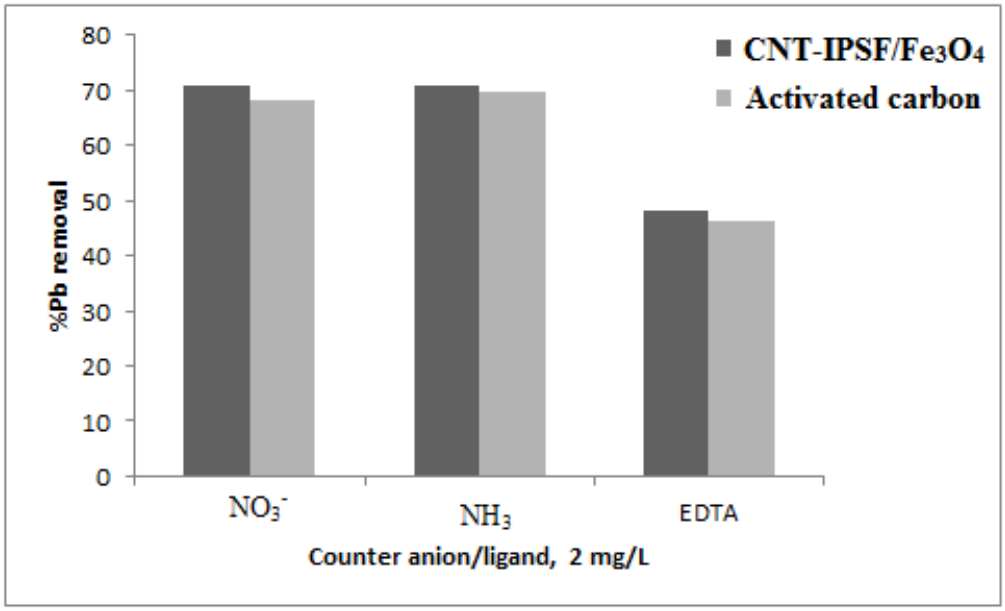

Figure 4. 22 Effect of 1M anion/ligands on Pb(II) ions adsorption onto CNT-IPSF/Fe_3O_4 and activated carbon

4.6 Removal of Phenanthrenes Using CNT-IPSF/Fe_3O_4 Nanocomposites

4.6.1 Optimization of Adsorption Parameters Using Phenathrene

4.6.1.1 Effect of Adsorbent Dose on Phenanthrenes Adsorption

The adsorption of phenanthrenes on the nanocomposites was studied by varying the nanocomposites mass from 2–20 mg in 20 ml of 15 and 20 µg/L initial phenanthrene concentrations (Figure 4.23). The phenanthrenes removal by the nanocomposite adsorbent increased sharply from adsorbent mass of 2 to 4 mg but rate decreased slightly when 20 mg was used.

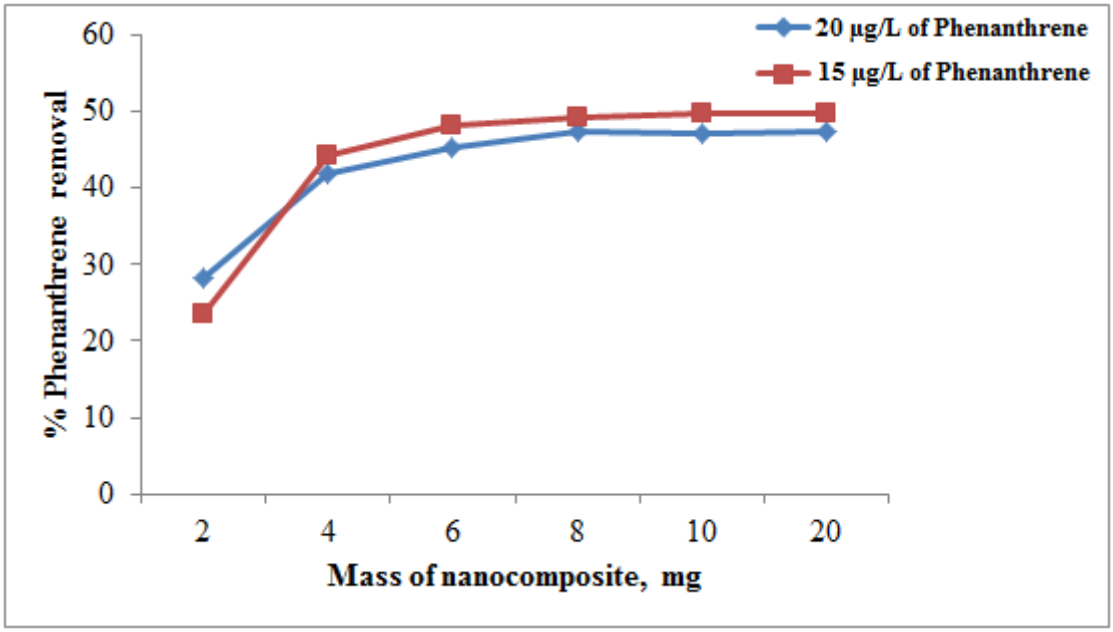

Figure 4. 23 Effect of nanocomposite dose on phenanthrenes adsorption

The percentage phenanthrenes removal increased from 28 – 45 % and 23 – 48 % for 20 and 15 µg/L initial phenanthene concentrations, respectively. The phenanthrenes adsorption was higher at the beginning due to higher adsorption of its molecules to the available adsorption sites (Yang and Xing, 2010). The higher adsorption could be attributed to an increase in electrostatic interactions between surface atoms and phenanthrenes molecules (Poater *et al.*, 2006). This was followed by a steady decrease in adsorption due exhaustion of the available adsorption sites. Therefore, further experiments were conducted at 6 mg optimum mass.

4.6.1.2 Effect of Contact Time on Phenanthrene Adsorption

The effect of contact time on the adsorption of phenanthrenes was investigated for 60 minutes using 15 and 20 µg/L of phenanthrenes solutions. The results (Figure 4.24) show a sharp increase in phenanthrenes removal between 5 and 20 minutes for 15 and 20 µg/L phenanthrene concentrations. This translated into an increase from 37.8-49.5 % and 30.7-41.7 % for 15 and 20 µg/L phenanthrenes concentrations, respectively.

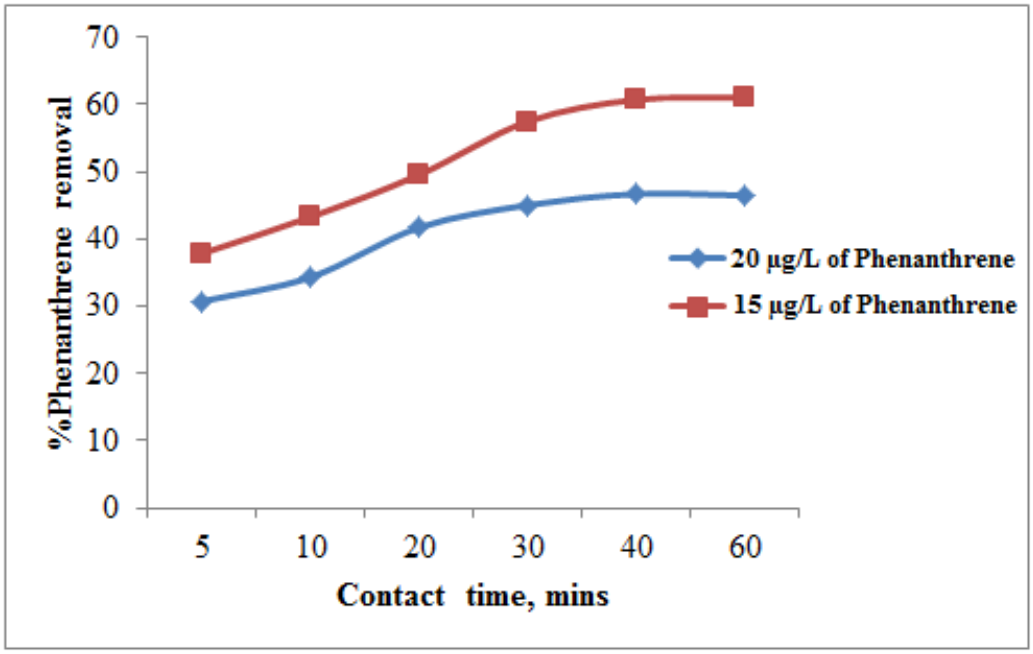

Figure 4. 24 Effect of contact time on phenanthrenes adsorption

The sharp increase could be due to the fact that more vacant surface sites were available for adsorption of phenanthrenes at initial stages which ultimately reduced with increase in contact time, leading to lower removal (Paria, 2008). Adsorption equilibrium was attained approximately within 40 minutes of contact time. The high affinities for adsorption of the phenanthrenes onto the adsorbent were dominated by π-π interactions onto the flat adsorbent surface. In contrast, limited π-π interaction led to the decreased adsorption due to unusually altered adsorption sites of adsorbent surface during the adsorption process (Wang *et al.*, 2014).

4.6.1.3 Effect of pH on Phenanthrenes Adsorption

The effects of solution pH on phenanthrenes removal by the nanocomposite adsorbent were compared for 15 and 20 µg/L phenanthrenes concentrations as in figure 4.25.

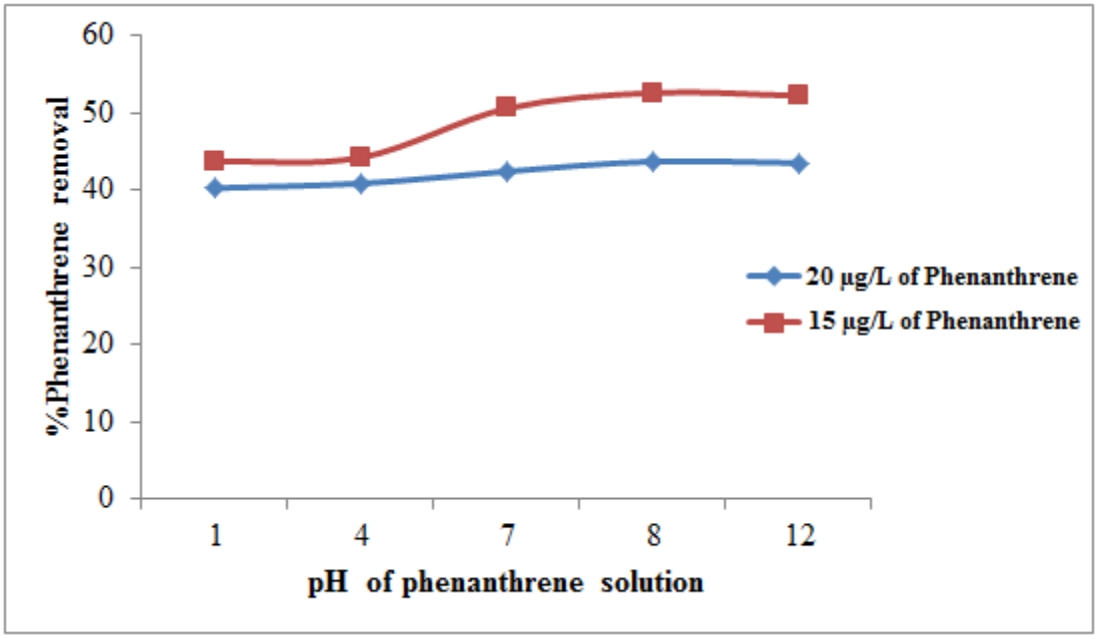

Figure 4. 25 Effect of pH on phenanthrenes adsorption

Phenanthrenes adsorption gradually increased as the pH increased from 4 to 8 for both initial phenanthrenes concentration. The removal of phenanthrenes was due to the possible π-π interactions between the nanocomposite adsorbent and phenanthrenes molecules (Gotovac *et al.*, 2006). Orange peel has also been used previously for the removal of naphthalene but the adsorption capacity was quiet low (Owabor *et al.*, 2012). Hashemian *et al.* (2013) reported adsorption of azo dyes from aqueous solution using activated carbon derived from orange peel (Hashemian *et al.*, 2013).

4.6.2 Kinetics Model for Phenanthrene Adsorption

4.6.2.1 Effect of Contact Time on Phenanthrene Adsorption Kinetics

This study showed that phenanthrenes sorption was time dependent and increased with increasing contact time (Figure 4.26). This was due to higher initial availability of the phenanthrenes adsorbates in solution which led to higher phenanthrenes removal. It was noticed that the change in contact time was comparable for the two concentrations with no significant difference ($p = 0.05$).

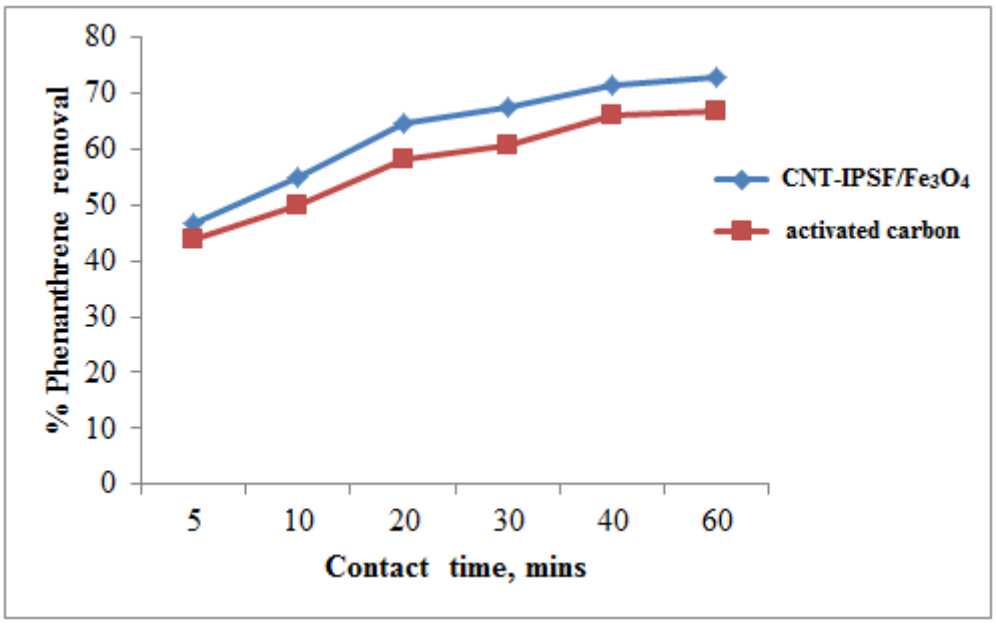

Figure 4. 26 Effect of time on phenanthrenes adsorption by CNT-IPSF/Fe_3O_4 and activated carbon

However, the CNT-IPSF/Fe_3O_4 nanocomposite gave better percentage removal reaching maximum of 72 % after 60 minutes, which indicated that its adsorption sites have higher affinity for phenanthrene molecules.

4.6.2.2 Kinetic Models for Phenanthrenes Adsorption

Two kinetic models were studied to describe the kinetics for the adsorption of phenanthrenes namely the pseudo-first-order and pseudo-second-order (Dharmambal *et al.*, 2015). Kinetic equations were applied to distinguish adsorption capacities of solids as per pseudo-first-order equation 4.5;

$$log(Qe - Qt) = logQe - (K_{1p} * t)/2.303 \quad \text{..... } \mathbf{4.5}$$

Fitting and plotting log (qe-qt) vs time, t from the adsorption data for CNT-IPSF/Fe_3O_4 and activated carbon, the following curves (Figure 4.27a) were obtained.

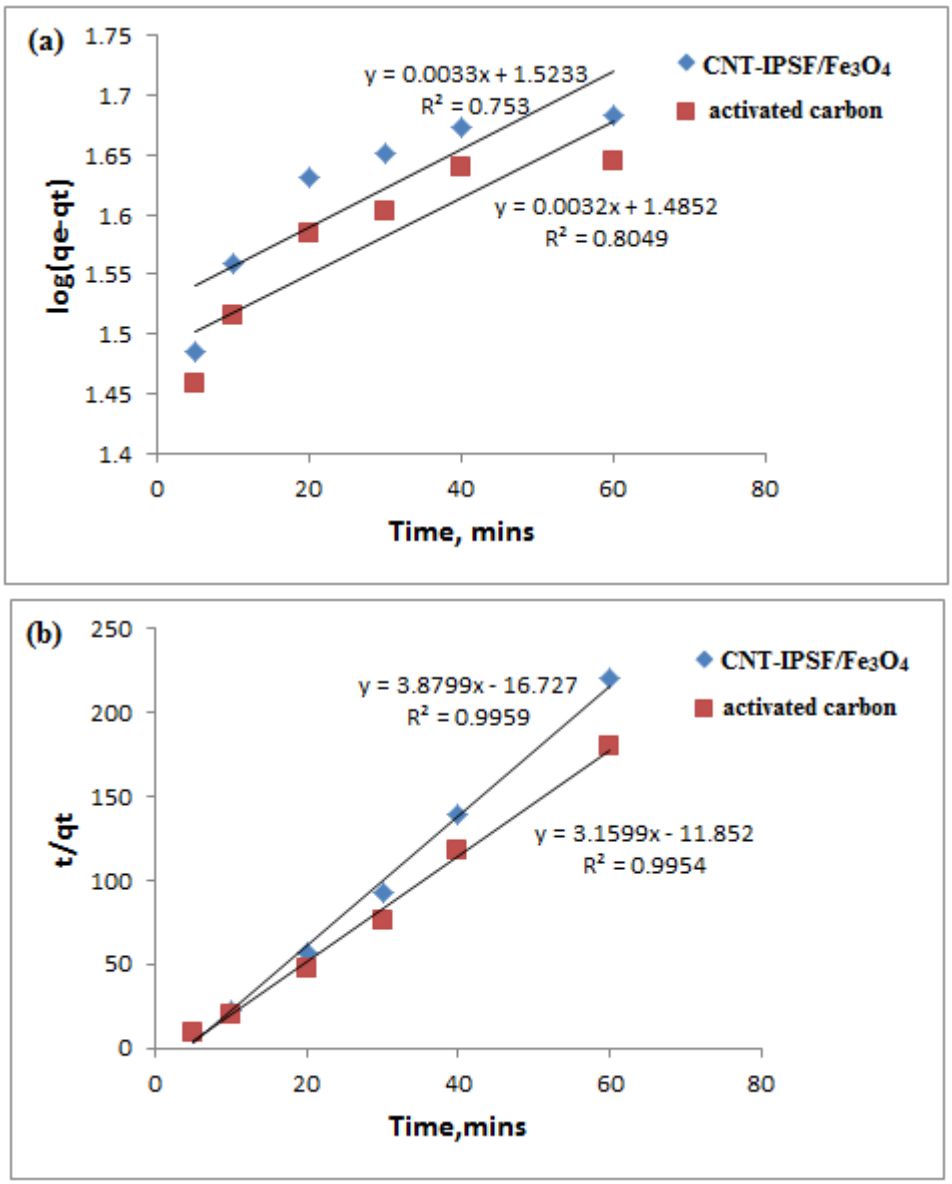

Figure 4. 27 (a) Pseudo-first-order and (b) Pseudo-second-order kinetics for phenanthrenes on CNT-IPSF/Fe_3O_4 and activated carbon

The values for kinetic parameters K_1 and R^2 for pseudo first order are indicated in table 4.4. The experimental data was also fitted to pseudo-second-order kinetic model as in equation 4.6;

$$t/Q_t = 1/K_{2p}Q_e^2 + 1/Q_e t \ldots\ldots\ldots\ldots\ldots\ldots\ldots\ldots \textbf{4.6}$$

When t/ Qt vs time was plotted for the adsorption data, the following curves (Figure 4. 27b) were obtained. The values for parameters K_2 and R^2 are shown in table 4.4.

The R^2 values for both the adsorbents are greater than 0.9 suggesting adsorption followed pseudo second order model.

Table 4.4 Pseudo-first and second-order adsorption constants for phenanthrene

Kinetics	Parameters	Type of adsorbent	
		CNT-IPSF/Fe_3O_4	activated carbon
Pseudo 1st order	q_e	33.37	30.56
	K_{1p}	0.0076	0.0074
	R^2	0.753	0.8049
Pseudo 2nd Order	q_e	0.26	0.32
	K_{2p}	0.89	0.84
	R^2	0.9959	0.9954

The pseudo-second-order model gave the best fit to phenanthrenes adsorption data for both the CNT-IPSF/Fe_3O_4 and activated carbon adsorbents with the highest correlation coefficient values of 0.9959 and 0.9954, respectively. This implied that the rate of occupation of adsorption sites is equivalent to the square the number of unoccupied sites (Lasheen *et al.*, 2012). A similar observation was made for Pb(II) ions adsorption kinetics (Table 4.2).

4.6.3 Isotherm Model for Phenanthrenes Adsorption

4.6.3.1 Initial Phenanthrenes Concentration

The adsorption capacities of the two adsorbents on phenanthrenes removal was investigated at different initial concentrations of phenathrene (1–10 µg/L) as shown in figure 4.28. Maximum adsorption capacities were realized at 6 and 8 µg/L phenanthrenes concentrations for CNT-IPSF/Fe_3O_4 and activated carbon adsorbents respectively.

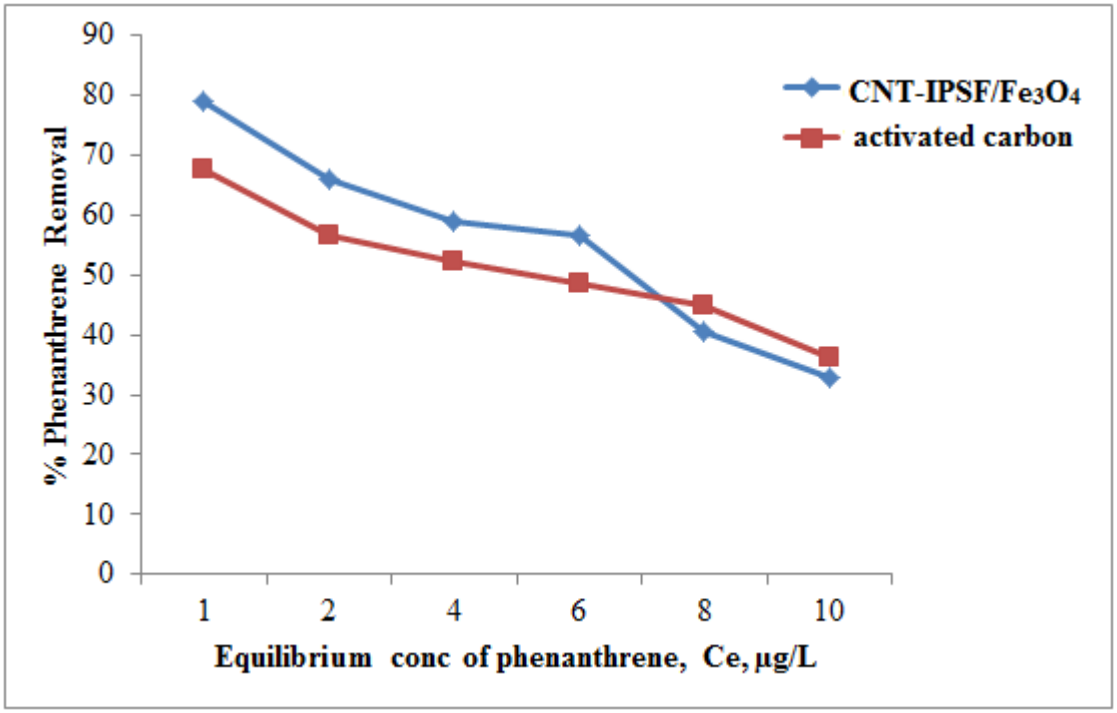

Figure 4. 28 Effect of initial phenanthrenes concentrations on CNT-IPSF/Fe_3O_4 and activated carbon

Maximum adsorption capacities were recorded at 6 and 8 µg/L initial phenanthrenes concentrations for CNT-IPSF/Fe_3O_4 and activated carbon adsorbents, respectively. The overall relationship for phenanthrenes removal was inverse to the initial phenanthrenes concentration where it decreased from 79.1 - 32.7 % and 69.7 - 36.1 % for CNT-IPSF/Fe_3O_4 and activated carbon adsorbents respectively as the initial phenanthrene concentrations increased from 1-10 µg/L. Higher removal efficiencies were observed at lower phenanthrene concentrations which is similar to other studies (Yang *et al.*, 2005).

4.6.3.2 Isotherm Models

A given form of the sorption isotherm can provide information on the chemical and physical properties of the adsorbate material and on how the adsorption process proceeds over a given surface (Ranke, 2002). Based on the nature of the adsorbate and

its interaction with adsorbent surface, two kinds of isotherms can be distinguished. The linear form for Langmuir isotherm was applied as per equation 4.7;

$$C_e/q_e = 1/q_m.b + C_e/q_m \quad \text{.....} \mathbf{4.7}$$

The plot of $\frac{C_e}{Q_e}$ against C_e gave a straight line (Figure 4.29a) which was used to determine Q_e (adsorption efficiency) and b (adsorption energy) as shown in table 4.5.

The linear form of equation 4.8 for Freundlich Isotherm was explained by

$$\log q_e = \log K_f + \frac{1}{n}\log C_e \quad \text{.....} \mathbf{4.8}$$

The linear plots of log q_e against log C_e from the adsorption data are shown in figure 4.29b.

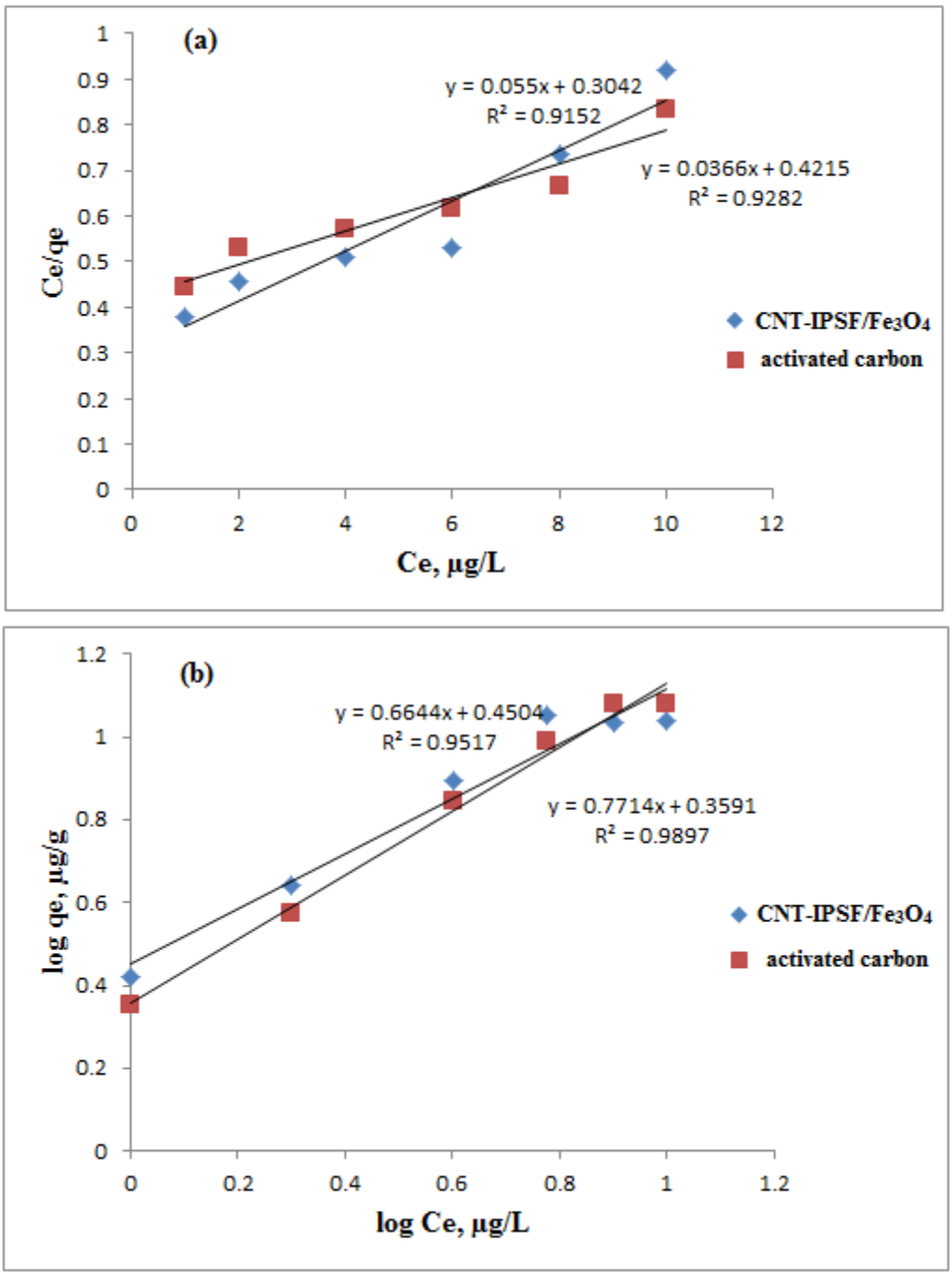

Figure 4. 29 (a) Langmuir and (b) Freundlich adsorption isotherms for phenanthrenes on CNT-IPSF/Fe_3O_4 and activated carbon

According to the R^2 for each adsorbent in table 4.5, the data gave best-fit for Freundlich isotherm models with correlation coefficient R^2 values greater than 0.95.

Table 4.5 Langmuir and Freundlich isotherm adsorption constants for Phenanthrenes on CNT-IPSF/Fe_3O_4 and activated carbon

Isotherms	Parameters	Type of adsorbent	
		CNT-IPSF/Fe_3O_4	activated carbon
Langmuir	Q_m	29.47	28.329
	b	0.1808	0.0868
	R^2	0.9152	0.9282
Freundlich	Kf	2.8210	2.2861
	1/n	0.6644	0.7714
	n	1.5051	1.2963
	R^2	0.9517	0.9897

The intensity of adsorption (b) is an indication of the bond energies between phenanthrene and adsorbent, and the possibility of physisorption is predictable. Although both isotherms described the adsorption process well, however, Freundlich isotherm for each adsorbent fitted better with higher correlation coefficient (>0.95) in table 4.5. This is further supported by the adsorption capacity K_f values of 2.8 and 2.3 for the CNT-IPSF/Fe_3O_4 and activated carbon adsorbents respectively. The values of n=1.5 is greater than 1, indicating the physisorption is much more possible. High value of n for adsorption showed a weak bond hence representing beneficial adsorption of phenanthrenes by CNT-IPSF/Fe_3O_4 nanocomposite (Zheng *et al.*, 2009).

4.6.4 Effect of Selected PAHs on Phenanthrenes Adsorption

Polycyclic aromatic hydrocarbons with comparable molecular weights to phenanthrenes such as naphthalene and anthracene from oil spills are major components of wastewater from industries (Tam *et al.*, 2001). Figure 4.30 shows the adsorption capacities of the fabricated CNT-IPSF/Fe_3O_4 nanocomposite for phenanthrenes and similar PAHs.

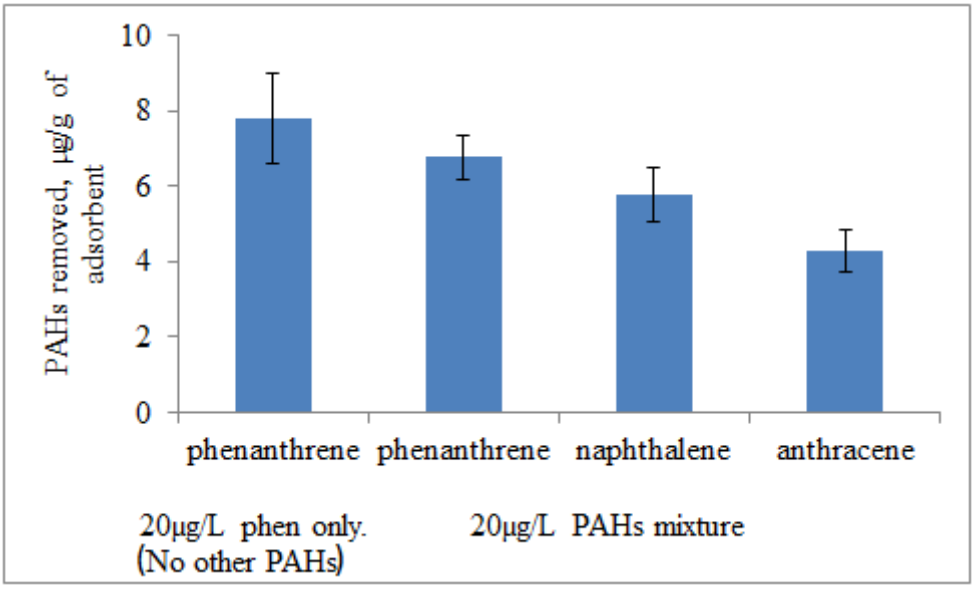

Figure 4. 30 Effect of selected PAHs on phenanthrenes adsorption onto CNT-IPSF/Fe_3O_4

The phenanthrenes concentration with and without selected PAHs was kept constant at 20 µg/L to check their influence on phenanthrenes adsorption. The adsorption of phenanthrenes in the absence of naphthalene and anthracene was 7.8 µg/g. However in presence of selected PAHs, the removal of phenanthrenes dropped to 6.8 µg/g while naphthalene and anthracene removal was 5.8 and 4.3 µg/g respectively. This could be due to competition of the PAHs for the same binding sites on the adsorbent (Kim *et al.*, 2002).

When CNT-IPSF/Fe_3O_4 and activated carbon adsorbents were separately used for phenanthrenes adsorptions in the control experiment, their % removal capacities are as shown in figure 4.31.

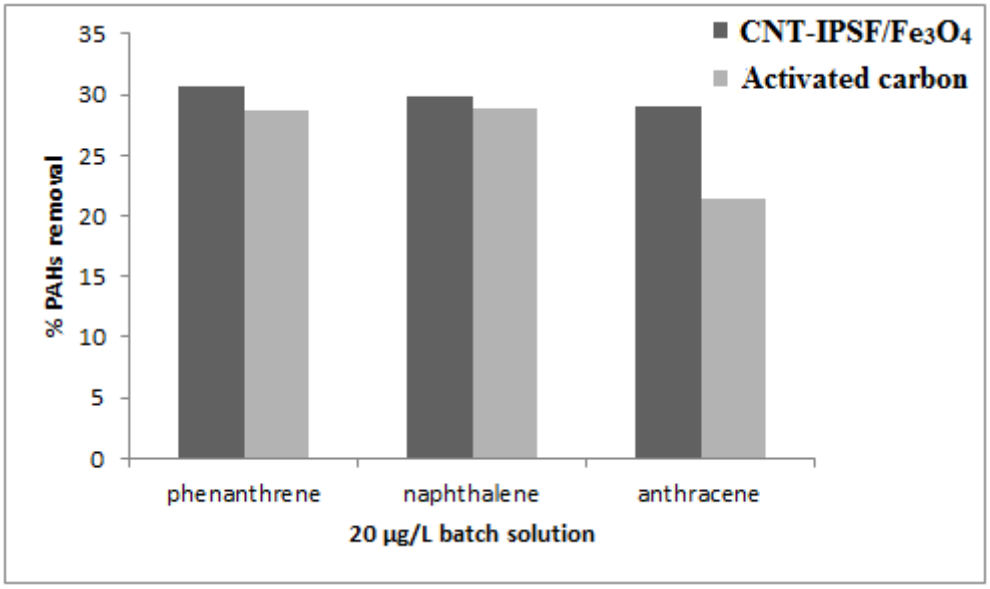

Figure 4. 31 Effect of 20 µg/L PAHs adsorption onto CNT-IPSF/Fe_3O_4 and activated carbon

The CNT-IPSF/Fe_3O_4 nanocomposites had higher removal efficiency ($p=0.005$) than activated carbon adsorbent for the PAHs studied. The removal efficiency for the prepared nanocomposites was less affected by the selected PAHs hence suitable.

Table 4.6 compares the adsorption capacity of the fabricated CNT-IPSF/Fe_3O_4 nanocomposites with other Fe_3O_4 based adsorbents.

Table 4.6 Adsorption capacities of other Fe_3O_4 based adsorbents compared with CNT-IPSF/Fe_3O_4 nanocomposites

Adsorbent	**Adsorption capacity (mg/g)**		
	Pb^{2+} ions	**Phenanthrenes**	**Reference**
Silica coated magnetite NPs	17.65	-	(Mahdavi *et al.*, 2013a)
Carboxylic acid coated magnetite NPs	6.6	-	(Atieh *et al.*, 2011)
Rice straw/Fe_3O_4	19.45	-	(Khandanlou *et al.*, 2015)
Activated carbon	20.33	28.33	Commercial adsorbent
CNT-IPSF/Fe_3O_4 nanocomposites	20.62	29.47	**Present work**

The fabricated CNT-IPSF/Fe_3O_4 nanocomposites from this study had higher adsorption abilities than the other adsorbents showing that it was more efficient and the possibility of its application on large scale could be viable.

4.7 Removal of Pb(II) ions and Phenanthrenes from Wastewater

4.7.1 Removal of Pb(II) ions from Wastewater

Contamination of water due to a wide range of toxic heavy metals and aromatic molecules is a serious environmental problem owing to their potential human toxicity. There is urgent need to improve on technologies that can remove such toxic pollutants from wastewaters. Recently, adsorption on polymeric adsorbent is becoming more popular method for the removal of pollutants from the wastewater. Figure 4.32 compares the removal efficiencies of fabricated CNT-IPSF/Fe_3O_4 nanocomposites and the standard activated carbon for Pb(II) ions from wastewater.

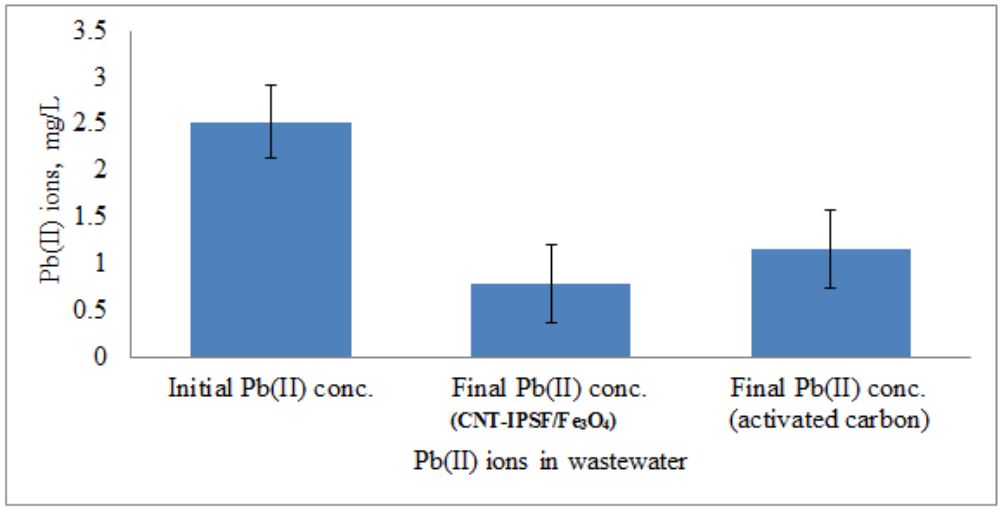

Figure 4. 32 Pb(II) ions removal from wastewater by CNT-IPSF/Fe_3O_4 and activated carbon

The prepared CNT-IPSF/Fe_3O_4 nanomposites and standard activated carbon adsorbents reduced Pb(II) ions from initial concentration of 2.53 mg/L to 0.79 and

1.16 mg/L which translates to adsorption of 1.74 and 1.37 mg/L, respectively. The removal efficiency for CNT-IPSF/Fe_3O_4 nanomposites and standard activated carbon adsorbents was determined as 69 % and 54 %, respectively. This implies that the surface of CNT-IPSF/Fe_3O_4 nanocomposite has higher affinity for Pb^{2+} ions than activated carbon adsorbent (Tofighy and Mohammadi, 2011). Modified nano-alumina with DNPH was favorable and useful for the removal of metal ions, and the high adsorption capacity makes it a good promising candidate material for Pb(II),Cr(III) and Cd(II) removal (Afkhami *et al.*, 2010).

4.7.2 Removal of Phenanthrenes from Wastewater

The removal of phenanthrenes from polluted waters containing other PAHs was tested on the CNT-IPSF/Fe_3O_4 nanocomposites and the results compared to the standard activated carbon (Figure 4.33).

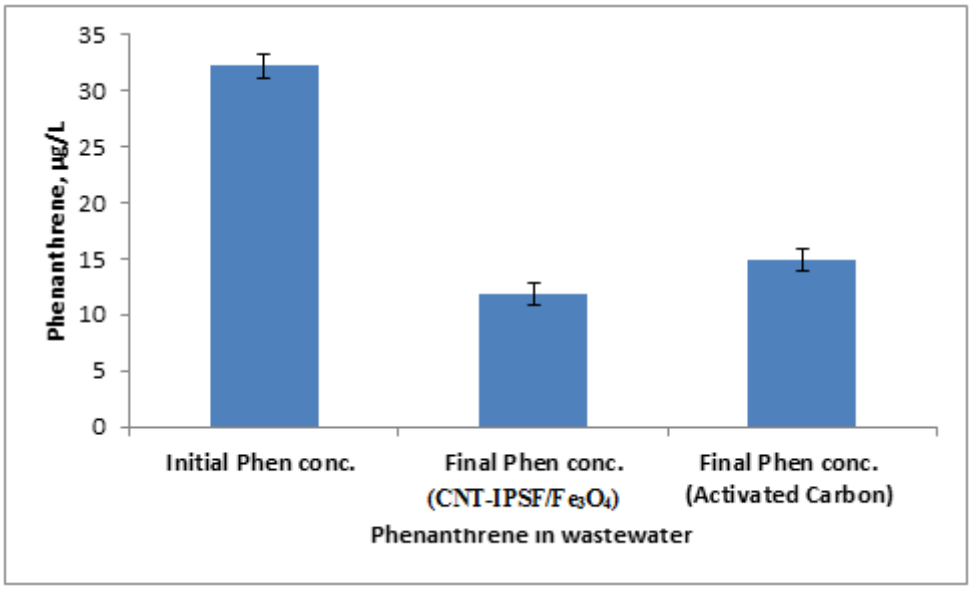

Figure 4. 33 Phenanthrene removal from wastewater by commercial activated carbon and CNT-IPSF/Fe_3O_4

The activated carbon reduced initial phenanthrenes concentrations from 32.2 to 14.8 µg/L while the CNT-IPSF/Fe_3O_4 nanocomposites reduced initial phenanthrenes concentrations to 11.82 µg/L. The phenanthrenes adsorption by activated carbon and

CNT-IPSF/Fe_3O_4 nanocomposite were 17.4 and 20.38 µg/g which translated into about 53 % and 63 % removals, respectively.

This implies that the prepared CNT-IPSF/Fe_3O_4 nanocomposites exhibited good adsorption ability for the recovery of low phenanthrenes concentrations from wastewater samples as demonstrated from its 1/n = 0.66 which is less than unity and n = 1.5 which is greater than one indicating physisorption (Table 4.5). This contribution arise due to the formation of weak bond from π - π electron interaction of the nanocomposites surface with phenanthrene molecules which represents beneficial adsorption (Ahmaruzzaman, 2010). Since these molecules are not chemically bonded to the adsorbent surface from their Freundlich isotherm model (R^2=0.9517), the aromatic core of the adsorbed phenanthrene molecules will exhibit pπ–pπ interactions with the adsorbent surface (Pandey *et al.*, 2011) hence its application on large scale in industry. A similar study found that more than 45% of 3-ring PAHs were removed from sludge by METIX-AC and during ELECSTAB process were quiet good with approximately 62% of 3-ring PAHs removal (Zheng *et al.*, 2007).

4.8 Desorption Studies on CNT-IPSF/Fe_3O_4 Nanocomposites

4.8.1 Desorption Studies Using Pb(II) ions

Common eluents such as sodium carbonate, potassium cyanide, EDTA, nitric acid, sulphuric acid and hydrochloric acid have been employed in the recovery of pollutants from the adsorbents (Mishra, 2014). Recent desorption studies have indicated HNO_3 and Na_2EDTA are more efficient desorption solvents in the recovery of Pb(II) ions (Tarigh and Shemirani, 2013). The desorption of Pb(II) ions from the CNT-IPSF/Fe_3O_4 nanocomposites was investigated using de-ionized water, 0.1M HNO_3 and 0.1M EDTA so as to identify the most suitable desorption solvent for removal of

the adsorbed Pb(II) ions from the nanocomposites. Deionized water was chosen because it is a component of the sample matrix while nitric acid and EDTA are known to form soluble compounds with Pb(II) ions. The efficiency of selected desorption solvents in removal of the adsorbed Pb(II) ions from the surfaces of the CNT-IPSF/Fe_3O_4 nanocomposites and standard activated carbon adsorbents is shown in figure 4.34.

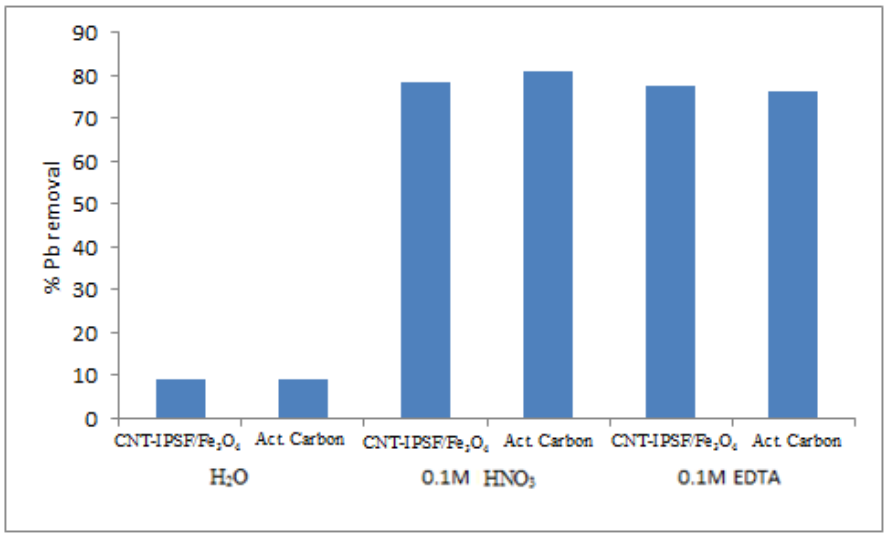

Figure 4. 34 Efficiencies of Pb(II) ions from CNT-IPSF/Fe_3O_4 and activated carbon

It is evident that HNO_3 and EDTA are better desorption solvents and that they were able to recover 78 % and 77 %, respectively of Pb(II) ions adsorbed from the surface of the prepared CNT-IPSF/Fe_3O_4 nanocomposites. However, de-ionized water showed recovery of about 9 % from the prepared nanocomposites. The high desorption ability of EDTA from these desorption studies could arise from the formation constant ($K'_f = 3.55\times10^{11}$) of the Pb(II)-EDTA complex (Martins *et al.*, 2006). EDTA is also a hexadentate ligand with chelating property that enables its binding to Pb(II) ions. The Pb(II) ions in the bound Pb - EDTA complex remain in solution although the ions have reduced reactivity.

This is supported by initial studies done to investigate Pb(II) ions adsorption from aqueous solutions in presence of EDTA ligand which found out that Pb(II) ions form soluble complexes with EDTA and thus readily provides Pb(II) ions for adsorptions onto the CNT-IPSF/Fe_3O_4 nanocomposites (Figure 4.22). However, HNO_3 acid was chosen for regeneration studies since Pb-EDTA complexes shows limited adsorption at various pH values (Bradl, 2004). Desorption study reveals that Pb(II) ions adsorbed could be desorbed using HNO_3 due to breakage of complexes formed on the sorbent surface.

4.8.2 Desorption Studies Using Phenanthrene

The optimum choice of organic solvents for desorption is dictated by solute polarity i.e. a less polar organic solvent is needed to attain the maximal efficiency when working with less polar solutes. Desorption studies were done to investigate the strengths of the desorption solvents in removal of adsorbed phenanthrenes from the nanocomposites. Figure 4.35 shows desorption efficiencies of methanol, n-hexane and acetone for phenanthrenes removal from CNT-IPSF/Fe_3O_4 nanocomposites and activated carbon adsorbents in which the strength of the studied desorption solvents was in the order: acetone > hexane > methanol. This trend can be explained on the basis of non-polarity, except for methanol which is most polar with polarity index value of 5.1 (Okoli *et al.*, 2015) thus exhibiting least desorption ability. This observation might likely be linked to the interactions of different functional groups with the phenanthrenes molecules. Acetone had the highest percentage removal ($p=0.05$) for phenanthrenes at 79 % and 75 % from the prepared CNT-IPSF/Fe_3O_4 nanocomposites and standard activated carbon adsorbents, respectively. Hence,

acetone which is ketone (R-CO-R) will likely interact more with the adsorbate than methanol which is an alcohol (R-OH).

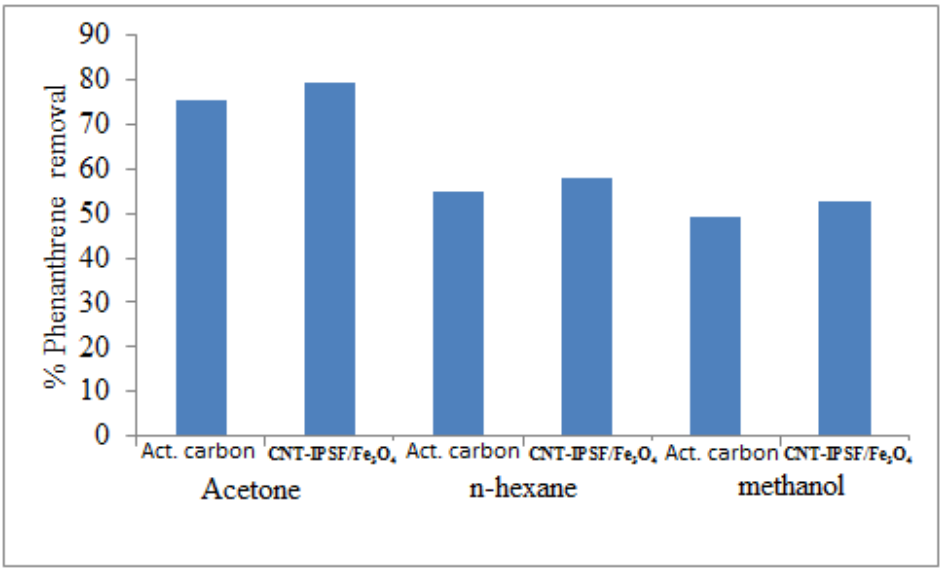

Figure 4. 35 Removal efficiencies of phenanthrenes from CNT-IPSF/Fe_3O_4 and commercial activated carbon different desorption solvents

4.9 Regeneration Studies on CNT-IPSF/Fe_3O_4 Nanocomposites

4.9.1 Regeneration Using Pb(II) ions

This desorption test, if reliable, could positively impact the subsequent utilization of the nanocomposites, thus providing higher chances for its reusability. The Pb(II) ions initially adsorbed onto the prepared CNT-IPSF/Fe_3O_4 nanocomposites were determined at initial Pb(II) ions concentrations of 1, 2, 4, 6, 8 and 10 mg/L while the % desorption efficiencies was determined after three adsorption desorption cycles using HNO_3 as per equation 4.9 and figure 4.36;

$$\% \text{ Desorption Efficiency} = \frac{\text{Amount of metal ions desorbed}}{\text{Amount of metal ions adsorbed}} \text{ x } 100 \quad \ldots\ldots\ldots\ldots\ldots\ldots \textbf{4.9}$$

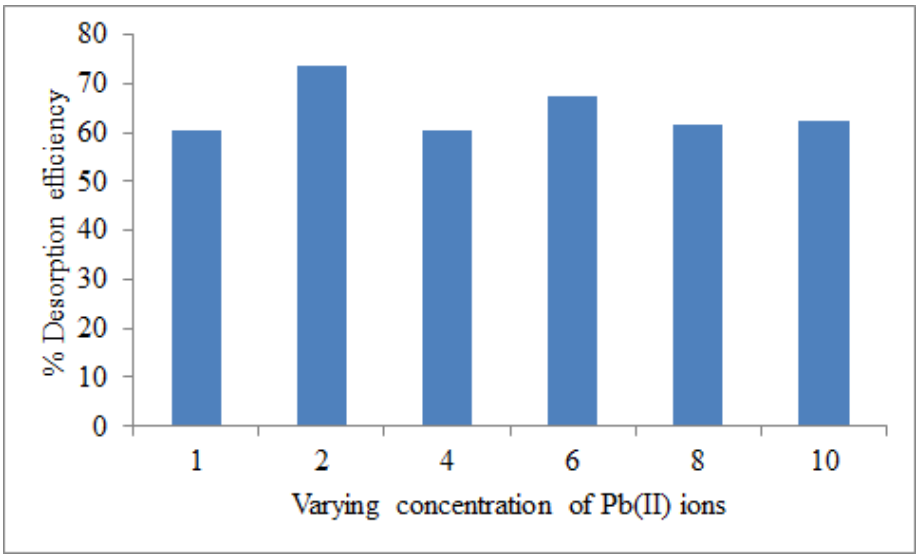

Figure 4. 36 Investigating reusability of CNT-IPSF/Fe_3O_4 using Pb(II) ions

There was a positive trend in the removal of Pb(II) ions from the adsorbent using HNO_3 at 1-10 mg/L initial Pb(II) ions. The desorption efficiency (%) was above 60 % after third cycle for each Pb(II) ions concentration used, which confirmed the suitability of the nanocomposites for its reusability. This observation could also indicate that the interaction between the Pb(II) ions and the nanocomposites surface is a weak chemisorption due to the ease by which the Pb(II) ions are removed (Futalan *et al.*, 2011).

4.9.2 Regeneration Using Phenanthrenes

Adsorption-desorption studies were done using acetone solvent on prepared CNT-IPSF/Fe_3O_4 nanocomposites to determine the reliability of the adsorbent's reusability (Figure 4. 37).

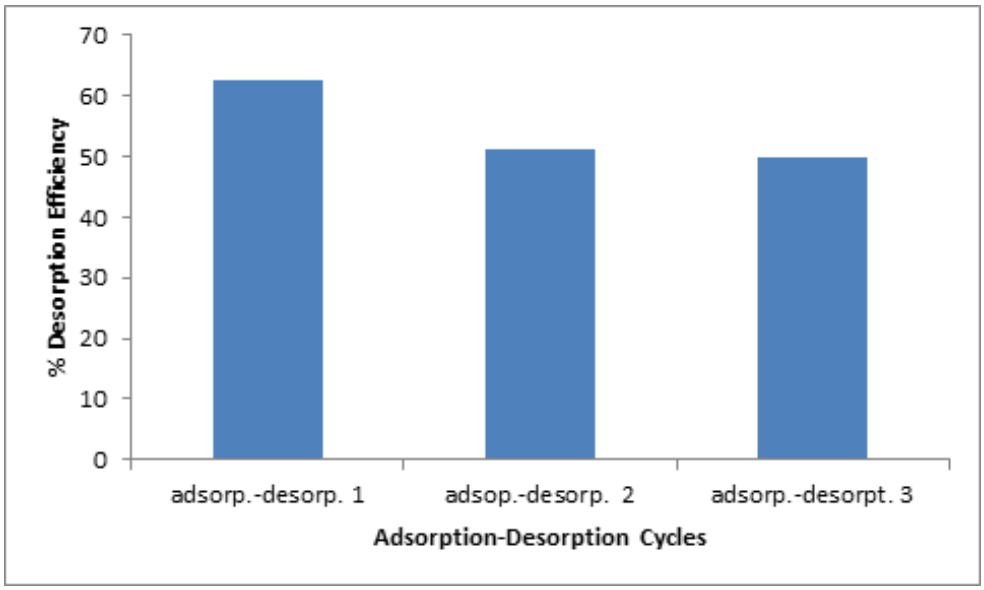

Figure 4. 37 Adsorption-desorption cycles for phenanthrenes

There was gradual decrease in % D.E for phenanthrene after three cycles showing good removal efficiency. This implied that no damaging of the adsorbent and hence it could advantageously be reused several times using acetone which is cheap and evaporates easily removing the pollutant. The % phenanthrenes desorbed by the nanocomposites decreased from 62.0 to 50.0 wt. % after third adsorption-desorption cycle.

The removal efficiency of 50 % after the third desorption cycle means that the nanocomposites can be reused several times which is an important characteristic of a good adsorbent (Ramana *et al.*, 2013). This could significantly reduce the cost of buying new adsorbents once reusability is confirmed.

Adsorption using low cost, simple and high removal efficiency adsorbent is a very promising method for purification of wastewater. In order to make this method more environment friendly and economical, regeneration of adsorbent is a very important aspect. Recently, few developments have inclined towards reusability of the spent

adsorbents with eluting agents such as acids, alkalis and chelating agents being employed.

Cukierman (2013) investigated thermal regeneration of activated carbon adsorbents using adsorbing volatile organic vapors such as acetone and methyl ethyl ketone (MEK) with dry air between 80 to 1600 K (Cukierman, 2013). It was observed that the regeneration efficiency increased by about 13 % with temperature for MEK implying that temperature change was not a factor. When the regeneration was tried using humid air, they found that the complete removal of adsorbate by humid air was not possible.

Velu et.al. (2003) reported regeneration of adsorbent used for spent oil using solvent washing, oxidative or reductive regeneration (Velu *et al.*, 2003). A mixture of methanol and toluene was used for solvent washing before the adsorbent was heated at high temperature. In reductive method; the adsorbent was treated with hydrogen at 400-500 °C. From this study, solvent washing was very effective and advantageous from environmental point of view.

Li Chai, et al. (2009) investigated the regeneration of modified spent grain used for lead removal using desorbing agents like HCl, NaOH, NaCl and ultrapure water (Li *et al.*, 2009). They observed that hydrochloric acid was the most efficient desorbing agent with 86 % efficiency while water and sodium chloride were not effective in removing the adsorbed materials. They also found that removal efficiency was directly related to concentration of HCl used. During their investigation, it was also observed that, above certain desorbent concentration, the increase in HCl concentration could lead to deterioration of the adsorbent.

An experimental and technical review on the steam regeneration of adsorbent was carried out (Shah *et al.*, 2013). According to them, any method adopted for regeneration depends on cost and nature of adsorbent. They observed that availability of steam generation units make this method common for regeneration. They however concluded that the drying of steam was energy intensive with the drying time being a concern.

Jeon and Kwon (2012) carried out investigation on adsorption and desorption of indium ions on phosphorylated sawdust (Jeon and Kwon, 2012). They found that about 97 %, 79 %, and 74 % regeneration was possible with 0.5N hydrochloric acid, ethylenediamine-tetraacetic acid and HCl respectively. They also observed that the desorption efficiency of recycled phosphorylated sawdust for indium ions could be kept at 85 % through 4 cycles. Bhuvaneshwari et.al. (2012) investigated the regeneration of chitosan after heavy metal sorption using dilute mineral acids and organic acids as eluents (Bhuvaneshwari *et al.*, 2012). They found that using sulphuric acid, 88 % of the chromium was recovered without any damage to the adsorbent and that the regenerated adsorbent was almost as efficient as the original new adsorbent.

Banana peel as bio-adsorbent was used for copper removal from which copper desorption up to 94 % was possible by 0.1 N sulphuric acid (Hossain *et al.*, 2012). They also observed that these cycles could be repeated for 7 times with satisfactory results. They also tried solvents such as tap water, distilled water and NaOH which exhibited limited amount of desorption (less than 30 %). Stability enhanced magnetic nanoparticles were used for rapid chromium removal from waster (Pang *et al.*, 2011) where the alkaline conditions suited desorption process. In their investigation using

sodium hydroxide solution for regeneration, they observed no significant decrease in the adsorption capacity after successive regenerations and that only 9 % drop in capacity was observed after 6 cycles.

Regeneration is a very important aspect of the adsorption from economy and environmental point of view with focus on disposal of adsorbent as one of the problems associated with the adsorption processes (Crini and Badot, 2008). Regeneration can reduce the need of new adsorbent and also eliminate the problem of disposal of the used adsorbent. Solvent washing regeneration method has been used in this study with some degree of success (Crini, 2005). The regeneration of the nanocomposites from lead and phenanthrene solutes was possible by using solvent washing. Normal drying at 60°C for the nanocomposites instead of electric heater showed promising results in terms of energy efficiency. The knowledge of both adsorption and desorption capacity of a material in a continuous adsorption/desorption cycle is an important factor in designing large-scale applications. It has been found that both sorption/desorption properties depend on the structure of the adsorbents and their surface properties.

4.10 CNT-IPSF/Fe_3O_4 Nanocomposites as Smart Materials in Water Remediation

Water pollution arising from industrial processes, underground storage tank leakages, landfills and abandoned mines pose great risk to human health. The main pollutants in wastewater include heavy metals like mercury, lead, cadmium, etc. and organic compounds like benzene, PAHs, etc. Most of the methods employed currently for the removal of such pollutants are too mechanical, time-consuming and costly.

Nanotechnology can help develop technologies with improved selectivity and sensitivity for in-situ remediation of inaccessible areas with minimal costs.

The fabricated CNT-IPSF/Fe_3O_4 nanocomposites contain mainly core shell nanoparticles and hydrophilic CNT-IPSF polymer. Heavy metal ions stick to core shell i.e. mainly silica coated iron oxide, which is generally magnetic so they can be removed from water using a magnet. The silica shell provides an inert layer over the magnetite core that protects it from oxidation and leaching during the remediation process. This technique is useful over other techniques for removal of heavy metal, as it is simple and doesn't use electricity.

The CNT-IPSF modified hydrophilic molecules enhance interaction with oil. They act as nano traps due to their high porosity and reactivity designed for such contaminants (Crini, 2005). The hydrophilic nanocomposites floats on the surface of water contaminated with oil and selectively absorb the oil. The oil-saturated nanocomposite is then removed by mechanical means. The infused polysulfone (IPSF) polymer provides hydrophilicity to the nanocomposites which protects it from fouling caused by interaction of the nanocomposite with the foulants in many different forms (inorganics, organics and biological substances) (Rana and Matsuura, 2010). Thus a combination of magnetite nanoparticles with CNT-IPSF gives rise to a smart magnetoresponsive composite material (CNT-IPSF/Fe_3O_4), which offers a novel chance for wastewater remediation.

CHAPTER FIVE

CONCLUSIONS AND RECOMMENDATIONS

5.1 Conclusions

CNT-IPSF/Fe_3O_4 nanocomposites were successfully fabricated from CNT-IPSF polymer and $SiO_2 \cdot Fe_3O_4$ nanoparticles based on various characterization procedures. Synthesized CNTs at 600 °C had threadlike twisting and winding entities for multiwalled CNTs with average diameters of 20 - 30 nanometers suitable in many applications. The presence of absorption band between 460 cm^{-1} and 521 cm^{-1} in the IR spectrum due to Fe−O bond confirmed the formation of Fe_3O_4 nanoparticles with saturation magnetization of 2.2 emu g^{-1} from SQUID confirming ferrimagnetic nanoparticles.

Nanocomposites recorded higher removal efficiencies of up to 69 % and 63 % for Pb(II) ions and phenanthrenes from wastewater, respectively. Optimization of parameters for Pb(II) ions removal gave adsorbent dose (0.05 g), contact time (60 minutes) and pH5 while the parameters for phenanthrenes removal were set at adsorbent dose (0.006 g), contact time (60 minutes) and pH5. Adsorption kinetics fitted well with pseudo-second-order model with R^2 >0.9 and the adsorption isotherm gave best fit to the Freundlich model. The CNT-IPSF/Fe_3O_4 nanocomposites had highest adsorption capacity when compared to other Fe_3O_4 based adsorbents hence it is more efficient.

Desorption efficiencies (%) for Pb(II) ions of above 60 % and gradual increase in desorption efficiency for phenanthrenes after three desorption cycles gives the fabricated CNT-IPSF/Fe_3O_4 nanocomposite its suitability for reuse. Desorption of the Pb(II) ions and phenanthrenes using HNO_3 and acetone (relatively non-toxic and

cheap organic solvent) respectively made the developed adsorbent a viable alternative to the common adsorbents available for treatment of wastewater with heavy metal ions and PAHs. The spent nanocomposites were regenerated by solvent washing treatment methods. The CNT-IPSF/Fe_3O_4 nanocomposites in this study could be recycled during the wastewater treatment.

5.2 Recommendations

The fabricated CNT-IPSF/Fe_3O_4 nanocomposites material has capability for use in water treatment due to their good adsorption capacity compared to commercial activated carbon.

5.3 Areas of Further Work

Further investigations should be done in the following areas.

i) There is need to investigate the use of the CNT-IPSF/Fe_3O_4 nanocomposite material on adsorption of more heavy metals and PAHs.

ii) Water remediation using the fabricated CNT-IPSF/Fe_3O_4 nanocomposites to large scale inaccessible polluted waters should be done.

iii) There is need to recover the water pollutants from regeneration solvents and carry out further investigations into the environmental side effects that may emanate from disposal of these nanomaterials since both health and environmental effects are not yet well understood.

REFERENCES

Abuilaiwi, F. A., Laoui, T., Al-Harthi, M. and Atieh, M. A. (2010). Modification and functionalization of multiwalled carbon nanotube (MWCNT) via fischer esterification. *The Arabian Journal for Science and Engineering* 35(1C): 37-48.

Adelodun, A. A., Lim, Y. H. and Jo, Y. M. (2014). Surface oxidation of activated carbon pellets by hydrogen peroxide for preparation of CO_2 adsorbent. *Journal of Industrial and Engineering Chemistry* 20(4): 2130-2137.

Afkhami, A., Saber-Tehrani, M. and Bagheri, H. (2010). Simultaneous removal of heavy-metal ions in wastewater samples using nano-alumina modified with 2, 4-dinitrophenylhydrazine. *Journal of Hazardous Materials* 181(1): 836-844.

Ahmad, T. and Phul, R. (2015).Magnetic Iron Oxide Nanoparticles as Contrast Agents: Hydrothermal Synthesis, Characterization and Properties. In *Solid State Phenomena*, Vol. 232, 111-145: Trans Tech Publications, Switzerland.

Ahmaruzzaman, M. (2010). A review on the utilization of fly ash. *Progress in Energy and Combustion Science* 36(3): 327-363.

Akaishi, A., Yonemaru, T. and Nakamura, J. (2017). Formation of Water Layers on Graphene Surfaces. *ACS Omega* 2(5): 2184-2190.

Akbarzadeh, A., Samiei, M. and Davaran, S. (2012). Magnetic nanoparticles: preparation, physical properties, and applications in biomedicine. *Nanoscale Research Letters* 7(1): 144.

Al-Degs, Y. S., El-Barghouthi, M. I., Issa, A. A., Khraisheh, M. A. and Walker, G. M. (2006). Sorption of Zn (II), Pb (II), and Co (II) using natural sorbents: equilibrium and kinetic studies. *Water Research* 40(14): 2645-2658.

Aliofkhazraei, M., Ali, N. and Michel, B. (2016). The 2nd International Conference on Surfaces, Coatings and Nanostructured Materials: Asia (NANOSMAT-Asia, 2015). *Microsystem Technologies* 22(5): 921-921.

Alslaibi, T. M., Abustan, I., Ahmad, M. A. and Foul, A. A. (2013). Application of response surface methodology (RSM) for optimization of Cu^{2+}, Cd^{2+}, Ni^{2+}, Pb^{2+}, Fe^{2+}, and Zn^{2+} removal from aqueous solution using microwaved olive stone activated carbon. *Journal of Chemical Technology and Biotechnology* 88(12): 2141-2151.

Althues, H., Henle, J. and Kaskel, S. (2007). Functional inorganic nanofillers for transparent polymers. *Chemical Society Reviews* 36(9): 1454-1465.

Amarasinghe, B. and Williams, R. (2007). Tea waste as a low cost adsorbent for the removal of Cu and Pb from wastewater. *Chemical Engineering Journal* 132(1): 299-309.

Andersson, J. T. and Achten, C. (2015). Time to say goodbye to the 16 EPA PAHs? Toward an up-to-date use of PACs for environmental purposes. *Polycyclic Aromatic Compounds* 35(2-4): 330-354.

Appel, C., Ma, L. Q., Rhue, R. D. and Kennelley, E. (2003). Point of zero charge determination in soils and minerals via traditional methods and detection of electroacoustic mobility. *Geoderma* 113(1): 77-93.

Atieh, M. A., Bakather, O. Y., Al-Tawbini, B., Bukhari, A. A., Abuilaiwi, F. A. and Fettouhi, M. B. (2011). Effect of carboxylic functional group functionalized on carbon nanotubes surface on the removal of lead from water. *Bioinorganic Chemistry and Applications* 2010.

Baaziz, W., Pichon, B. P., Fleutot, S., Liu, Y., Lefevre, C., Greneche, J.-M., Toumi, M., Mhiri, T. and Begin-Colin, S. (2014). Magnetic iron oxide nanoparticles: reproducible tuning of the size and nanosized-dependent composition, defects, and spin canting. *The Journal Of Physical Chemistry C* 118(7): 3795-3810.

Babel, S. and Kurniawan, T. A. (2003). Low-cost adsorbents for heavy metals uptake from contaminated water: A Review. *Journal of Hazardous Materials* 97(1): 219-243.

Banerjee, S., Hemraj-Benny, T. and Wong, S. S. (2005). Covalent surface chemistry of single-walled carbon nanotubes. *Advanced Materials* 17(1): 17-29.

Bang, J. H. and Suslick, K. S. (2010). Applications of ultrasound to the synthesis of nanostructured materials. *Advanced Materials* 22(10): 1039-1059.

Bankar, A. V., Kumar, A. R. and Zinjarde, S. S. (2009). Removal of chromium (VI) ions from aqueous solution by adsorption onto two marine isolates of Yarrowia lipolytica. *Journal of Hazardous Materials* 170(1): 487-494.

Barth, J. V., Costantini, G. and Kern, K. (2005). Engineering atomic and molecular nanostructures at surfaces. *Nature* 437(7059): 671-679.

Berube, D., Cummings, C., Cacciatore, M., Scheufele, D. and Kalin, J. (2011). Characteristics and classification of nanoparticles: expert Delphi survey. *Nanotoxicology* 5(2): 236-243.

Bhattacharya, S., Saha, I., Mukhopadhyay, A., Chattopadhyay, D. and Chand, U. (2013). Role of nanotechnology in water treatment and purification: Potential applications and implications. *International Journal of Chemical Science Technology* 3(3): 59-64.

Bhuvaneshwari, S., Sruthi, D., Sivasubramanian, V. and Kanthimathy, K. (2012). Regeneration of chitosan after heavy metal sorption. *Journal of Scientific and Industrial Research* 71(4): 266.

Blanch, A. J., Lenehan, C. E., and Quinton, J. S. (2010). Optimizing surfactant concentrations for dispersion of single-walled carbon nanotubes in aqueous solution. *The Journal of Physical Chemistry B* 114(30): 9805-9811.

Blaney, L. (2007). Magnetite (Fe_3O_4): Properties, synthesis, and applications. Vol 15, 5

Bradl, H. B. (2004). Adsorption of heavy metal ions on soils and soils constituents. *Journal of Colloid and Interface Science* 277(1): 1-18.

Brinker, C. J. and Scherer, G. W. (2013). Sol-gel science: the physics and chemistry of sol-gel processing. *Journal of Non-Crystalline Solids* 70 (3), 301-322

Callister, W. D. and Rethwisch, D. G. (2012). Fundamentals of materials science and engineering: an integrated approach. John Wiley and Sons.

Čapek, L., Kreibich, V., Dědeček, J., Grygar, T., Wichterlova, B., Sobalik, Z., Martens, J., Brosius, R. and Tokarova, V. (2005). Analysis of Fe species in zeolites by UV–VIS–NIR, IR spectra and voltammetry. Effect of preparation, Fe loading and zeolite type. *Microporous and Mesoporous Materials* 80(1): 279-289.

Carrey, J., Mehdaoui, B. and Respaud, M. (2011). Simple models for dynamic hysteresis loop calculations of magnetic single-domain nanoparticles: Application to magnetic hyperthermia optimization. *Journal of Applied Physics* 109(8): 083921.

Chen, C.-W. (2013). Magnetism and metallurgy of soft magnetic materials. Courier Corporation.

Chen, S., Feng, J., Guo, X., Hong, J. and Ding, W. (2005). One-step wet chemistry for preparation of magnetite nanorods. *Materials Letters* 59(8): 985-988.

Chipera, S. J. and Bish, D. L. (2002). FULLPAT: a full-pattern quantitative analysis program for X-ray powder diffraction using measured and calculated patterns. *Journal of Applied Crystallography* 35(6): 744-749.

Cohen, G. E. (2000). Mixing Zones: Diluting Pollution Under the Clean Water Act. *Tulane Environmental Law Journal* 14(1): 1-94.

Corcoran, E. (2010). Sick water?: the central role of wastewater management in sustainable development: a rapid response assessment. UNEP/Earthprint.

Cornell, R. M. and S chwertmann, U. (2003). The iron oxides: structure, properties, reactions, occurrences and uses. John Wiley and Sons.

Crabtree, R. H. (2009). The organometallic chemistry of the transition metals. John Wiley and Sons.

Crini, G. (2005). Recent developments in polysaccharide-based materials used as adsorbents in wastewater treatment. *Progress in Polymer Science* 30(1): 38-70.

Crini, G. and Badot, P.-M. (2008). Application of chitosan, a natural aminopolysaccharide, for dye removal from aqueous solutions by adsorption processes using batch studies: a review of recent literature. *Progress in Polymer Science* 33(4): 399-447.

Crini, G., Peindy, H. N., Gimbert, F. and Robert, C. (2007). Removal of CI Basic Green 4 (Malachite Green) from aqueous solutions by adsorption using cyclodextrin-based adsorbent: Kinetic and equilibrium studies. *Separation and Purification Technology* 53(1): 97-110.

Cukierman, A. L. (2013). Development and environmental applications of activated carbon cloths. *ISRN Chemical Engineering* 2013.

Cullity, B. D. and Graham, C. D. (2011). *Introduction to magnetic materials.* John Wiley and Sons.

Das, N., Vimala, R. and Karthika, P. (2008). Biosorption of heavy metals—an overview. *Indian Journal of Biotechnology* 7(2): 159-169.

Datsyuk, V., Kalyva, M., Papagelis, K., Parthenios, J., Tasis, D., Siokou, A., Kallitsis, I. and Galiotis, C. (2008). Chemical oxidation of multiwalled carbon nanotubes. *Carbon* 46(6): 833-840.

Deng, L., Su, Y., Su, H., Wang, X. and Zhu, X. (2007). Sorption and desorption of lead (II) from wastewater by green algae Cladophora fascicularis. *Journal of Hazardous Materials* 143(1): 220-225.

Deng, Y., Qi, D., Deng, C., Zhang, X. and Zhao, D. (2008). Superparamagnetic high-magnetization microspheres with an Fe_3O_4.SiO_2 core and perpendicularly aligned mesoporous SiO2 shell for removal of microcystins. *Journal of the American Chemical Society* 130(1): 28-29.

Deshmukh, P. K., Ramani, K. P., Singh, S. S., Tekade, A. R., Chatap, V. K., Patil, G. B. and Bari, S. B. (2013). Stimuli-sensitive layer-by-layer (LbL) self-assembly systems: targeting and biosensory applications. *Journal of Controlled Release* 166(3): 294-306.

Dharmambal, S., Mani, N. and Kannan, D. (2015). Adsorption of Rhodamine-B Dye from the aqueous Solution by using Tectonagrandis Bark Powder. *Asian Journal of Research in Chemistry* 8(5): 346.

Dhingra, R., Naidu, S., Upreti, G. and Sawhney, R. (2010). Sustainable nanotechnology: through green methods and life-cycle thinking. *Sustainability* 2(10): 3323-3338.

Ding, S., Chen, J. S., Luan, D., Boey, F. Y. C., Madhavi, S. and Lou, X. W. D. (2011). Graphene-supported anatase TiO 2 nanosheets for fast lithium storage. *Chemical Communications* 47(20): 5780-5782.

Dong, X., Potter, D. and Erkey, C. (2002). Synthesis of CuS nanoparticles in water-in-carbon dioxide microemulsions. *Industrial and Engineering Chemistry Research* 41(18): 4489-4493.

Dormann, J. and Fiorani, D. (2012). Magnetic properties of fine particles. Elsevier.

Epstein, M. J. and Buhovac, A. R. (2014). Making sustainability work: Best practices in managing and measuring corporate social, environmental, and economic impacts. Berrett-Koehler Publishers.

Fagaly, R. (2006). Superconducting quantum interference device instruments and applications. *Review of Scientific Instruments* 77(10): 101101.

Fan, Y.-Y., Kaufmann, A., Mukasyan, A. and Varma, A. (2006). Single-and multi-wall carbon nanotubes produced using the floating catalyst method: Synthesis, purification and hydrogen up-take. *Carbon* 44(11): 2160-2170.

Felicia, L. J. and Philip, J. (2012). Probing of field-induced structures and tunable rheological properties of surfactant capped magnetically polarizable nanofluids. *Langmuir* 29(1): 110-120.

Fu, F. and Wang, Q. (2011). Removal of heavy metal ions from wastewaters: a review. *Journal of Environmental Management* 92(3): 407-418.

Fu, S.-Y., Feng, X.-Q., Lauke, B. and Mai, Y.-W. (2008). Effects of particle size, particle/matrix interface adhesion and particle loading on mechanical properties of particulate–polymer composites. *Composites Part B: Engineering* 39(6): 933-961.

Futalan, C. M., Kan, C.-C., Dalida, M. L., Hsien, K.-J., Pascua, C. and Wan, M.-W. (2011). Comparative and competitive adsorption of copper, lead, and nickel using chitosan immobilized on bentonite. *Carbohydrate Polymers* 83(2): 528-536.

Gadipelly, C., Pérez-González, A., Yadav, G. D., Ortiz, I., Ibáñez, R., Rathod, V. K. and Marathe, K. V. (2014). Pharmaceutical industry wastewater: review of the technologies for water treatment and reuse. *Industrial and Engineering Chemistry Research* 53(29): 11571-11592.

Gan, Q., Rooney, D., Xue, M., Thompson, G. and Zou, Y. (2006). An experimental study of gas transport and separation properties of ionic liquids supported on nanofiltration membranes. *Journal of Membrane Science* 280(1): 948-956.

Ghaedi, M., Shokrollahi, A., Kianfar, A., Mirsadeghi, A., Pourfarokhi, A. and Soylak, M. (2008). The determination of some heavy metals in food samples by flame atomic absorption spectrometry after their separation-preconcentration on bis salicyl aldehyde, 1, 3 propan diimine (BSPDI) loaded on activated carbon. *Journal of Hazardous Materials* 154(1): 128-134.

Ghandoor, H., Zidan, H., M, Khalil, M. M., H and Ismail, M., M (2012). Synthesis and some physical properties of magnetite (Fe_3O_4) nanoparticles. *International Journal of Electrochemical Science* 7(6): 5734-5745.

Ghosh, R. and Paria, S. (2011). Core/shell nanoparticles: classes, properties, synthesis mechanisms, characterization, and applications. *Chemical Reviews* 112(4): 2373-2433.

Gohil, J. and Ray, P. (2009). Polyvinyl alcohol as the barrier layer in thin film composite nanofiltration membranes: Preparation, characterization, and performance evaluation. *Journal of Colloid and Interface Science* 338(1): 121-127.

Gojny, F. H., Wichmann, M. H., Fiedler, B. and Schulte, K. (2005). Influence of different carbon nanotubes on the mechanical properties of epoxy matrix composites–a comparative study. *Composites Science and Technology* 65(15): 2300-2313.

Göksungur, Y., Üren, S. and Güvenç, U. (2005). Biosorption of cadmium and lead ions by ethanol treated waste baker's yeast biomass. *Bioresource Technology* 96(1): 103-109.

Goldstein, J., Newbury, D. E., Echlin, P., Joy, D. C., Romig Jr, A. D., Lyman, C. E., Fiori, C. and Lifshin, E. (2012). Scanning electron microscopy and X-ray microanalysis: a text for biologists, materials scientists, and geologists. Springer Science and Business Media.

Gorjizadeh, N. and Kawazoe, Y. (2010). Chemical functionalization of graphene nanoribbons. *Journal of Nanomaterials* 2010: 5.

Gotovac, S., Hattori, Y., Noguchi, D., Miyamoto, J.-i., Kanamaru, M., Utsumi, S., Kanoh, H. and Kaneko, K. (2006). Phenanthrene adsorption from solution on single wall carbon nanotubes. *The Journal of Physical Chemistry B* 110(33): 16219-16224.

Goyal, K., Amit, S., Johal, E. and Rath, G. (2011). Nanotechnology for water treatment. *Current Nanoscience* 7(4): 640-654.

Griffiths, P. R. and Haseth, J. A. (2007). Fourier transform infrared spectrometry. John Wiley and Sons.

Grigorian, L., Hornyak, L., Dillon, A. C. and Heben, M. J. (2008).Continuous growth of single-wall carbon nanotubes using chemical vapor deposition. Google Patents.

Gupta, V. K., Ali, I., Saleh, T. A., Nayak, A. and Agarwal, S. (2012). Chemical treatment technologies for waste-water recycling—an overview. *RSC Advances* 2(16): 6380-6388.

Hajipour, M. J., Fromm, K. M., Ashkarran, A. A., de Aberasturi, D. J., de Larramendi, I. R., Rojo, T., Serpooshan, V., Parak, W. J. and Mahmoudi, M. (2012). Antibacterial properties of nanoparticles. *Trends in Biotechnology* 30(10): 499-511.

Han, Z. and Fina, A. (2011). Thermal conductivity of carbon nanotubes and their polymer nanocomposites: a review. *Progress in Polymer Science* 36(7): 914-944.

Haritash, A. and Kaushik, C. (2009). Biodegradation aspects of polycyclic aromatic hydrocarbons (PAHs): a review. *Journal of Hazardous Materials* 169(1): 1-15.

Harris, P. J. F. (2009). Carbon nanotube science: synthesis, properties and applications. Cambridge university press.

Hashemian, S., Salari, K., Salehifar, H. and Atashi Yazdi, Z. (2013). Removal of azo dyes (Violet B and Violet 5R) from aqueous solution using new activated carbon developed from orange peel. *Journal of Chemistry* 2013.

He, R., You, X., Shao, J., Gao, F., Pan, B. and Cui, D. (2007). Core/shell fluorescent magnetic silica-coated composite nanoparticles for bioconjugation. *Nanotechnology* 18(31): 315601.

Hillier, S. (2000). Accurate quantitative analysis of clay and other minerals in sandstones by XRD: comparison of a Rietveld and a reference intensity ratio (RIR) method and the importance of sample preparation. *Clay Minerals* 35(1): 291-302.

Hossain, M., Ngo, H. H., Guo, W. and Nguyen, T. (2012). Removal of copper from water by adsorption onto banana peel as bioadsorbent. *International Journal of Geomate* 2: 227-234.

Huang, L.-Z., Hassenkam, T., Hansen, H. C. B. and Bjerrum, M. J. (2014). Single sheet iron oxide based films: electrochemical properties with in situ UV-vis measurement. *Journal of Materials Chemistry A* 2(11): 4029-4037.

Ismail, M. G. B. H., Weng, C. N., Rahman, H. A. and Zakaria, N. A. (2013). Freundlich Isotherm Equilibrium Equastions in Determining Effectiveness a Low Cost Absorbent to Heavy Metal Removal In Wastewater (Leachate) At Teluk Kitang Landfill, Pengkalan Chepa, Kelantan, Malaysia. *Journal of Geography and Earth Science* 1(1): 01-08.

Jayaprabha, K. and Joy, P. (2014). Curcumin encapsulated superparamagnetic iron oxide based nanofluids for possible multifunctional applications. *Journal of Nanofluids* 3(1): 1-7.

Jeon, C. and Kwon, T.-N. (2012). Desorption and regeneration characteristics for previously adsorbed indium ions to phosphorylated sawdust. *Environmental Engineering Research* 17(2): 65-67.

Jolivet, J.-P., Chanéac, C. and Tronc, E. (2004). Iron oxide chemistry. From molecular clusters to extended solid networks. *Chemical Communications* (5): 481-483.

Kaewsarn, P., Yu, Q. and Ma, W. (2001). Interference of co-ions in biosorption of Cu2+ by biosorbent from marine alga Durvillaea potatorum. *Environmental Engineering Science* 18(2): 99-104.

Kamonji, F. C. (2012).Lead poisoning from used lead acid battery recycling: a case study of Owino-Uhuru, Mombasa, Kenya. In *Geological Society of America Abstracts with Programs*, Vol. 44, 111.

Karşı, D. (2014).Karbon Nanotüp Katkılı Nanokompozit Polimerik Membranların Üretimi, Karakterizasyonu Ve Uygulaması. Fen Bilimleri Enstitüsü.

Khajeh, M., Laurent, S. and Dastafkan, K. (2013). Nanoadsorbents: classification, preparation, and applications (with emphasis on aqueous media). *Chemical Reviews* 113(10): 7728-7768.

Khandanlou, R., Ahmad, M. B., Masoumi, H. R. F., Shameli, K., Basri, M. and Kalantari, K. (2015). Rapid Adsorption of Copper (II) and Lead (II) by Rice Straw/Fe_3O_4 Nanocomposite: Optimization, Equilibrium Isotherms, and Adsorption Kinetics Study. *PloS one* 10(3): e0120264.

Khandhar, A. P., Ferguson, R. M., Simon, J. A. and Krishnan, K. M. (2012). Tailored magnetic nanoparticles for optimizing magnetic fluid hyperthermia. *Journal of Biomedical Materials Research Part A* 100(3): 728-737.

Kim, J. and Van der Bruggen, B. (2010). The use of nanoparticles in polymeric and ceramic membrane structures: review of manufacturing procedures and performance improvement for water treatment. *Environmental Pollution* 158(7): 2335-2349.

Kim, Y. Y., Yang, Y. Y. and Lee, Y. (2002). Pb and Cd uptake in rice roots. *Physiologia Plantarum* 116(3): 368-372.

Kleiner, R., Koelle, D., Ludwig, F. and Clarke, J. (2004). Superconducting quantum interference devices: State of the art and applications. *Proceedings of the IEEE* 92(10): 1534-1548.

Kolhatkar, A. G., Jamison, A. C., Litvinov, D., Willson, R. C. and Lee, T. R. (2013). Tuning the magnetic properties of nanoparticles. *International Journal of Molecular Sciences* 14(8): 15977-16009.

Kothari, C. R. (2004). Research methodology: Methods and techniques. New Age International.

Kuchibhatla, S. V., Karakoti, A., Bera, D. and Seal, S. (2007). One dimensional nanostructured materials. *Progress in Materials Science* 52(5): 699-913.

Kucki, M., Cavelius, C. and Kraegeloh, A. (2013). Interference of silica nanoparticles with the traditional Limulus amebocyte lysate gel clot assay. *Innate Immunity*: 1753425913492833.

Kulkarni, S. A., Sawadh, P. and Palei, P. K. (2014). Synthesis and Characterization of Superparamagnetic Fe_3O_4.SiO_2 Nanoparticles. *Journal of Korean Chemical Society* 58.

Kumar, S. S., Manoj, P. and Giridhar, P. (2015). Fourier transform infrared spectroscopy (FTIR) analysis, chlorophyll content and antioxidant properties of native and defatted foliage of green leafy vegetables. *Journal of Food Science and Technology* 52(12): 8131-8139.

Lahure (2015). Preparation and Characterization of Magnetite Nanoparticle using Green Synthesis. *International Journal of Research in Chemistry and Environment* 5(4): 38-43.

Laoui, T., Al-Amer, A. M., Khalil, A. B., Abbas, A., Khraisheh, M. and Atieh, M. A. (2015). Novel anti-microbial membrane for desalination pretreatment: a silver nanoparticle-doped carbon nanotube membrane. *Desalination* 376: 82-93.

Lasheen, M. R., Ammar, N. S. and Ibrahim, H. S. (2012). Adsorption/desorption of Cd (II), Cu (II) and Pb (II) using chemically modified orange peel: Equilibrium and kinetic studies. *Solid State Sciences* 14(2): 202-210.

Li, C., Li, Z., Zhu, H., Wang, K., Wei, J., Li, X., Sun, P., Zhang, H. and Wu, D. (2010). Graphene nano-"patches" on a carbon nanotube network for highly transparent/conductive thin film applications. *The Journal of Physical Chemistry C* 114(33): 14008-14012.

Li, Q.-Z., Chai, L.-Y., Jing, Z., Yang, Z.-H. and Wang, Q.-W. (2009). Lead desorption from modified spent grain. *Transactions of Nonferrous Metals Society of China* 19(5): 1371-1376.

Li, X.-M., Xu, G., Liu, Y. and He, T. (2011). Magnetic Fe3O4 nanoparticles: synthesis and application in water treatment. *Nanoscience and Nanotechnology-Asia* 1(1): 14-24.

Lopez, J. A., González, F., Bonilla, F. A., Zambrano, G. and Gómez, M. E. (2010). Synthesis and characterization of Fe_3O_4 magnetic nanofluid. *Revista Latinoamericana de Metalurgia y Materiales*: 60-66.

Lu, A. H., Salabas, E. e. L. and Schüth, F. (2007). Magnetic nanoparticles: synthesis, protection, functionalization, and application. *Angewandte Chemie International Edition* 46(8): 1222-1244.

Ma, X.-k., ling Wu, L. and Fam, H. (2014). Heavy metal ions affecting the removal of polycyclic aromatic hydrocarbons by fungi with heavy-metal resistance. *Applied Microbiology and Biotechnology* 98(23): 9817-9827.

Madejová, J. (2003). FTIR techniques in clay mineral studies. *Vibrational Spectroscopy* 31(1): 1-10.

Mahdavi, M., Ahmad, M. B., Haron, M. J., Gharayebi, Y., Shameli, K. and Nadi, B. (2013a). Fabrication and characterization of SiO_2/(3-aminopropyl) triethoxysilane-coated magnetite nanoparticles for lead (II) removal from aqueous solution. *Journal of Inorganic and Organometallic Polymers and Materials* 23(3): 599-607.

Mahdavi, M., Ahmad, M. B., Haron, M. J., Namvar, F., Nadi, B., Rahman, M. Z. A. and Amin, J. (2013b). Synthesis, surface modification and characterisation of biocompatible magnetic iron oxide nanoparticles for biomedical applications. *Molecules* 18(7): 7533-7548.

Mahmoudi, M., Sant, S., Wang, B., Laurent, S. and Sen, T. (2011). Superparamagnetic iron oxide nanoparticles (SPIONs): development, surface modification and applications in chemotherapy. *Advanced Drug Delivery Reviews* 63(1): 24-46.

Malato, S., Fernández-Ibáñez, P., Maldonado, M., Blanco, J. and Gernjak, W. (2009). Decontamination and disinfection of water by solar photocatalysis: recent overview and trends. *Catalysis Today* 147(1): 1-59.

Mallick, P. K. (2007). Fiber-reinforced composites: materials, manufacturing, and design. CRC press.

Marimuthu, G., Ramalingam, K., Rizzoli, C. and Arivanandhan, M. (2012). Solvothermal preparation of nano-β-HgS from a precursor, bis (dibenzyldithiocarbamato) mercury (II). *Journal of Nanoparticle Research* 14(2): 1-11.

Mark, F. (2001).Optical properties of solids. Oxford University Press, New York.

Marshall, S. (2011). The water crisis in Kenya: Causes, effects and solutions. *Global Majority E-Journal* 2(1): 31-45.

Martins, B. L., Cruz, C. C., Luna, A. S. and Henriques, C. A. (2006). Sorption and desorption of Pb^{2+} ions by dead Sargassum sp. biomass. *Biochemical Engineering Journal* 27(3): 310-314.

Mateen, F., Javed, I., Rafique, U., Tabassum, N., Sarfraz, M., Safi, S. Z., Yusoff, I. and Ashraf, M. A. (2015). New method for the adsorption of organic pollutants using natural zeolite incinerator ash (ZIA) and its application as an environmentally friendly and cost-effective adsorbent. *Desalination and Water Treatment* (ahead-of-print): 1-9.

McClements, D. J. (2012). Nanoemulsions versus microemulsions: terminology, differences, and similarities. *Soft Matter* 8(6): 1719-1729.

Meena, A. K., Mishra, G., Rai, P., Rajagopal, C. and Nagar, P. (2005). Removal of heavy metal ions from aqueous solutions using carbon aerogel as an adsorbent. *Journal of Hazardous Materials* 122(1): 161-170.

Mishra, S. (2014). Adsorption–desorption of heavy metal ions. *Current. Sciences* 107(4): 601-612.

Moghaddam, H. K. and Pakizeh, M. (2015). Experimental study on mercury ions removal from aqueous solution by MnO_2/CNTs nanocomposite adsorbent. *Journal of Industrial and Engineering Chemistry* 21: 221-229.

Muir, D. C. and Howard, P. H. (2006). Are there other persistent organic pollutants? A challenge for environmental chemists. *Environmental Science and Technology* 40(23): 7157-7166.

Mukhopadhyay, A., Joshi, N., Chattopadhyay, K. and De, G. (2011). A facile synthesis of PEG-coated magnetite (Fe_3O_4) nanoparticles and their prevention of the reduction of cytochrome C. *ACS Applied Materials and Interfaces* 4(1): 142-149.

Musameh, M. M., Hickey, M. and Kyratzis, I. L. (2011). Carbon nanotube-based extraction and electrochemical detection of heavy metals. *Research on Chemical Intermediates* 37(7): 675-689.

Nagl, S. and Wolfbeis, O. S. (2008).Classification of chemical sensors and biosensors based on fluorescence and phosphorescence. In *Standardization and Quality Assurance in Fluorescence Measurements I*, 325-346: Springer.

Najm, I. and Trussell, R. R. (1999). New and emerging drinking water treatment technologies. *Identifying future drinking water contaminants*: 220.

Nehl, C. L., Liao, H. and Hafner, J. H. (2006). Optical properties of star-shaped gold nanoparticles. *Nano Letters* 6(4): 683-688.

Ngah, W. W., Endud, C. and Mayanar, R. (2002). Removal of copper (II) ions from aqueous solution onto chitosan and cross-linked chitosan beads. *Reactive and Functional Polymers* 50(2): 181-190.

Ngah, W. W. and Fatinathan, S. (2008). Adsorption of Cu (II) ions in aqueous solution using chitosan beads, chitosan–GLA beads and chitosan–alginate beads. *Chemical Engineering Journal* 143(1): 62-72.

Ngo, T. H., Do, H. M., Tran, V. H. and Nguyen, X. P. (2010). Facile and solvent-free routes for the synthesis of size-controllable Fe_3O_4 nanoparticles. *Advances in Natural Sciences: Nanoscience and Nanotechnology* 1(3): 035001.

Nidhin, M., Indumathy, R., Sreeram, K. and Nair, B. U. (2008). Synthesis of iron oxide nanoparticles of narrow size distribution on polysaccharide templates. *Bulletin of Materials Science* 31(1): 93-96.

Ochanda, F., Cho, K., Andala, D., Keane, T. C., Atkinson, A. and Jones Jr, W. E. (2009). Synthesis and optical properties of Co-doped ZnO submicrometer tubes from electrospun fiber templates. *Langmuir* 25(13): 7547-7552.

Oh, J. K. and Park, J. M. (2011). Iron oxide-based superparamagnetic polymeric nanomaterials: design, preparation, and biomedical application. *Progress in Polymer Science* 36(1): 168-189.

Okoli, C. P., Adewuyi, G. O., Zhang, Q., Zhu, G., Wang, C. and Guo, Q. (2015). Aqueous scavenging of polycyclic aromatic hydrocarbons using epichlorohydrin, 1, 6-hexamethylene diisocyanate and 4, 4-methylene diphenyl diisocyanate modified starch: Pollution remediation approach. *Arabian Journal of Chemistry*.

Onditi, M., Adelodun, A. A., Changamu, E. O. and Ngila, J. C. (2016). Removal of Pb^{2+} and Cd^{2+} from drinking water using polysaccharide extract isolated from cactus pads (Opuntia ficus indica). *Journal of Applied Polymer Science* 133(38).

Örnek, A., Özacar, M. and Şengil, İ. A. (2007). Adsorption of lead onto formaldehyde or sulphuric acid treated acorn waste: equilibrium and kinetic studies. *Biochemical Engineering Journal* 37(2): 192-200.

Owabor, C., Agarry, S. and Jato, D. (2012). Removal of naphthalene from aqueous system using unripe orange peel as adsorbent: effects of operating variables. *Desalination and Water Treatment* 48(1-3): 315-319.

Pala, R. A., White, J., Barnard, E., Liu, J. and Brongersma, M. L. (2009). Design of plasmonic thin-film solar cells with broadband absorption enhancements. *Advanced Materials* 21(34): 3504-3509.

Pandey, R., Kumar, P., Singh, A. K., Shahid, M., Li, P.-z., Singh, S. K., Xu, Q., Misra, A. and Pandey, D. S. (2011). Fluorescent zinc (II) complex exhibiting "on-off-on" switching toward Cu^{2+} and Ag^{+} ions. *Inorganic Chemistry* 50(8): 3189-3197.

Pang, Y., Zeng, G., Tang, L., Zhang, Y., Liu, Y., Lei, X., Li, Z., Zhang, J., Liu, Z. and Xiong, Y. (2011). Preparation and application of stability enhanced magnetic nanoparticles for rapid removal of Cr (VI). *Chemical Engineering Journal* 175: 222-227.

Paria, S. (2008). Surfactant-enhanced remediation of organic contaminated soil and water. *Advances in Colloid and Interface Science* 138(1): 24-58.

Pathan, A., Bond, J. and Gaskin, R. (2010). Sample preparation for SEM of plant surfaces. *Materials Today* 12: 32-43.

Patnaik, P. (2010). Handbook of environmental analysis: chemical pollutants in air, water, soil, and solid wastes. CRC Press.

Patrick, L. (2006). Lead toxicity part II: the role of free radical damage and the use of antioxidants in the pathology and treatment of lead toxicity. *Alternative Medicine Review* 11(2): 114.

Pendergast, M. M. and Hoek, E. M. (2011). A review of water treatment membrane nanotechnologies. *Energy and Environmental Science* 4(6): 1946-1971.

Peng, H., Pan, B., Wu, M., Liu, R., Zhang, D., Wu, D. and Xing, B. (2012). Adsorption of ofloxacin on carbon nanotubes: solubility, pH and cosolvent effects. *Journal of Hazardous Materials* 211: 342-348.

Pierard, N., Fonseca, A., Konya, Z., Willems, I., Van Tendeloo, G. and Nagy, J. B. (2001). Production of short carbon nanotubes with open tips by ball milling. *Chemical Physics Letters* 335(1): 1-8.

Poater, J., Solà, M. and Bickelhaupt, F. M. (2006). Hydrogen–Hydrogen Bonding in Planar Biphenyl, Predicted by Atoms-In-Molecules Theory, Does Not Exist. *Chemistry–A European Journal* 12(10): 2889-2895.

Pogue, B. W., Poplack, S. P., McBride, T. O., Wells, W. A., Osterman, K. S., Osterberg, U. L. and Paulsen, K. D. (2001). Quantitative Hemoglobin Tomography with Diffuse Near-Infrared Spectroscopy: Pilot Results in the Breast 1. *Radiology* 218(1): 261-266.

Porjazoska, K, Aleksandra, M and Liljana, M. (2015). Adsorption kinetic models of heavy metal ions on granular activated carbon. *Zaštita Materijala* 56(2): 179-190.

Qu, X., Alvarez, P. J. and Li, Q. (2013). Applications of nanotechnology in water and wastewater treatment. *Water Research* 47(12): 3931-3946.

Ramana, D. V., Yu, J. S. and Seshaiah, K. (2013). Silver nanoparticles deposited multiwalled carbon nanotubes for removal of Cu (II) and Cd (II) from water: Surface, kinetic, equilibrium, and thermal adsorption properties. *Chemical Engineering Journal* 223: 806-815.

Rana, D. and Matsuura, T. (2010). Surface modifications for antifouling membranes. *Chemical Reviews* 110(4): 2448-2471.

Ranke, W. (2002).Modern methods in heterogeneous catalysis research: Theory and experiment. Thermal analysis-TDS. In *Modern Methods in Heterogeneous Catalysis Research: Theory and Experiment*.

Ray, P. C. (2010). Size and shape dependent second order nonlinear optical properties of nanomaterials and their application in biological and chemical sensing. *Chemical Reviews* 110(9): 5332-5365.

Rehani, B. R., Joshi, P., Lad, K. N. and Pratap, A. (2006). Crystallite size estimation of elemental and composite silver nano-powders using XRD principles. *Indian Journal of Pure and Applied Physics* 44(2): 157-161.

Ren, X., Chen, C., Nagatsu, M. and Wang, X. (2011). Carbon nanotubes as adsorbents in environmental pollution management: A Review. *Chemical Engineering Journal* 170(2): 395-410.

Sadaka, M., Young, C., Ganguli, R. and Mehrotra, V. (2007).Magnetic materials made from magnetic nanoparticles and associated methods. Google Patents.

Sanchez, C., Belleville, P., Popall, M. and Nicole, L. (2011). Applications of advanced hybrid organic–inorganic nanomaterials: from laboratory to market. *Chemical Society Reviews* 40(2): 696-753.

Saravanan, R. and Ravikumar, L. (2015). The Use of New Chemically Modified Cellulose for Heavy Metal Ion Adsorption and Antimicrobial Activities. *Journal of Water Resource and Protection* 7(06): 530.

Senz, S., Blum, W. and Hesse, D. (2001). The effect of stress on cubic-to-tetragonal phase transitions in Mg_2TiO_4 and Mg_2GeO_4 spinel films. *Philosophical Magazine A* 81(1): 109-124.

Shaaban, E., Ahmad, M., Wahab, E. A., Hassan, H. S. and Aboraia, A. (2013).Structural and optical properties of varies thickness of ZnTe nanoparticle. In *Book of Proceedings*.

Shah, I. K., Pre, P. and Alappat, B. J. (2013). Steam regeneration of adsorbents: an experimental and technical review. *Journal of Chemical Sciences* 2(4): 1078-1088.

Shannon, M. A., Bohn, P. W., Elimelech, M., Georgiadis, J. G., Marinas, B. J. and Mayes, A. M. (2008). Science and technology for water purification in the coming decades. *Nature* 452(7185): 301-310.

Sheela, T. and Nayaka, Y. A. (2012). Kinetics and thermodynamics of cadmium and lead ions adsorption on NiO nanoparticles. *Chemical Engineering Journal* 191: 123-131.

Sigel, A., Sigel, H. and Sigel, R. (2011). Metal ions in toxicology: effects, interactions, interdependencies. *Metal Ions Life Sciences* 8.

Smičiklas, I., Milonjić, S., Pfendt, P. and Raičević, S. (2000). The point of zero charge and sorption of cadmium (II) and strontium (II) ions on synthetic hydroxyapatite. *Separation and Purification Technology* 18(3): 185-194.

Sodipo, B. K. and Aziz, A. A. (2013).Sonochemical synthesis of silica coated super paramagnetic iron oxide nanoparticles. In *Materials Science Forum*, Vol. 756, 74-79: Trans Tech Publications, Switzerland.

Spitalsky, Z., Tasis, D., Papagelis, K. and Galiotis, C. (2010). Carbon nanotube–polymer composites: chemistry, processing, mechanical and electrical properties. *Progress in Polymer Science* 35(3): 357-401.

Sreejalekshmi, K., Krishnan, K. A. and Anirudhan, T. (2009). Adsorption of Pb (II) and Pb (II)-citric acid on sawdust activated carbon: Kinetic and equilibrium isotherm studies. *Journal of Hazardous Materials* 161(2): 1506-1513.

Stafiej, A. and Pyrzynska, K. (2007). Adsorption of heavy metal ions with carbon nanotubes. *Separation and Purification Technology* 58(1): 49-52.

Stein, A., Wang, Z. and Fierke, M. A. (2009). Functionalization of porous carbon materials with designed pore architecture. *Advanced Materials* 21(3): 265-293.

Storhoff, J. J., Lazarides, A. A., Mucic, R. C., Mirkin, C. A., Letsinger, R. L. and Schatz, G. C. (2000). What controls the optical properties of DNA-linked gold nanoparticle assemblies? *Journal of the American Chemical Society* 122(19): 4640-4650.

Sun, C., Li, H. and Chen, L. (2012). Nanostructured ceria-based materials: synthesis, properties, and applications. *Energy and Environmental Science* 5(9): 8475-8505.

Sun, S., Zeng, H., Robinson, D. B., Raoux, S., Rice, P. M., Wang, S. X. and Li, G. (2004). Monodisperse MFe_2O_4 (M= Fe, Co, Mn) nanoparticles. *Journal of the American Chemical Society* 126(1): 273-279.

Suryanarayana, C. and Norton, M. G. (2013). X-ray diffraction: a practical approach. Springer Science and Business Media.

Szabó, A., Perri, C., Csató, A., Giordano, G., Vuono, D. and Nagy, J. B. (2010). Synthesis methods of carbon nanotubes and related materials. *Materials* 3(5): 3092-3140.

Tam, N., Ke, L., Wang, X. and Wong, Y. (2001). Contamination of polycyclic aromatic hydrocarbons in surface sediments of mangrove swamps. *Environmental Pollution* 114(2): 255-263.

Tang, C., Zhang, Q., Wang, K., Fu, Q. and Zhang, C. (2009). Water transport behavior of chitosan porous membranes containing multi-walled carbon nanotubes (MWNTs). *Journal of Membrane Science* 337(1): 240-247.

Tarigh, G. D. and Shemirani, F. (2013). Magnetic multi-wall carbon nanotube nanocomposite as an adsorbent for preconcentration and determination of lead (II) and manganese (II) in various matrices. *Talanta* 115: 744-750.

Tavakoli, A., Sohrabi, M. and Kargari, A. (2007). A review of methods for synthesis of nanostructured metals with emphasis on iron compounds. *Chemical Papers* 61(3): 151-170.

Tavakoly, S., Hashim, R., Salleh, A., Rezayi, M., Mehdinia, A. and Safari, O. (2014). Polycyclic aromatic hydrocarbons in coastal sediment of Klang Strait, Malaysia: distribution pattern, risk assessment and sources. *PloS one* 9: e94907.

Tian, Y., Yu, B., Li, X. and Li, K. (2011). Facile solvothermal synthesis of monodisperse Fe 3 O 4 nanocrystals with precise size control of one nanometre as potential MRI contrast agents. *Journal of Materials Chemistry* 21(8): 2476-2481.

Tofighy, M. A. and Mohammadi, T. (2011). Adsorption of divalent heavy metal ions from water using carbon nanotube sheets. *Journal of Hazardous Materials* 185(1): 140-147.

Trojanowicz, M. (2006). Analytical applications of carbon nanotubes: A review. *TrAC Trends in Analytical Chemistry* 25(5): 480-489.

Trombulak, S. C. and Frissell, C. A. (2000). Review of ecological effects of roads on terrestrial and aquatic communities. *Conservation Biology* 14(1): 18-30.

Tüzen, M. (2003). Determination of heavy metals in soil, mushroom and plant samples by atomic absorption spectrometry. *Microchemical Journal* 74(3): 289-297.

Umut, E. (2013). Surface Modification of Nanoparticles Used in Biomedical Applications. *Modern Surface Engineering Treatments 20*: 185-208.

Ünal, H. and Niazi, J. H. (2013). Carbon nanotube decorated magnetic microspheres as an affinity matrix for biomolecules. *Journal of Materials Chemistry B* 1(14): 1894-1902.

Vadivelan, V. and Kumar, K. V. (2005). Equilibrium, kinetics, mechanism, and process design for the sorption of methylene blue onto rice husk. *Journal of Colloid and Interface Science* 286(1): 90-100.

Valeur, B. and Santos, M. N. (2012). Molecular fluorescence: principles and applications. John Wiley and Sons.

Veličković, Z. S., Marinković, A. D., Bajić, Z. J., Marković, J. M., Perić-Grujić, A. A., Uskokovic, P. S. and Ristic, M. D. (2013). Oxidized and ethylenediamine-functionalized multi-walled carbon nanotubes for the separation of low concentration arsenate from water. *Separation Science and Technology* 48(13): 2047-2058.

Velu, S., Watanabe, S., Ma, X. and Song, C. (2003). Regenerable adsorbents for the adsorptive desulfurization of transportation fuels for fuel cell applications. *Chemical Society, Fuel Chemical Division* 48: 526-528.

Verstraete, W., Van de Caveye, P. and Diamantis, V. (2009). Maximum use of resources present in domestic "used water". *Bioresource Technology* 100(23): 5537-5545.

Vidal, J., Rivas, J. and Lopez-Quintela, M. (2006). Synthesis of monodisperse maghemite nanoparticles by the microemulsion method. *Colloids and Surfaces A: Physicochemical and Engineering Aspects* 288(1): 44-51.

Vijayakumar, R., Koltypin, Y., Felner, I. and Gedanken, A. (2000). Sonochemical synthesis and characterization of pure nanometer-sized Fe 3 O 4 particles. *Materials Science and Engineering: A* 286(1): 101-105.

Wakeman, R. and Williams, C. (2002). Additional techniques to improve microfiltration. *Separation and Purification Technology* 26(1): 3-18.

Wang, J. and Chen, C. (2009). Biosorbents for heavy metals removal and their future. *Biotechnology Advances* 27(2): 195-226.

Wang, J., Chen, Z. and Chen, B. (2014). Adsorption of polycyclic aromatic hydrocarbons by graphene and graphene oxide nanosheets. *Environmental Science and Technology* 48(9): 4817-4825.

Wang, Y., Angelatos, A. S. and Caruso, F. (2007). Template Synthesis of Nanostructured Materials via Layer-by-Layer Assembly†. *Chemistry of Materials* 20(3): 848-858.

Wang, Y., Liang, S., Chen, B., Guo, F., Yu, S. and Tang, Y. (2013). Synergistic removal of Pb (II), Cd (II) and humic acid by Fe_3O_4.mesoporous silica-graphene oxide composites. *PloS one* 8(6): e65634.

Wei, D., Liu, Y., Wang, Y., Zhang, H., Huang, L. and Yu, G. (2009). Synthesis of N-doped graphene by chemical vapor deposition and its electrical properties. *Nano Letters* 9(5): 1752-1758.

Wei, X., Wang, Z., Wang, J. and Wang, S. (2012). A novel method of surface modification to polysulfone ultrafiltration membrane by preadsorption of citric acid or sodium bisulfite. *Membrane Water Treatment* 3: 35-49.

Wilson, E. B., Decius, J. C. and Cross, P. C. (2012). Molecular vibrations: the theory of infrared and Raman vibrational spectra. Courier Corporation.

Witek-Krowiak, A., Szafran, R. G. and Modelski, S. (2011). Biosorption of heavy metals from aqueous solutions onto peanut shell as a low-cost biosorbent. *Desalination* 265(1): 126-134.

Wu, N., Fu, L., Su, M., Aslam, M., Wong, K. C. and Dravid, V. P. (2004). Interaction of fatty acid monolayers with cobalt nanoparticles. *Nano Letters* 4(2): 383-386.

Wu, W., He, Q. and Jiang, C. (2008). Magnetic iron oxide nanoparticles: synthesis and surface functionalization strategies. *Nanoscale Research Letters* 3(11): 397.

Wu, W., He, Q. and Jiang, C. (2009). Magnetic iron oxide nanoparticles: synthesis and surface functionalization strategies. *ChemInform* 40(24): i.

Xu, L.-C., Vadillo-Rodriguez, V. and Logan, B. E. (2005). Residence time, loading force, pH, and ionic strength affect adhesion forces between colloids and biopolymer-coated surfaces. *Langmuir* 21(16): 7491-7500.

Xu, Y., Karmakar, A., Wang, D., Mahmood, M. W., Watanabe, F., Zhang, Y., Fejleh, A., Fejleh, P., Li, Z. and Kannarpady, G. (2010). Multifunctional Fe_3O_4 cored magnetic-quantum dot fluorescent nanocomposites for RF nanohyperthermia of cancer cells. *The Journal of Physical Chemistry C* 114(11): 5020-5026.

Yan, A., Liu, X., Qiu, G., Wu, H., Yi, R., Zhang, N. and Xu, J. (2008). Solvothermal synthesis and characterization of size-controlled Fe_3O_4 nanoparticles. *Journal of Alloys and Compounds* 458(1): 487-491.

Yang, J.-W., Lee, Y.-J., Park, J.-Y., Kim, S.-J. and Lee, J.-Y. (2005). Application of APG and Calfax 16L-35 on surfactant-enhanced electrokinetic removal of phenanthrene from kaolinite. *Engineering Geology* 77(3): 243-251.

Yang, K. and Xing, B. (2010). Adsorption of organic compounds by carbon nanomaterials in aqueous phase: Polanyi theory and its application. *Chemical Reviews* 110(10): 5989-6008.

Yang, S., Liu, H. and Zhang, Z. (2008). A facile route to hollow superparamagnetic magnetite/polystyrene nanocomposite microspheres via inverse miniemulsion polymerization. *Journal of Polymer Science Part A: Polymer Chemistry* 46(12): 3900-3910.

Zare, K., Gupta, V. K., Moradi, O., Makhlouf, A. S. H., Sillanpää, M., Nadagouda, M. N., Sadegh, H., Shahryari-ghoshekandi, R., Pal, A. and Wang, Z.-j. (2015). A comparative study on the basis of adsorption capacity between CNTs and activated carbon as adsorbents for removal of noxious synthetic dyes: a review. *Journal of Nanostructure in Chemistry* 5(2): 227-236.

Zhan, Y., Zhao, R., Lei, Y., Meng, F., Zhong, J. and Liu, X. (2011). A novel carbon nanotubes/Fe 3 O 4 inorganic hybrid material: synthesis, characterization and microwave electromagnetic properties. *Journal of Magnetism and Magnetic Materials* 323(7): 1006-1010.

Zhang, L. L. and Zhao, X. (2009). Carbon-based materials as supercapacitor electrodes. *Chemical Society Reviews* 38(9): 2520-2531.

Zhang, W., Wang, T. and Chen, X. (2010). Effect of surface/interface stress on the plastic deformation of nanoporous materials and nanocomposites. *International Journal of Plasticity* 26(7): 957-975.

Zhao, W., Gu, J., Zhang, L., Chen, H. and Shi, J. (2005). Fabrication of uniform magnetic nanocomposite spheres with a magnetic core/mesoporous silica shell structure. *Journal of the American Chemical Society* 127(25): 8916-8917.

Zheng, J.-C., Feng, H.-M., Lam, M. H.-W., Lam, P. K.-S., Ding, Y.-W. and Yu, H.-Q. (2009). Removal of Cu (II) in aqueous media by biosorption using water hyacinth roots as a biosorbent material. *Journal of Hazardous Materials* 171(1): 780-785.

Zheng, X.-J., Blais, J.-F., Mercier, G., Bergeron, M. and Drogui, P. (2007). PAH removal from spiked municipal wastewater sewage sludge using biological, chemical and electrochemical treatments. *Chemosphere* 68(6): 1143-1152.

Ziegler, C. and Eychmüller, A. (2011). Seeded growth synthesis of uniform gold nanoparticles with diameters of 15− 300 nm. *The Journal of Physical Chemistry C* 115(11): 4502-4506.

APPENDICES

Appendix 1. Calibration Curve For Lead(II) ions Standards

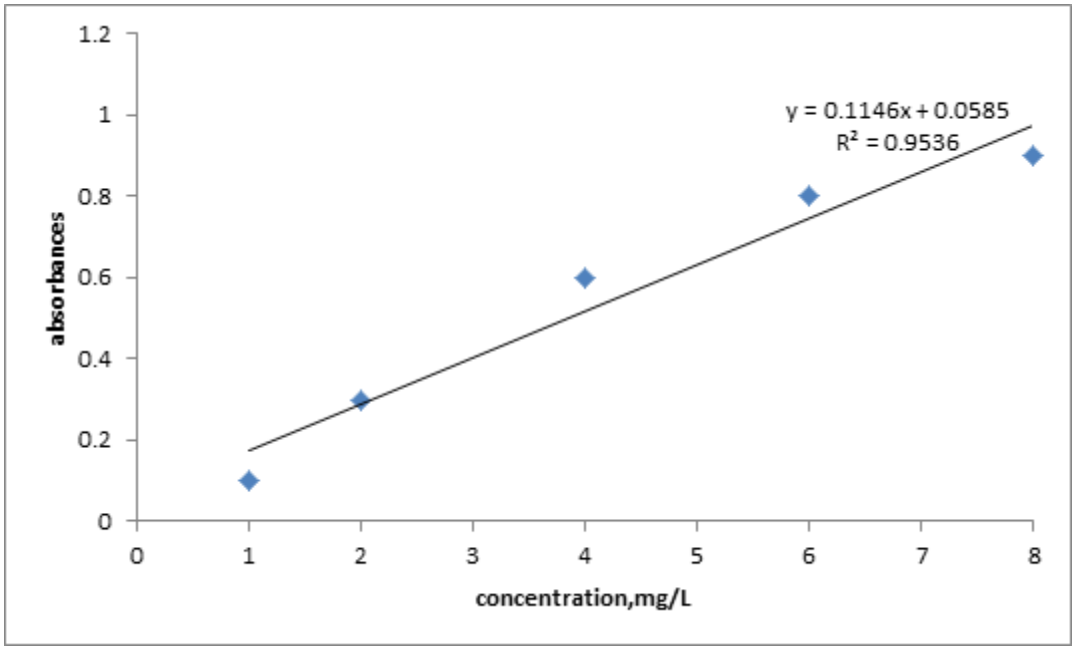

Appendix 2. Determination of pH_{PZC}

				pHi			
		2	4	6	8	10	12
pHf	1	2.5	4.7	5.1	3.8	7.5	11.7
	2	2.1	4.9	5.1	3.9	7.1	11.7
	3	1.7	4.6	5.1	4.1	7	11.9
	4	2.1	4.8	5.2	3.8	7.2	11.8
	5	2.2	4.8	5.5	3.9	6.7	11.6
	6	2.4	4.9	4.9	3.8	7.1	11.9
	7	2.6	4.8	4.8	3.9	7	11.8
	8	2.7	4.8	4.9	4.4	7.3	11.9
	9	2.3	4.6	4.8	4.5	7.2	11.8
	10	2.5	5.5	4.7	4.1	7.7	11.9

Appendix 3. Investigating adsorbent dose for Pb(II) ions removal

2 mg/L		0.02	0.04	0.06	0.08	0.1	0.12
Pool		adsorbed	adsorbed	adsorbed	adsorbed	adsorbed	adsorbed
	1	0.628223	1.405699	1.32768	1.436228	1.374491	1.386662
	2	0.736771	1.312076	1.467436	1.561058	1.561058	1.356662
	3	0.799186	1.312076	1.483039	1.561058	1.561058	1.508643
	4	0.783582	1.32768	1.498643	1.575455	1.576662	1.541058
	5	0.783582	1.343284	1.483039	1.561058	1.561058	1.545455
	6	0.783582	1.249661	1.483039	1.561058	1.545455	1.561058
	7	0.799186	1.32768	1.467436	1.561058	1.561058	1.561058
	8	0.783582	1.343284	1.52768	1.561058	1.561058	1.526662
	9	0.767978	1.32768	1.52768	1.483039	1.561058	1.501058
	10	0.783582	1.32768	1.32768	1.483039	1.561058	1.461058
4 mg/L	1	1.105432	1.921099	2.124168	2.52018	2.166491	2.144666
	2	1.006269	2.10076	1.909436	2.105834	2.123058	2.262144
	3	1.021659	1.924076	2.053793	2.004283	2.223091	1.932165
	4	1.426209	2.026188	1.725031	2.043523	2.343689	2.051106
	5	1.216358	2.243284	2.142304	2.221579	2.124101	1.922501
	6	1.116943	1.896608	2.253039	1.835019	2.109242	2.004283
	7	1.392649	2.102783	1.902504	1.93005	2.355104	1.739101
	8	1.160921	1.635533	2.135235	2.001024	1.891003	1.953254
	9	1.065583	1.571648	2.063613	2.063949	2.439104	1.855296
	10	1.344609	1.783068	2.129783	2.107888	1.926513	1.951058

Appendix 4. Investigating Contact time for Pb(II) ions removal

2mg/L		10	20	30	60	90	120	180	240
Pool		adsorbed	adsorbed	adsorbed	adsorbed	adsorbed	adsorbed	adsorbed	adsorbed
	1	0.907734	1.234057	1.312076	1.32768	1.276657	1.334267	1.314422	1.322413
	2	0.938942	1.203528	1.296472	1.343284	1.243284	1.302711	1.343284	1.331246
	3	1.001357	1.296472	1.280868	1.312076	1.374491	1.374491	1.342557	1.333244
	4	0.970149	1.280868	1.32768	1.358887	1.364699	1.313353	1.305699	1.319226
	5	0.892809	1.249661	1.249661	1.343284	1.32768	1.300225	1.332116	1.332116
	6	0.923338	1.234057	1.280868	1.374491	1.343284	1.305114	1.331442	1.321142
	7	0.970149	1.219132	1.32768	1.32768	1.312076	1.317724	1.310433	1.322314
	8	0.970149	1.296472	1.343284	1.343284	1.374491	1.374491	1.361448	1.338897
	9	0.938942	1.249661	1.32768	1.358887	1.358887	1.342664	1.331453	1.331135
	10	0.923338	1.265265	1.358887	1.312076	1.32768	1.335631	1.319946	1.34012
4mg/L		adsorbed	adsorbed	adsorbed	adsorbed	adsorbed	adsorbed	adsorbed	adsorbed
	1	1.239965	1.600349	1.800175	2.079581	1.879581	2.29075	2.211533	2.060035
	2	1.159686	1.239965	1.760035	2.203141	2.044266	2.040314	1.972312	1.900349
	3	1.280105	1.560209	1.800175	1.800175	1.990175	2.013352	2.003215	2.001745
	4	1.320244	1.52007	1.639616	2.179581	1.879581	2.182461	1.810214	2.003141
	5	1.360384	1.560209	1.52007	1.879581	1.879581	1.800175	2.001745	1.960035
	6	1.080279	1.52007	1.760035	1.840314	1.990314	1.840314	2.0011	1.719895
	7	1.1303	1.600349	1.719895	2.001745	2.017452	1.95986	1.950033	2.001745
	8	1.320244	1.52007	1.679756	2.079756	1.979756	1.840314	1.940361	2.000314
	9	1.280105	1.47993	1.719895	1.940314	1.840314	1.800175	1.805201	2.101745
	10	1.320244	1.52007	1.840314	2.09075	2.1521	1.99033	1.993019	1.890035

Appendix 5. Effect of pH on Pb(II) ions removal

2mg/L	pH 1	pH2	pH3	pH4	pH5	pH6	pH7
Pool	adsorbed	adsorbed	adsorbed	adsorbed	adsorbed	adsorbed	adsorbed
1	1.030393	1.249661	1.545455	1.622795	1.622795	1.300271	1.331096
2	1.136771	1.280868	1.32768	1.622795	1.638399	1.654003	1.654003
3	1.045319	1.374491	1.60787	1.467436	1.654003	1.569607	1.654003
4	1.045319	1.390095	1.592266	1.400271	1.638399	1.639607	1.662144
5	1.045319	1.405699	1.60787	1.638399	1.405699	1.638399	1.301127
6	1.030393	1.24607	1.40554	1.610944	1.61138	1.302714	1.422911
7	1.006771	1.201154	1.315663	1.644925	1.639009	1.49432	1.40021
8	1.01886	1.300265	1.602293	1.400355	1.600137	1.406961	1.33159
9	1.016024	1.311639	1.52116	1.50012	1.60845	1.449607	1.311383
10	1.002442	1.401164	1.601966	1.501191	1.401945	1.338399	1.30037
4mg/L							
Pool	adsorbed	adsorbed	adsorbed	adsorbed	adsorbed	adsorbed	adsorbed
1	1.030393	2.249661	2.545455	2.622795	2.822795	2.654003	2.611565
2	1.136771	2.280868	2.32768	2.622795	2.638399	2.654003	2.640901
3	1.045319	2.374491	2.60787	2.467436	2.954003	2.619496	2.654003
4	1.045319	2.390095	2.592266	2.654003	2.938399	2.669607	2.662144
5	1.045319	2.405699	2.60787	2.638399	2.705699	2.638399	2.62294
6	1.003119	2.119326	2.435449	2.610335	2.820545	2.654003	2.520961
7	1.011706	2.210097	2.300947	2.620069	2.83149	2.400971	2.50419
8	1.131845	2.372291	2.601669	2.43401	2.74002	2.445094	2.654003
9	1.031339	2.30195	2.509264	2.553916	2.812299	2.549065	2.762144
10	1.12292	2.406693	2.615592	2.629153	2.701929	2.429038	2.474003

Appendix 6. Effect of contact time and adsorption kinetics for Pb(II) ions

				Time				
	10	20	30	60	90	120	180	250
	prep	prep	prep	prep	prep	prep	prep	prep
	adsorbed	adsorbed	adsorbed	adsorbed	adsorbed	adsorbed	adsorbed	adsorbed
1	0.751696	0.871886	0.954775	1.05036	1.148531	1.275305	1.233522	1.499401
2	1.084111	0.831886	0.875727	1.010094	1.108942	1.127317	1.128446	1.159086
3	1.283555	0.958209	0.957689	1.119044	1.101164	1.144067	1.17365	1.155208
4	0.782632	0.831886	0.914925	0.994482	1.042191	1.105842	1.176931	1.159776
5	0.835577	0.839349	0.948787	1.103945	1.101574	1.146842	1.148862	1.259774
6	0.699517	0.855319	0.966937	1.078321	1.102107	1.149263	1.233757	1.159411
7	0.814111	0.853189	0.862266	1.104982	1.085012	1.167539	1.104219	1.028462
8	0.834355	0.993582	0.959378	1.012269	1.005705	1.130621	1.405763	1.377966
9	0.653826	0.856319	0.954338	1.004094	1.289599	1.121952	1.397437	1.18841
10	0.649756	0.865393	0.964896	1.001175	1.153297	1.127955	1.157331	1.198732
	std	std	std	std	std	std	std	std
	adsorbed	adsorbed	adsorbed	adsorbed	adsorbed	adsorbed	adsorbed	adsorbed
1	0.656446	0.644893	0.596884	0.847864	0.973102	0.985753	1.111769	1.201357
2	0.453666	0.587211	0.639953	0.948207	1.135852	1.04749	0.921107	1.130936
3	0.746448	0.689947	0.857042	0.972191	0.968234	1.04749	1.021167	1.074898
4	0.557761	0.603973	0.885663	0.958466	1.130534	1.14749	1.211644	1.123094
5	0.432169	0.79622	0.875634	0.964288	0.884522	1.025378	1.105219	1.040977
6	0.464775	0.955833	0.770565	0.844631	0.980642	1.198575	1.019674	1.206469
7	0.464288	0.893185	0.853854	0.921435	1.219783	1.04749	0.896487	1.205409
8	0.394276	0.622884	0.844734	0.973198	0.989957	1.04749	1.194672	1.114225
9	0.873544	0.598836	0.864733	0.974682	0.995477	1.04749	1.218795	1.104317
10	0.452746	0.576321	0.862442	0.975319	0.944732	1.032564	1.291785	1.024316

Appendix 7. Effect of initial Pb(II) ions concentrations and adsorption isotherms

	initial Pb(II) ions conc.					
	2	4	6	8	10	12
	prep	prep	prep	prep	prep	prep
	adsorbed	adsorbed	adsorbed	adsorbed	adsorbed	adsorbed
1	1.499905	2.919453	4.054545	5.016961	6.141113	4.958752
2	1.456716	3.284532	4.609227	5.606309	6.094301	5.981411
3	1.474355	2.983582	4.954545	6.04749	3.990502	6.141113
4	1.556716	2.998453	4.014925	5.406309	6.109905	4.964383
5	1.541113	2.283039	4.348711	5.704749	5.113297	3.883976
6	1.578697	2.893894	4.04749	5.643826	6.970149	5.094301
7	1.565875	2.992334	4.063094	4.597015	5.985753	5.094301
8	1.439905	2.954545	4.094301	4.028223	5.001357	4.964383
9	1.524301	2.297015	4.151099	3.612619	4.985753	4.956581
10	1.562822	2.901357	3.891255	4.628223	5.001357	4.964383
	std					
1	0.982605	2.947083	3.767978	2.860923	6.938942	3.812076
2	0.984166	2.156581	3.860923	4.954545	5.001357	3.796472
3	1.198358	2.265807	3.876526	3.985753	5.985753	3.780868
4	0.998453	2.095346	3.876526	4.954545	5.900136	3.82768
5	1.283039	2.5346	3.845319	3.938942	4.981682	3.843284
6	1.193894	2.04749	2.156716	3.783582	4.04749	3.82768
7	1.192334	2.063094	2.714111	4.346676	4.063094	3.812076
8	0.954545	2.001357	2.910991	4.11479	3.032564	3.796472
9	1.297015	1.916961	2.814111	4.830393	5.016961	3.82768
10	1.001357	1.932564	2.915672	3.083039	3.032564	3.843284

Appendix 8. Effect of cations on Pb(II) ions removal

			concentration of cations							
	0mg/L			1mg/L				4mg/L		
	Pb		Pb	Zn	Cu	Cd	Pb	Zn	Cu	Cd
pool	adsorbed		adsorbed	adsorbed	adsorbed	adsorbed	adsorbed	adsorbed	adsorbed	adsorbed
1	1.568563		1.481682	1.009195	1.178697	0.963772	0.588167	0.494301	0.31787	0.243284
2	1.532564		1.33787	1.074491	1.05943	0.943012	0.43095	0.380991	0.363772	0.32768
3	1.548168		1.432564	1.186974	1.248168	1.14787	0.69213	0.35943	0.325645	0.212076
4	1.463772		1.216961	1.296472	1.278697	0.948168	0.496744	0.409905	0.481682	0.180868
5	1.148168		1.193256	1.280868	1.168311	0.863772	0.688008	0.378697	0.348168	0.196472
6	1.425509		1.236558	1.326438	1.042217	0.967322	0.590978	0.418846	0.395328	0.412076
7	1.527421		1.413841	1.11528	1.382216	0.906278	0.591529	0.372444	0.411958	0.457307
8	1.45212		1.053894	1.063022	1.042118	0.938537	0.483364	0.494427	0.37462	0.38429
9	1.158442		0.997784	1.123374	1.116332	0.638527	0.514823	0.336842	0.322649	0.446311
10	1.472215		1.106417	1.235279	1.090453	0.696836	0.422665	0.377932	0.344639	0.526756

Appendix 9. Effect of cations on prepared and standard adsorbents Pb(II) ions removal

		cations removal						
	prep				std			
	pb2+	Zn2+	Cu2+	Cd2+	pb2+	Zn2+	Cu2+	Cd2+
1	1.463584	1.338291	1.311048	1.468396	1.481682	1.009195	1.178697	0.963772
2	1.432109	1.341579	1.407837	1.405837	1.33787	1.074491	1.05943	0.943012
3	1.346254	1.351048	1.405735	1.421906	1.432564	1.186974	1.248168	1.14787
4	1.432855	1.321958	1.453892	1.438905	1.216961	1.296472	1.278697	0.948168
5	1.443295	1.336722	1.347211	1.421058	1.193256	1.280868	1.168311	0.863772
6	1.41836	1.334827	1.472918	1.463905	1.236558	1.326438	1.042217	0.967322
7	1.357937	1.367257	1.448038	1.412859	1.413841	1.11528	1.382216	0.906278
8	1.443826	1.353726	1.422817	1.439574	1.053894	1.063022	1.042118	0.938537
9	1.334528	1.362875	1.437719	1.420785	0.997784	1.123374	1.116332	0.638527
10	1.404726	1.342719	1.447903	1.478204	1.106417	1.235279	1.090453	0.696836

Appendix 10. Effect of anions/ligand on Pb(II) ions removal

			ions/Ligands present				
pool	No ions present	Nitrate ion	NH3	EDTA	Nitrate ion	NH3	EDTA
1	1.658392781	1.0537826	1.45183175	1.303828	1.2957948	0.907836	1.105699
2	1.767836718	1.1604726	1.427734057	1.203396	1.2047927	1.089473	1.058887
3	1.633748194	1.2147936	1.42629684	1.284699	1.3937281	1.058936	1.12768
4	1.556281048	1.1482085	1.460471621	1.295537	1.411839	1.110499	1.201786
5	1.472047185	1.0289262	1.428937219	1.435282	1.1046867	1.300489	1.150372
6	1.685729048	1.1339578	1.394038105	1.328509	1.2246826	1.221038	1.201759
7	1.464893057	1.1047837	1.279462756	1.436228	1.0142795	1.046825	1.057836
8	1.63729461	1.0570176	1.413956826	1.436228	1.1038027	1.057836	1.393793
9	1.673519404	1.1057927	1.474936825	1.405699	1.0058925	1.290472	1.285673
10	1.573902189	1.3372685	1.404773518	1.343284	1.436228	1.227185	1.011472

Appendix 11. Effect of anions/ligand on prepared and standard adsorbents Pb(II) ions removal

	1M NO3-		1M NH3		1 M EDTA	
	1mg/L NO3-		1 mg/L NH3		1 mg/L EDTA	
	prep	std	prep	std	prep	std
pool	adsorbed	adsorbed	adsorbed	adsorbed	adsorbed	adsorbed
1	1.430295894	1.420194735	1.430583946	1.367947	0.178069	0.187069
2	1.376901703	1.419473724	1.356940858	1.379685	0.197069	0.177069
3	1.445038028	1.346864829	1.456893479	1.402195	0.177269	0.187069
4	1.433850038	1.400274738	1.439047291	1.389474	0.178069	0.187069
5	1.380482791	1.41904385	1.356839479	1.356349	0.197069	0.177069
6	1.438037913	1.325638294	1.437293848	1.448995	0.177269	0.187069
7	1.495037194	1.392487939	1.445283749	1.39895	0.178069	0.187069
8	1.364991273	1.411947948	1.368203835	1.364684	0.197069	0.177069
9	1.404793728	1.320395933	1.448947939	1.429105	0.177269	0.187069
10	1.434283649	1.205834894	1.447283729	1.386829	0.178069	0.187069

Appendix 12. Calibration Curve For Phenanthrene Standards

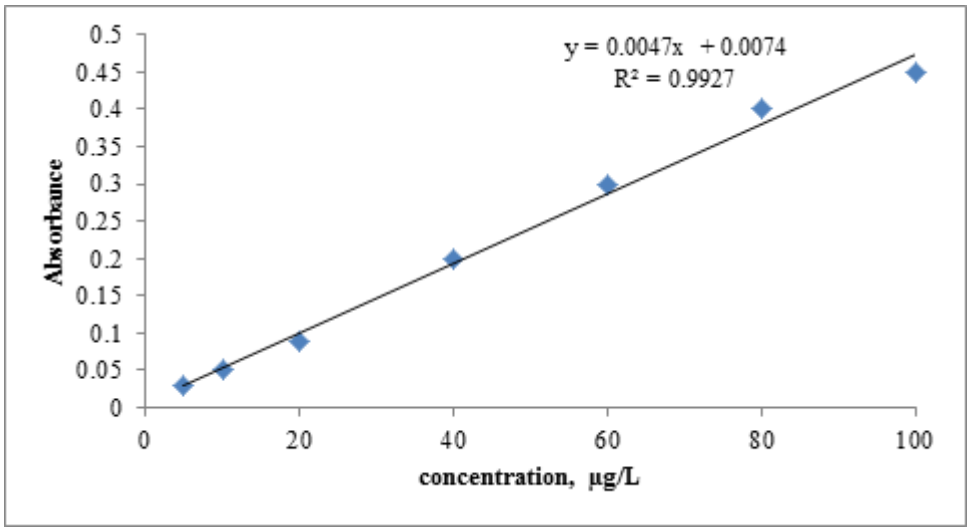

Appendix 13. Effect of adsorbent dose on phenanthrenes removal

	mass, mg					
20 µg/L	2	4	6	8	10	20
pool	adsorbed	adsorbed	adsorbed	adsorbed	adsorbed	adsorbed
1	5.595745	8.382979	9.212766	9.340426	9.340426	9.340426
2	5.93617	8.659574	8.87234	9.510638	9.510638	9.468085
3	5.468085	8.191489	9.276596	9.510638	9.510638	9.340426
4	5.382979	8.255319	9	9.340426	9.340426	9.808511
5	5.659574	8.319149	9.06383	9.404255	9.404255	9.276596
6	5.531915	8.723404	8.723404	9.680851	9.340426	9.617021
7	5.87234	8.531915	9.276596	9.276596	9.276596	9.404255
8	5.595745	8.106383	9.212766	9.617021	9.617021	9.468085
9	5.659574	8.106383	9.12766	9.617021	9.617021	9.340426
10	5.723404	8.319149	9	9.340426	9.340426	9.744681
15µg/L						
1	3.395745	6.829787	7.92766	8.330426	8.004255	8.042553
2	3.03617	6.395957	7.67234	7.106383	7.638298	7.680951
3	3.980851	6.902149	7.01766	7.06383	7.638298	7.553191
4	3.422979	6.443191	7.42579	7.319149	6.319149	7.808511
5	3.289574	6.309149	7.978723	7.045532	7.425532	7.446809
6	3.891915	6.709043	7.742553	7.085106	7.342553	7.316021
7	3.90234	6.421915	6.715957	7.259574	7.659574	7.319149
8	3.485745	6.768383	6.212766	7.670213	7.617213	7.208511
9	3.999574	6.916383	6.272596	7.602128	7.617021	7.340426
10	3.06234	6.669149	7.441208	7.340426	7.346626	6.846809

Appendix 14. Effect of contact time on phenanthrenes removal

	Optimization: investigatin contact time as fn of PHEN removal					
pool	5	10	20	30	40	60
20 µg/L	adsorbed	adsorbed	adsorbed	adsorbed	adsorbed	adsorbed
1	5.468085	5.87234	8.382979	8.659574	8.93617	9
2	6.255319	7.010054	8.191489	8.723404	10.87234	9.06383
3	6.659574	7.808511	8.319149	8.531915	9.012103	8.93617
4	5.595745	6.148936	8.595745	8.87234	9.06383	9.091662
5	6.87234	6.212766	8.255319	8.787234	8.93617	8.87234
6	5.531915	7.93617	8.191489	9.723404	10.32543	9.212766
7	6.595745	7.87234	7.978723	8.659574	8.87234	8.93617
8	5.723404	6.06383	8.319149	8.595745	9.276596	8.87234
9	5.808511	5.808511	8.531915	9.723404	8.93617	9.952302
10	6.976809	7.87234	8.595745	9.723404	9.093617	10.93617
15µg/L						
1	5.680851	6.834043	7.829726	8.574468	8.91307	8.88231
2	5.553191	6.735111	7.148226	8.724255	9.07234	8.63999
3	5.957447	6.106383	7.191422	8.191434	9.140225	8.934552
4	5.680851	6.93617	7.744681	8.874255	9.638298	8.911436
5	5.340426	6.595745	7.531915	8.734043	8.937021	9.92234
6	5.914894	6.021277	7.148936	8.742553	9.104357	9.765957
7	5.808511	5.425532	6.97234	8.657447	8.874255	8.89617
8	5.340426	6.829787	7.191229	8.574496	9.764468	9.874255
9	5.851064	6.510655	7.914894	8.341126	8.930213	8.989947
10	5.638298	6.872426	7.574468	8.715355	8.617133	8.693121

Appendix 15. Effect of pH on phenanthrenes removal

20 µg/L		pH			
Pool	1	4	7	8	12
	adsorbed	adsorbed	adsorbed	adsorbed	adsorbed
1	7.319149	8.531915	8.723404	8.87234	8.787234
2	8.191489	7.319149	8.446809	8.595745	8.446809
3	8.595745	8.595745	8.595745	8.93617	8.659574
4	7.659574	8.659574	8.87234	8.787234	8.595745
5	8.382979	7.106383	8.595745	8.723404	8.87234
6	8.446809	8.255319	8.531915	9	8.042553
7	8.255319	8.319149	8.319149	8.723404	9
8	7.106383	8.382979	8.191489	8.595745	8.87234
9	8.255319	8.446809	8.93617	8.446809	8.787234
10	8.319149	8.106383	7.638298	8.723404	8.93617
15 µg/L					
1	5.191146	6.531915	7.723404	7.287204	7.27834
2	6.110894	7.319149	8.044681	7.759574	7.048085
3	6.250957	6.595745	7.390596	8.993062	8.265574
4	7.3626	6.659574	8.187404	7.577874	7.595745
5	6.106938	6.106383	7.859574	7.291723	8.90874
6	6.689009	6.255319	7.531915	7.932267	7.250453
7	6.532919	7.919149	7.319149	8.072003	7.952546
8	7.632787	6.382979	7.191489	7.605909	7.87234
9	7.531915	6.446809	7.93617	7.968085	8.04078
10	6.114894	6.106383	6.638298	8.37234	8.093617

Appendix 16. Effect of contact time and adsorption kinetics for phenanthrenes

	Prep	Time, mins				
	5	10	20	30	40	60
1	9.842776	11.86958	11.86376	13.46947	13.78579	13.83459
2	8.976824	10.70478	12.92359	13.47096	13.46747	14.47467
3	9.795786	9.646875	11.97986	11.48849	12.47896	15.46756
4	9.457958	9.672386	13.78587	13.56953	14.4677	13.47986
5	9.578958	9.746769	13.87903	12.5068	14.56943	15.91238
6	8.938958	12.7288	11.22473	12.56986	14.58991	13.94785
7	9.125675	11.02673	13.93277	14.68673	15.69567	14.43826
8	9.29058	11.18468	12.94879	14.48857	14.4679	13.57893
9	8.957746	11.78467	13.22886	14.47985	14.4857	14.49328
10	9.194786	11.4789	13.49092	14.46959	14.46975	15.84457
pool	Std					
1	9.489362	10.85106	10.37937	13.19149	13.34043	11.02128
2	7.425532	9.510638	12.15472	12.2766	12.93617	11.97872
3	8.93617	10.91489	11.68356	11.25532	13.92979	14.40426
4	9.340426	9.702128	12.04781	10.87234	12.19149	15.36236
5	8.497224	9.978723	12.62382	11.05896	14.34036	15.95745
6	9.389266	9.86339	11.34043	13.14572	13.37568	13.02128
7	7.457286	9.505025	11.19149	12.24685	12.89057	13.97872
8	8.999748	9.728529	12.40426	11.26257	12.89468	11.40426
9	8.389386	9.756743	12.04683	12.94681	13.14362	12.46847
10	9.946726	9.904737	10.42553	13.04783	12.90447	13.67247

Appendix 17. Effect of initial phenanthrenes concentrations and adsorption isotherms

			initial phen conc. prepared					initial phen conc. standard					
	1	2	4	6	8	10		1	2	4	6	8	10
	adsorbed	adsorbed	adsorbed	adsorbed	adsorbed	adsorbed		adsorbed	adsorbed	adsorbed	adsorbed	adsorbed	adsorbed
1	0.689362	1.434043	2.064681	2.987234	3.987234	3.914894	1	0.87234	1.380851	1.944681	2.37234	2.76383	3.93617
2	0.784617	1.085106	2.12766	3.295319	3.953191	4.058915	2	0.740426	1.361702	2.255319	2.187234	4.902979	2.87234
3	0.621702	1.174468	2.068085	4.389362	2.191489	2.287234	3	0.574468	0.923404	2.106383	3.93617	2.276596	3.446809
4	0.808511	0.930638	2.171489	1.545532	2.92766	2.522511	4	0.361702	1.375377	2.97234	3.25734	2.787234	3.06383
5	0.848936	1.240426	2.578723	3.919149	2.905532	2.401702	5	0.795745	1.02766	1.910638	2.778723	4.93617	3.978723
6	0.829787	1.468085	2.046809	3.487234	3.99617	3.118511	6	0.659574	0.908511	1.890426	2.587234	2.723404	3.93617
7	0.948936	1.56383	1.961277	4.689872	3.987234	4.189149	7	0.723404	0.92766	2.046809	3.659574	3.43617	4.93617
8	0.877202	1.424255	3.251064	3.250213	2.295319	4.087234	8	0.508511	0.93617	1.37234	2.193617	4.689596	3.936783
9	0.82234	1.374468	2.271489	2.955319	3.765957	2.02766	9	0.774255	1.26383	1.787234	3.702128	4.06383	2.906383
10	0.674894	1.476596	2.974894	3.391915	2.553191	4.089362	10	0.757447	1.191489	2.659574	2.446809	3.412766	3.057723

Appendix 18. Effect of counter PAHs

		counter PAHs		
	0 µg/L PAHs		20 µg/L	
	Phenanthrene	Phenanthrene	Naphthalene	Anthracene
1	8.581560284	7.716312057	6.560894895	3.404255319
2	6.879432624	6.29787234	5.242086527	3.914893617
3	7.234042553	6.65248227	6.085765897	4.269503546
4	5.957446809	7.574468085	4.246322639	4.836879433
5	8.29787234	6.971631206	6.7009324	4.489361702
6	6.09929078	6.284397163	5.815752266	4.340425532
7	8.841607565	6.453900709	5.471594186	4.938534279
8	8.011631252	7.304964539	6.496538632	3.489361702
9	9.422530913	6.177304765	5.582972599	4.340425532
10	8.78578562	6.120567376	5.524289562	4.938534279

Appendix 19. Effect of counter PAHs on prepared and standard adsorbents phenanthrene removal

	20µg/L	PAHs adsorption prepared				PAHs adsorption standard	
	phenanthrene	naphthalene	anthracene		phenanthrene	naphthalene	anthracene
1	6.369391927	5.971946826	5.284571168	1	5.762947837	6.560894895	3.404255319
2	5.458927837	6.104752958	6.085671858	2	4.374692069	5.242086527	3.914893617
3	5.569723379	6.246931444	5.115725817	3	4.288302685	6.085765897	4.269503546
4	4.356271984	5.193216749	6.954686917	4	6.163968247	4.246322639	4.836879433
5	5.369283947	6.174942349	5.952869127	5	5.899437859	6.7009324	4.489361702
6	7.551029338	7.241304853	5.632825968	6	5.362846847	5.815752266	4.340425532
7	6.473939336	4.168246582	6.071956569	7	5.384614683	5.471594186	4.938534279
8	7.562938935	5.271014172	5.143686219	8	5.23103474	6.496538632	3.489361702
9	7.301389786	7.112795652	5.85786729	9	7.126224697	5.582972599	4.340425532
10	5.372039792	6.156285618	5.930348677	10	7.85236958	5.524289562	4.938534279

Appendix 20. Pb(II) removal from wastewater

		CNT-IPSF/Fe3O4 NCs	Activated carbon
	Initial Pb(II) conc.	final Pb(II) conc.(Prep	Final Pb(II) conc. (Std)
pool	conc.	adsorbed mg/l	adsorbed mg/l
1	2.234735414	1.010176391	0.821438263
2	2.149253731	0.373134328	0.60963365
3	2.537991859	1.050203528	1.435006784
4	2.694029851	0.723202171	1.391994573
5	2.020352782	0.352781547	0.546404342
6	2.29165536	1.152578019	1.099389417
7	2.289687924	0.990569878	0.889959294
8	2.976933514	1.373812754	1.445861601
9	3.018317503	0.84531886	1.694843962
10	3.070556309	0.020352782	1.655630936

Appendix 21. Phenanthrene removal from wastewater

		µg/g	
pool	Initial PHEN conc.	Final Phen conc. (Std)	final PHEN conc. (Prep)
1	32.9787234	17.44680851	7.517730496
2	31.56028369	20.42553191	10.63829787
3	32.12765957	17.5177305	14.32624113
4	33.4751773	14.25531915	10.85106383
5	32.34042553	14.60992908	10.9929078
6	32.12765957	14.32624113	11.13475177
7	31.63120567	10.70921986	14.11347518
8	32.26950355	10.9929078	14.25531915
9	31.56028369	13.75886525	13.61702128
10	31.91489362	14.32624113	10.78014184

Appendix 22. Investigating the reusability of the desorption test for Pb(II) ions

					mg/L							
		1		2		4		6		8		10
pool	ads.	Res.	ads.	Res.	ads.	Res.	ads.	Res.	ads.	Res.	ads.	Res.
1	0.74816825	0.251832	1.267483	0.732517	2.173175	1.826825	3.97545	2.02455	4.83175	3.16825	5.781832	4.218168
2	0.570149254	0.429851	1.399851	0.600149	2.029851	1.970149	3.906749	2.093251	5.850746	2.149254	6.288985	3.711015
3	0.693337856	0.306662	1.221438	0.778562	2.576662	1.423338	3.566666	2.433334	4.766621	3.233379	6.746227	3.253773
4	0.728941655	0.271058	1.171183	0.828817	2.561058	1.438942	3.269036	2.730964	5.583446	2.416554	6.044058	3.955942
5	0.781682497	0.218318	1.546032	0.453968	2.945183	1.054817	3.673383	2.326617	4.852783	3.147217	7.057183	2.942817
6	0.701492537	0.298507	1.207463	0.792537	2.529851	1.470149	3.299406	2.700594	5.246985	2.753015	5.766099	4.233901
7	0.733378562	0.266621	1.376662	0.623338	2.576662	1.423338	3.988577	2.011423	5.097897	2.902103	7.102662	2.897338
8	0.689416554	0.310583	1.157306	0.842694	2.995611	1.004389	3.667358	2.332642	4.849106	3.150894	6.614458	3.385542
9	0.637856174	0.576662	1.455621	0.544379	2.658447	1.341553	3.673766	2.326234	5.675845	2.324155	7.034662	2.965338
10	0.749253731	0.529851	1.116268	0.883732	2.759119	1.240881	3.447519	2.552481	4.591187	3.408813	5.675187	4.324813

Appendix 24. Removal efficiency of different desorption solvents for phenanthrenes

		methanol				n-hexane				acetone		
		prep		std		prep		std		prep		std
	residual	adsorbed	residual	adsorbed	residual	adsorbed	residual	adsorbed	residual	adsorbed	residual	adsorbed
1	15.61702	4.382979	16.64475	3.355248	11.39609	8.60391	11.33977	8.660229	10.54275	9.45725	11.56331	8.436691
2	15.59574	4.404255	15.11077	4.889228	11.64079	8.359212	11.68553	8.31447	10.64821	9.351789	11.89621	8.103791
3	15.59574	4.404255	15.99058	4.009425	11.42333	8.576669	11.46365	8.536346	10.40963	9.590371	10.99234	9.00766
4	15.59574	4.404255	15.8951	4.104898	11.70889	8.291107	11.54559	8.454409	10.42797	9.572032	11.78002	8.219978
5	15.6884	4.311598	15.67499	4.32501	11.62661	8.373392	11.64898	8.351022	10.56685	9.433147	10.7234	9.276596
6	15.00722	4.992779	16.61702	3.382979	11.2766	8.723404	11.45741	8.542591	10.67956	9.32044	11.56645	8.433552
7	15.6697	4.330295	15.67702	4.322979	11.40426	8.595745	11.2766	8.723404	10.7234	9.276596	11.06383	8.93617
8	15.44084	4.559155	15.61102	4.388979	11.12766	8.87234	11.40426	8.595745	10.44681	9.553191	10.78723	9.212766
9	15.55339	4.446611	15.61702	4.382979	11.2766	8.723404	11.34043	8.659574	10.78723	9.212766	11.09086	8.909144
10	15.66355	4.336449	15.61702	4.382979	11.21277	8.787234	11.34043	8.659574	10.53191	9.468085	10.7234	9.276596

Appendix 25. Adsorption-Desorption Studies for Phenanthrene

Pool	adsorp.-desorp. 1	adsop.-desorp. 2	adsorp.-desorpt. 3
1	25.53191489	30.92198582	36.45390071
2	22.62411348	31.91489362	32.05673759
3	25.31914894	33.97163121	31.13475177
4	21.77304965	34.39716312	32.69503546
5	21.4893617	31.34751773	34.96453901
6	22.19858156	30.92198582	36.45390071
7	25.95744681	31.91489362	32.05673759
8	28.65248227	33.97163121	31.13475177
9	28.43971631	34.39716312	32.69503546
10	28.15602837	31.34751773	34.96453901